1-1-2013

Celestial Paleontology: The Legacy of Dying Stars

Alexa Hodgson Hart
University of Denver

Celestial Paleontology: The Legacy of Dying Stars

A Dissertation

Presented to

the Faculty of Natural Sciences and Mathematics

University of Denver

in Partial Fulfillment

of the Requirements for the Degree

Doctor of Philosophy

by

Alexa H. Hart

August 2013

Advisor: Dr. Robert Stencel

Author: Alexa H. Hart
Title: Celestial Paleontology: The Legacy of Dying Stars
Advisor: Dr. Robert Stencel
Degree Date: August 2013

Abstract

In their death throes, stars dole out their atmospheric material to the interstellar medium in dramatic stellar winds and spectacular explosions. The details of this profound metamorphosis, from star to remnant, play a key role in the next generation of star formation as well as the energetic and chemical evolution of galaxies and the universe as a whole. Dying stars are thought to be the source of all of the nuclei heavier than iron in the universe, as well as more complex molecules, such as carbon chains, which form the backbone of life as we know it.

High mass Wolf-Rayet stars are likely progenitors of many types of Supernova, yet due to observational constraints we lack the most basic information about most of them: rather they are part of binary systems. This information is key to the determination of rather or not these stars will go supernova, since depending on its nature the companion can either draw mass off the Wolf-Rayet star, effectively quenching the march to explosion, or feed material onto the Wolf-Rayet star, speeding its demise as a supernova. Models of galactic evolution depend sensitively on the frequency of supernova for several reasons: they inject a great deal of energy into the Interstellar medium, they are the only known producers of nuclei heavier than nickel, and the shock waves that they create can stimulate star formation. In turn, the energy generated by supernova explosions drives the galactic wind, the heavier elements now present in the Interstellar Medium increase the efficiency of star formation, and the groups of new stars formed in the wake of a shock are thought to lead to the development of spiral arms in galaxies. In addition, because high mass stars are so short-lived, they can cycle through hundreds of generations in the time it takes one solar-type star's to evolve.

Though intermediate mass stars merely fizzle out in comparison, they are pivotal to the evolution of the universe because they make up over 97% of the stars that have had enough time to evolve off the Main Sequence since the Big Bang. These stars produce more than half of the carbon in the universe as well as much of the nitrogen, oxygen, and more complex molecules such as aromatic rings of carbon. This process, often referred to as chemical enrichment, strongly affects the star formation rates and the characteristics of the next generation of stars.

In this work, we explore the contributions of these two classes of stars to our own galaxy: we quantify the nature of the chemical enrichment to the Milky Way from a large sample of intermediate mass stars, and determine the binary status of a sample of Wolf-Rayet stars in the Milky Way.

Acknowledgements

This research was funded by a Pre-Doctoral fellowship from the Smithsonian Astrophysical Observatory, as well as the Donald Menzel Memorial Fund and the Rocky Mountain NASA Spacegrant Consortium at the University of Denver.

This work is based, in part, on observations made with the Spitzer Space Telescope, which is operated by the Jet Propulsion Laboratory, California Institute of Technology under a contract with NASA. In addition, the SMART software was used extensively for spectral extractions and analysis, and we would like to thank the SMART support team at Cornell University, particularly Vianney Lebouteiller, for his quick and thorough responses. The research presented in Chapter 4 was made possible by the tireless efforts of the PTI Collaboration

(http://pti.jpl.nasa.gov/ptimembers.html), and we would like to thank them for their invaluable support. In particular, we would like to thank Rachel Akeson for her assistance with the KI Archival data reduction. The research has also made extensive use of the NExScI visibility modeling tools and of the Keck Archive for retrieval of the KI data. This publication makes use of data products from the Two Micron All Sky Survey, which is a joint project of the University of Massachusetts and the Infrared Processing and Analysis Center/California Institute of Technology, funded by the National Aeronautics and Space Administration and the National Science Foundation. This research is also based on observations with AKARI, a JAXA project with the participation of ESA. In addition, this research has made use of the SIMBAD database, operated at CDS, Strasbourg, France, and NASA's Astrophysics Data System Bibliographic Services.

Contents

List of Tables

List of Figures

Chapter 1

Introduction

The brief yet enigmatic transition a dying star makes from glowing ball of gas to diffuse nebulae of stardust has long puzzled astronomers. During this phase, the circumstellar material can transforms the symmetry of its distribution, its chemistry and its ionization state. These changes reflect the complex interplay between dust formation on the micro scale and nebular shaping on the macro scale. Armed with our knowledge of the basic physics involved, researchers have developed models that allow us to leverage laboratory data to better understand this interplay. This thesis work marries observational data to these models to investigate the physical and chemical processes that shape and transform the nebula during this epoch. Specifically, we use observational data on two types of dying stars to identify the shaping agents present in the transition from star to nebula and characterize the dust formation processes which take place in these circumstellar environments, which are among the universe's most important incubators of celestial dust and complex molecules, including the organic molecules that are the basis for life as we know it. In the first project, discussed in Chapters Two and Three, I present my investigation (carried out with several collaborators) of intermediate mass stars during their transition to Planetary Nebula, with a particular focus on the chemical evolution of the dust and a phenomenon called "dual dust chemistry" with its apparent connection to the morphology of the newly formed nebula.

These two chapters will be submitted for publication this month (June 2013). For the second project, described in Chapter Four, my co-authors and I investigated the binary status of a sample of extremely massive dying stars called Wolf-Rayet stars, work which has implications for our understanding of the role that binarity plays in the formation and evolution of these stars. This chapter has been submitted for publication and is currently in revisions.

Before I discuss the manner of their ultimate demise, I'll give an abbreviated summary of the lives of these stars. The path a star follows in its lifetime is determined primarily by its initial mass, which astronomers call the Zero Age Main Sequence (ZAMS) Mass. High-mass stars ($M_{ZAMS} > 8M_{\odot}$) live a rock 'n' roll lifestyle, burning brightly but dying young and dramatically as supernovae. In contrast, intermediate-mass stars ($0.8M_{\odot} > M_{ZAMS} > 8M_{\odot}$) burn slowly, plodding along their evolutionary tracks for billions of years before dispersing their outer layers into space and fading from view as cooling embers, better known as white dwarfs. After I've summarized the evolutionary paths of each class of star, I'll give a synopsis of the most relevant literature on the phases studied here, where the stars are releasing their material back into space on their march towards oblivion. Finally, I'll describe the work presented here and it's implications for our understanding of expiring stars.

1.1 Intermediate-Mass Stars: Future Planetary Nebulae

Intermediate-mass stars are those with an initial (zero age main sequence, or ZAMS) mass of $0.8M_{\odot} - 8M_{\odot}$ (approximately; this range depends on metallicity, among other things). These stars spend most of their lives (roughly 10^9 years or more than 85% of their lifetimes; Blöcker 1995) converting hydrogen to helium on the main sequence. Once the core hydrogen is spent, and thus the outward pressure due to fusion ceases, gravity causes the core to contract to the point that the material around the (at this point inert) helium core is dense and hot enough to start to fuse hydrogen in a shell around the core, initiating

the giant phase. Due to the contraction of the core, more hydrogen is made available for fusion and the extra outward pressure caused by this extra energy generation causes the outer layers to puff up (but cool because they are now farther from the energy source). The core continues to contract until reaches the critical temperature (10^8 K) required for helium begin to fuse into carbon in the core via the triple-alpha process (in a secondary reaction, oxygen is created from the fusion of carbon and helium via the alpha process), while hydrogen burning continues in a surrounding shell in a phase we call the horizontal giant branch.

When the core helium is exhausted, the core contracts once again, resulting in a degenerate C/O core surrounded by helium- and hydrogen-burning shells. This increases the energy output from the central fusion zone, which causes the outer layers to again expand. This phase is called the AGB; the star burns hydrogen and helium in shells surrounding the spent C/O core. The helium burning is thermally unstable, and thus periodic runaway fusion reactions produce thermal pulses called helium flashes (this phase is called the Thermal Pulse AGB), where the helium ignites but quickly burns all the available fuel. During the AGB phase, there is a slow, dense and sometimes erratic stream of material leaving the star called the AGB wind. This wind has epochs of density enhancement due to the thermal pulsations described above, which could account for the appearance of shells in the structure of the circumstellar material.

As the mass loss process continues, the thick cloud of dust and gas it creates can obscure the star itself in visible wavelengths (García-Lario 2006). Eventually, the central star will have lost most of its mass (model predictions range from 70-85% of the initial mass for a $M_{ZAMS} = 4M_{\odot}$ star; Stanghellini & Renzini 2000). This depletion of the stellar envelope will eventually lead the slow, dense AGB wind to cease. The mass loss rate thus drops by an order of magnitude and the material expelled by the AGB wind drifts away and becomes a detached shell of material (van der Veen et al. 1989); this marks the beginning of the post-AGB phase (Kwok 1993).

Though we can conjecture about what happens next, observations are often difficult due to the significant reddening and/or obscuration of the central star. This obscuration is problematic because it introduces observational bias. Stars that have massive, optically thick dust clouds can be more difficult to find in optical/NIR surveys since there may only be emission from reflected starlight, while most can be easily found in mid-IR surveys due to thermal emission from the dust.

Post-AGB stars observed in the infrared with IRAS apparently fit into an evolutionary sequence with the effective temperatures (T_{EFF}) steadily increasing until the star is hot enough to ionize its envelope (spectral types marching from K, G, F, A to B; ionization begins at roughly $T_{EFF} > 25,000$ K; Balick & Frank 2002). Near the end of this progression, when the central star is a spectral type A or B, the star enters the transition from post-AGB to young planetary nebula. This transition lasts mere thousands of years. Once the star gets hot enough to ionize its envelope, the planetary nebula (PN) phase commences. The ionized material is optically thin, so for the obscured cases, the central star re-emerges in visible wavelengths once the ionization front has traveled sufficiently far out into the envelope. Morphologies of these young PNe are diverse: bipolar, elliptical, point-symmetric and spherical (Balick & Frank 2002).

1.1.1 Why So Square?

One of the unsolved mysteries of planetary nebulae is how they are shaped. They exhibit a dazzling array of symmetries and sizes; so much so that it seems unlikely one process could account for them all. Magnetic fields, rotation, binary interactions, and inherently asymmetric winds have all been proposed as shaping mechanisms (Owocki et al. 1996; Blackman et al. 2001; De Marco 2009; Meixner et al. 1997, respectively).

For the most part, giant stars appear to be spherically symmetric. Though few AGB stars have been spatially resolved, they were traditionally assumed to have spherically symmetric mass loss as well. We now know, however, that many AGB stars have non-spherical

outflows. A seminal Hubble survey that imaged the stars thought to be in the phase immediately following the AGB found a high incidence of at least axisymmetry (Ueta et al. 2000). Most planetary nebulae also show departures from spherical symmetry (Balick & Frank 2002). The time of onset of and the triggering mechanisms for these asymmetries are still not understood.

1.1.2 Dust Chemistry

During the AGB phase, stars shed most of their outer envelope in a dense circumstellar wind. This wind contains products of nucleosynthesis from earlier phases, particularly helium, carbon and oxygen. These winds are typically characterized as having a carbon- or oxygen-rich chemistry. Helium flashes that happen during the AGB phase can cause the convection zone to reach all the way down to the helium-burning shell, carrying up material enhanced with ^{12}C. If this process is efficient enough (but the competing mechanism called Hot Bottom Burning is not; Karakas 2010), the carbon will tie up all of the oxygen in CO, leaving only C to form other molecules. This creates a carbon-rich environment. Otherwise, oxygen dominates the chemistry in the circumstellar environment. Whether a star has an oxygen- or carbon-rich environment is tied closely to its initial mass; only the subset of stars with a mass of (roughly) $1.5 - 4M_{\odot}$ typically become carbon-rich (Karakas & Lattanzio 2007).

The value of this C/O ratio dramatically affects the asteromineralogical and perhaps even morphological characteristics of the circumstellar envelope in the AGB phase and beyond. During the post-AGB phase, carbon-rich dust species are much more optically thick, thus affecting everything from the efficiency with which radiation pressure drives the winds to how much of the envelope is shielded from stellar radiation. This shielding could allow for the formation of more complex molecules or larger dust grains. A small minority of AGB stars called dual chemistry objects show evidence of both carbon and oxygen species in their dust, a phenomenon which has yet to be understood (Szczerba et

al. 2007). The incidence of this so-called dual chemistry is much higher in post-AGB stars, however, and in these cases the phenomenon could be indicative of either an O-rich environment preserved in outflows (Zijlstra et al. 1991), or in a stable, dusty structure (potentially a circum-stellar disk around the post-AGB star or a binary companion, or a circum-binary disk) while the mass loss from the central star transformed to C-rich (Zijlstra et al. 1991; Waters et al. 1998; Molster et al. 1999). Alternatively, the photo-dissociation of CO by a hot central star could create a non-equilibrium state where limited amount of C is available in an O-rich envelope (Guzman-Ramirez et al. 2011; Guzmán-Ramírez et al. 2012).

1.1.3 Post-AGB Stars: Previous Work

A number of photometric and spectroscopic studies have been undertaken to identify potential post-AGB sources. Photometric identifications for proto planetary nebulae (PPNe), such as those developed on the basis of IRAS colors (van der Veen & Habing 1988) greatly expanded the number of candidate post-AGB objects. Newer studies have applied photometric selection criteria to stars in our own galaxy (Ramos-Larios et al. 2009) and the LMC and SMC (van Aarle et al. 2011). Spectral surveys, such as the one carried out by Suárez et al. (2006) have further refined our understanding of the optical properties of post-AGB stars as a class. Spectral surveys of O-rich PPNs with ISO revealed crystalline silicates (Molster et al. 2002b) while surveys of C-rich spectra revealed features at 21 and 30μm and unidentified infrared emission features at 3.3, 6.2, 7.7 and 11.3 μm now commonly associated with PAHs (Hrivnak et al. 2000). The Toruń catalogue of Galactic post-AGB and related objects currently contains 326 likely post-AGBs (Szczerba et al. 2007).

Imaging surveys of PPNe undertaken with the ground-based IR cameras (MIRAC2 & Berkcam) and the Hubble Space Telescope revealed elongation in all of the detected and resolved reflection nebulae (Meixner et al. 1999; Ueta et al. 2000). Furthermore, those sur-

veys and subsequent work (Ueta et al. 2005; Siódmiak et al. 2008; Lagadec et al. 2011) confirmed the existence of two distinct classes of proto-planetary nebulae: SOLE-Toroidal (star-obvious low-level-elongated) nebulae, which do not totally obscure the central star, tend to have elliptical morphology and have low surface brightness nebulosity, and DUPLEX Core-Elliptical (dust-prominent longitudinally extended) nebulae, which have dense, optically thick dust waists that completely or partially obscure the central star and often exhibit dramatic bipolar morphologies. These classes are not merely distinguished by the viewing angle alone; they have been found to represent distinct morphological classes with differing optical thicknesses in the circumstellar shell. This difference may correlate with progenitor mass, with DUPLEX nebulae forming from high-mass progenitor AGBs while SOLE nebulae form from intermediate-mass progenitors. Meixner et al. (2002) suggested that the enhanced mass loss that forms the dusty waists in the DUPLEX nebulae is enabled by a binary companion.

Several mechanisms have been proposed to explain the shaping of planetary nebulae, most of which fall into three broad categories: magnetic fields, rotation, and binary interactions. The diversity of shapes and sizes in planetary nebula seems to indicate that more than one shaping mechanism is responsible, and indeed, many current theories on the formation of individual nebulae involve a combination of shaping agents. In broad terms, the close-in magnetic fields and rotation can shape the nebula by creating inherently asymmetric winds, thus creating equatorially enhanced outflows that lead to the formation of dusty waists or collimated polar outflows. Large-scale magnetic fields can shape the envelope at later stages (Sabin et al. 2007). However, models that generate jets, collimated outflows and circum-stellar (or circum-binary) disks can also be constructed on the basis of binary interactions (De Marco 2009). There is presently no consensus on this issue; for more on each of these models and the question of nebular shaping, see the excellent review by Balick & Frank (2002).

1.1.4 This work

In this work I present the results of one of the largest, most comprehensive space-based surveys of post-AGB stars to date. The survey was carried out on the world's most sensitive near- and mid- infrared space telescope with a sample that is ten times larger than the typical post-AGB study. This unique data set has allowed my co-authors and I to shine new light on a subject that has in the past been plagued by small number statistics.

To address the question of shaping, it is imperative that researchers determine the first incidence (in an evolutionary sense) of asymmetry in these objects. In this work, my co-authors and I assess the symmetry of the circumstellar material in a sample of late stage post-AGB stars, both through direct imaging and a detailed analysis of the characteristics of the circumstellar dust species. In particular, we model the Spectral Energy Distribution of the dust to look for the signature of a circumstellar waist structure. Additionally, in the later planetary nebula phase, the occurrence of so-called "dual chemistry" in the circumstellar dust appears to be phenomenologically related to the presence of a dense, circumstellar waist (Guzman-Ramirez et al. 2011). In this work, we test that hypothesis for the late-stage post-AGB phase. In addition, several observational signatures have been proposed as indicators of evolutionary status in post-AGB stars. We have collected these proposed signatures and searched for correlations among them to test their veracity as evolutionary clocks. This analysis is the first of its type, as previous studies have typically included fewer than ten sources.

For this work, I've grouped together observations proposed for by my collaborators in separate programs to form a sample of targets that span the entire temporal sequence from star to nebula (Fazio et al. 2006, 2007, 2008; currently available in the IPAC Spitzer archive[1]). The three observational programs were targeted at slightly different epochs of the transition from star to nebula: post-AGB stars (26 stars; Program ID 50116), young PNe

[1] http://irsa.ipac.caltech.edu/data/SPITZER/docs/spitzerdataarchives/

(36 targets called “transition objects” in the proposal; Program ID 30036), and planetary nebulae (18 sources; Program ID 40115). Each of these is discussed in more detail below.

My co-authors and I designed the post-AGB sample to select stars that are nearing or have just passed the end of the post-AGB phase, that is, stars that are on the brink of or have just begun ionizing their envelopes. To find such stars, my collaborators started with targets that were characterized as post-AGB candidates based on their IRAS colors (Suárez et al. 2006) and then further constrained them to have a central star of spectral type A and a far-IR excess typical of PNe dust emission (Parthasarathy et al. 2000). The spectral type condition should limit the sample to objects with very hot central stars, which should be those that are at the very end of the post-AGB phase. Type A stars should not generally be hot enough to ionize surrounding material.

To isolate true young PNe (“transition objects”), i.e. stars that have just begun to ionize their circumstellar envelopes, my collaborators chose a sample of post-AGB candidate (again selected based on IRAS colors and infrared excess) with slightly hotter spectral type B central stars were chosen. These stars should be very nearly hot enough to emit ionizing radiation. As an independent measure of ionization, my collaborators also observed these sources with the radio interferometer called the Very Large Array; 16 of the 36 were detected, confirming the presence of ionized gas (Umana et al. 2004; Cerrigone et al. 2008).

The planetary nebulae chosen by my co-authors all have H-deficient central stars of late, carbon-rich Wolf-Rayet spectral type ([WC 8–12]). These PNe may also have in common a peculiar spectroscopic property: simultaneous evidence for both oxygen-based crystalline silicates and carbon-based PAHs in their dust. A correlation between PNe with [WC] central stars has been well established (Cohen et al. 2002), but the physics responsible for this relationship is still debated (Perea-Calderón et al. 2009).

Observations

The intermediate-mass star sample I've compiled comprises 70 targets in total that were observed with Spitzer Space Telescope. All have infrared spectra covering 5–40 μm and images centered at 3.6, 4.5, 5.8 and 8 μm. Additionally, I was awarded six half-nights on the Magellan 6 m telescopes, some of the planet's largest ground-based telescopes, located at La Silla Observatory in Chile, to get follow-up data (near-infrared spectra and images).

The IRAC and PANIC imaging revealed extended emission around a few post-AGBs, the results of which I will discuss in Chapter Three. In addition, I extracted photometry for all of the sources. I used these photometric points, with the addition of archival photometry, to model the Spectral Energy Distributions (SEDs) of these sources.

As seen in the infrared, carbon-rich sources show emission in the aromatic infrared bands (AIBs) commonly attributed to polycyclic aromatic hydrocarbons (PAHs) at 3.3, 6.2, 7.7, 8.6 and 11.3 μm (Hrivnak et al. 2007), as well as an SiC feature at 11.3 μm (Speck et al. 2009) and in some cases a mysterious feature at 21 μm (Cerrigone et al. 2011). Oxygen-rich sources have silicate features at $\sim$10-18 μm and $\sim$24-33 μm and show evidence for water ice (Dijkstra et al. 2006).

Interestingly, Cerrigone et al. (2009) found that approximately 40% of the transition object sample were dual-chemistry objects (showing evidence for both silicates and PAHs), a striking contrast to the global occurrence of $\sim$ 10% among PNe. The authors noted that this might be due to a selection effect, in particular the choice of objects with a far-IR excess which may be indicative of the presence of a disk. Additionally, 70% of those dual-chemistry objects were radio-detected in free-free emission, hinting at a potential correlation between photo-dissociation and the dual-chemistry phenomenon. Modeling of the PAH features resulted in the conclusion that the PAH molecules are located in the outflows, far from the central star. While the transition objects appear to have a 40% incidence of dual-chemistry objects, the nominally younger post-AGB sample had only 20% of the

objects displaying dual-chemistry characteristics. This reinforces the idea that dual dust chemistry may be associated with photo-dissociation rather than spatially segregated dust structures. This will be discussed in greater detail in Chapter Two.

The IRS spectra for 67 of the proposed sources has revealed the following breakdown in the sample (three objects that had failed observations): 14 O-rich post-AGBs, 10 C-rich post-AGBs, 20 Mixed Chemistry post-AGBs, 10 Young PNe, 5 mature PNe, and 8 sources that were misidentified (LBVs, YSOs). In all of the post-AGB sources, more than one dust emitting component is necessary to fit the SED, with dust temperatures ranging from 100-1000 K.

I will present the resulting spectra and spectral analysis in Chapter Two, and the imaging and analysis of the Spectral Energy Distribution are presented in Chapter Three.

1.2 High-Mass Stars: Future Supernovae

Stars that are born with more than $8M_{\odot}$ of initial mass evolve quickly along the main sequence, where they convert most of their core hydrogen to helium on the order of 10^6 years via the CNO cycle (hydrogen fusing to helium using carbon, nitrogen, and oxygen as catalysts). Once the core hydrogen is exhausted, the star leaves the main sequence, the outer layers expand and the star becomes a giant and then supergiant. During these phases, nuclear fusion via the alpha process (helium fusing with carbon to make oxygen, then helium fusing with oxygen to make Ne, and so on to produce all the alpha elements) happens first in the core, and once the fuel is exhausted there, the burning migrates outward into shell burning, resulting in concentric shells of nuclear fusion. In these massive stars, this nuclear fusion ladder can create nuclei as heavy as ^{56}Fe (plus ^{56}Ni that decays to ^{56}Co then ^{56}Fe) in the core. The supergiant phase lasts even less time; for the most massive stars, only 10^5 years. Once the core material has been converted to Ni and Fe, it becomes inert and there is no further exothermic fusion reaction that can produce the energy necessary

to stave off gravitational collapse. When the pull of gravity overwhelms the core, it will collapse to become a white dwarf supported by electron degeneracy. When (and if) the degenerate core grows to reach the Chandrasekhar limit of $1.4M_{\odot}$, the star will implode and meet its demise as a supernova.

The particular high-mass stars studied in this work are called Wolf-Rayet stars, which are thought to have evolved from the most massive supergiants ($M_{ZAMS} > 8M_{\odot}$) (Crowther 2007). These stars exhibit high mass loss (10^{-5} to $10^{-4}M_{\odot}$ per year), and are thought to be the stellar progenitors of Type Ibc and some Type II supernova. The winds coming off these stars are so dense that the stellar surface continuum is almost completely obscured. As a result, their spectra are dominated by broad emission lines ($\pm$3000 km/s) and very few (if any) lines of absorption. The spectra are also unique in their lack of hydrogen lines. Wolf-Rayet spectra are instead dominated by helium, with highly ionized carbon, nitrogen and oxygen lines. These are all thought to be core material, and are not normally observed on the surface of stars (Crowther 2007). The role that mass loss plays in the evolution of these stars is poorly known, as are the exact mechanisms of the loss. Many Wolf-Rayet stars are components in systems of interacting binaries. The unusually large amounts of hot gas streaming off these stars makes the detection of actual mass exchange dynamics possible, and also provides an opportunity to watch binary interactions and the resulting feedback happen on a shorter time scale.

The anomalous lack of hydrogen in the spectra of Wolf-Rayet stars has led some to hypothesize that they were originally more massive stars (Of stars, red supergiants or luminous blue variables), but their binary companions have stripped them of their outer layers via Roche-lobe overflow (RLOF). This would result in the core of the star being exposed, and could explain the presence of core material on the surface (Crowther 2007). The percentage of WR stars that form via RLOF is unknown, but theory predicts as many as 19% of WRs in the Milky Way (Bartzakos et al. 2001) have formed this way. Thus far, researchers have found evidence for binary companions in 40% of galactic WR stars (van der Hucht

2001), but the spectroscopic and photometric methods used to detect binary companions (and even planets) in other types of stars do not work well for Wolf-Rayet stars due to their peculiarities, so the theory that all WR stars are the result of binary interactions cannot be ruled out.

This work presents the first attempt to apply a promising new technique to test this binary formation scenario: near infrared interferometry. This technique is potentially the best tool that we have to answer this question because an interferometer samples the spatial frequencies of the on-sky brightness distribution, thus enabling us to easily distinguish the signal variation due to a binary companion from variations due to intrinsic variability of the star. This study is the first attempt to answer the WR binary question because the Palomar Testbed Interferometer (PTI) that we used was among the first such instruments that were sensitive enough to detect any Wolf-Rayet stars at all. Though this work is the first attempt to resolve previously undiscovered companions of WR stars, studies of this type have spatially resolved known spectroscopic WR binaries for the first time, enabling us to constrain orbital parameters and approximate distance measurements: using the IOTA3 Interferometer, researchers were able to resolve the binary system of WR 140 (Monnier et al. 2004). Using a mask on a single telescope, the technique that is a precursor to the use of modern multi-telescope near infrared interferometers, a group was able to model the pinwheel nebula surrounding (known binary) WR 104 (Monnier et al. 1999) with Keck I, while similar structure was mapped around (known binary) WR 98a (Tuthill et al. 1999), and Allen et al. (1981) were able measure the extent of the dust shells around two Wolf-Rayet stars. The increased sensitivity and order-of-magnitude improvement in angular resolution offered by interferometric telescope arrays such as PTI have finally made interferometry a viable technique for studying more than just the few brightest WR stars.

1.2.1 Wolf-Rayet Stars: Previous Work

As the chemically evolved progeny of massive O-type stars, WR stars are characterized by heavy mass loss. These stars are flinging their outer envelopes away into space at thousands of kilometers per second, resulting in a mass loss of $10^{-5} - 10^{-4} M_{\odot}$ per year, which can form nebulae around the central stars that are tens to hundreds of stellar radii in extent.

The spectra of these stars are similar to massive O-type stars, but anomalous for their lack of hydrogen absorption lines. Instead, we see emission lines from material that results from nuclear CNO burning. These bright, broad emission lines from the strong stellar winds dominate the spectra. Subtypes WN and WC are defined by the appearance of optical emission lines from He, C, N and O ions. In WN (nitrogen) spectra He I-II and N III-V lines dominate, and in WC (carbon) spectra C II-IV, He I-II and O III-IV lines dominate. For an excellent review of the properties of Wolf-Rayet stars, see van der Hucht (1992).

The energy distribution of WRs exhibits a prominent excess in the infrared due to the absorption and re-emission of most of the stellar radiation by the circumstellar envelope. This energy is primarily re-radiated in continuum free-free emission (Hackwell et al. 1974). Some dusty WR stars exhibit periodic or episodic variability in the infrared, indicative of dust formation events (Williams, 1987). Late WC stars also exhibit thermal dust emission lines (Allen et al. 1972). This infrared excess and the bright, compact central sources make these objects ideal for investigations of binary status with near-infrared interferometers.

1.2.2 This Work

The unusual characteristics of Wolf-Rayet stars has led some to speculate that all WR stars are in multiple systems (van der Hucht 2001). In this scenario, the companion is responsible for stripping away the outer layers of the star. Unambiguous detections of binary companions in these stars are rare because of the high levels of intrinsic variability in both the photometric data and the spectra. Detecting shifts in the emission line is complicated

by extreme broadening due to high velocities in the winds. In addition the dust seems to form sporadically and non-isotropically, so that infrared lines are also subject to a great deal of intrinsic variation. Fortunately, thanks to advances in observational instrumentation, near-infrared interferometers have gained the sensitivity necessary to observe some of these sources. This technique holds great promise because the signature of intrinsic stellar variability is easily distinguished from the signature produced by a binary companion. In this work, we present one of the earliest attempts to apply this newly developed instrumentation to a sample Wolf-Rayet stars with the aim of unambiguously determining the binarity of the brightest observable WRs. In doing so, we establish interferometry as a superior technique for future determinations of WR binarity.

Using the Palomar Testbed Interferometer, we attempted to observe every Wolf-Rayet star that was bright enough to possibly produce fringes in the best seeing conditions. These stars were WR 121, 134, 136, 137, 139 and 140. In addition, we supplemented our data with some archival data from the Keck Interferometer shared risk time. We pulled archival observations for WR 134, 135, 136, 137, 140 and 148. These were valuable to us as the Keck interferometer has a different orientation and baseline from PTI, and thus provided slightly better coverage of the Fourier transform space corresponding to the intensity distribution on the sky, called the UV plane. We were lucky enough to catch WR 121 in an unusual outburst that conveniently increased its brightness significantly; we propose this was a dust creation event of the type that has been proposed for other WR stars. Unfortunately, we were the only group monitoring the star at that time, so the data we have on the outburst are limited. Nonetheless, we were able to constrain the size of the circumstellar envelope and report that the star is likely single, despite its dramatic variability that in other sources has been tied to stellar wind interactions in a wind collision region (e.g. WR 140; Dougherty et al. 2005).

The seeing requirements for these sources was stringent and the data on these stars ended up being more sparse than we had hoped. Wolf-Rayet stars are known to be vari-

able in the near infrared and likely have complex dust distributions (such as the pinwheel nebulae mentioned above), and the scarce UV plane coverage limited our ability to distinguish between binarity and these complexities. Despite these limitations, we were able to constrain binarity for most of the sources and provide estimates of their angular extent, which demonstrates the power of our method and will provide critical proof of concept for observations proposed using the next generation of interferometers. In Chapter Four, we describe this work and the conclusions we were able to draw from the observations.

1.3 Conclusions

The results of two research projects are presented here. The first is one of the largest, most comprehensive space-based surveys of post-AGB stars to date. The survey was carried out on the world's most sensitive near- and mid- infrared space telescope with a sample that is ten times larger than the typical post-AGB study. As I discuss in Chapters Two and Three, we have found that the majority of late-stage post-AGBs in our sample appear to harbor a reservoir of dust near the star, likely in the form of a dusty waist or disk, where the dust grains coagulate and are processed by radiation from the central star. These objects also seem to have at least two distinct dust components which are either spatially segregated (such as in an outflow and a disk) or that are merely distinguished by their exposure to radiation from the central source (e.g., if a dusty waist shields radiation from part of the outflow). These results have important implications for our understanding of both the nebular shaping mechanisms taking place around these stars and the nature of the stardust that these stars provide in feedback to the interstellar medium.

The second project, described in Chapter Four, employed a novel technique to asses the binary status of a sample of extremely massive Wolf-Rayet stars. Though the study was plagued by the limited sampling typical of such pioneering studies, we were able to ascertain the presence (or lack thereof) of binary companions in most of our targets, and

critically determined that at least some WR stars are not currently binaries, a conclusion that has important implications for our understanding of how WR stars are formed.

Finally, I will sum up the conclusions of this research and outline how this data could be used in future work.

Chapter 2

A Spitzer Spectroscopic Survey of post-AGB stars

The final bursts of nuclear fusion in intermediate mass stars (0.8–$8M_{\odot}$) on the asymptotic giant branch (AGB) result in episodes of enhanced mass loss. As this material drifts outward and cools, a dense, rich circumstellar environment is created that is ripe for the growth of myriad molecular species (see Olofsson 2008) and the condensation of circumstellar dust grains (Murakawa et al. 2010). Among the diverse molecular and dust species observed in these environments are crystalline silicates (Molster et al. 2002a), polycyclic aromatic hydrocarbons (PAHs, e.g. Tielens 2008), Silicon Carbide (SiC; e.g. De Marco 2009), and C60 "bucky balls" (Cami et al. 2010; Kwok & Zhang 2011). These molecular factories and the nuclear fusion that fuels them are the driving engine behind the chemical enrichment of the interstellar medium, which feeds and shapes the next generation of stars and planets.

Post-AGB objects are those caught just after the AGB phase, in the rapid ($\approx 10^3$–10^4 year-long) transition from AGB star to planetary nebula (PN; e.g. Kwok 1993, van Winckel 2003). Commencing at the terminus of heavy AGB mass loss, the post-AGB phase is characterized by the presence of a cool, dense circumstellar cloud of gas and dust drifting

away from a quiescent central star that is slowly heating up as it contracts. If the central star becomes hot enough before the circumstellar material disperses, it will photodissociate and later photoionize some or all of this circumstellar material. Thus, objects on the post-AGB form a nominal evolutionary sequence from K to G, F, A and eventually OB. For the purpose of this paper, we define our terms in the following way: after the end of heavy AGB mass loss, the star is a post-AGB star. Once the central star reaches ionizing temperatures, we call the object a young planetary nebula (YPN).

Planetary Nebulae (PNe) display a dazzling variety of shapes and sizes, and the question of how these shapes and sizes are determined has been the subject of decades worth of investigation. The subject is still hotly debated, but the emerging understanding is that binary companions (even substellar companions) may play a significant role (Nordhaus et al. 2010; for an excellent review, see De Marco 2009). In particular, a companion may shape or focus mass loss, leading to the formation of a dusty Keplerian disk orbiting the star or a dusty "waist" (equatorial density enhancement) in the outflows. At the heart of this debate are the critical early stages of nebular shaping that take place on the post-AGB, when an actor as small as a planet can establish initial conditions that can lead to subsequent large-scale shaping.

As the central star evolves, the chemical characteristics of the circumstellar environment, namely the C/O ratio, can change. This change is thought to be the result of a third dredge up in the absence of efficient hot bottom burning that takes place in only a subset of the AGB mass range (approximately 1.5–$4M_{\odot}$, depending on metallicity; see Karakas et al. (2002) for further discussion). In these environments, CO will form first, leaving only the more abundant of C or O to form other molecules. Thus, the chemistry of the molecules that form around these stars in the later post-AGB phase can be classified in two broad categories: carbon-rich and oxygen-rich. This picture, however, is over simplified: in fact, many post-AGB sources show evidence for both carbon- and oxygen-containing molecules (Cerrigone et al. 2009). Many hypotheses have been proposed to explain this, including

the preservation of O-rich material in a disk while the remainder of the environment becomes C-rich, or the photodissociation of CO making some limited O available to form other molecules.

Table 2.1. Post-AGB Evolutionary Tracers

Wavelength	Source of emission	Traces	Proposed Evolution
7.7 μm	AIBs (C-rich)	Aromatic Hydrocarbons	Central λ shifts to shorter wavelengths
6.2 , 7.7, 8.5 & 11.2 μm	AIBs (C-rich)	Ionization, Grain growth & processing	Ionization fraction increases, characteristic grain size increases
30 μm	MgS (C-rich)	Dust Chemistry	Peak position & width change w/ temperature of underlying continuum
10-18 μm	Silicates (O-rich)	Dust Chemistry, Grain growth & processing	Changes from emission to absorption to emission
23.7, 27.6, & 33.6 μm	Crystalline Silicates (O-rich)	Grain processing (annealing)	Changes from emission to absorption to emission

In this chapter, we explore the chemical evolution of post-AGB stars as they evolve to PN. This sample represents the largest of its type, enabling us to use the evolutionary maturity of these objects as a baseline to explore how these stars and their circumstellar environment evolve during the PPN phase. Specifically, we use infrared spectroscopy to trace changes in infrared emission features such as PAHs and silicates through the evolution process. Table 2.1 lists some of these potential evolutionary indicators. Because we have detailed knowledge of the conditions (densities, abundances and timescales) necessary to foster the growth and destruction of these dust particles, placing their positions on an evolutionary track can help us to understand the mechanisms driving the evolution of the circumstellar envelope. This analysis will help us to determine rather the warm and hot dust observed around these stars is contained in a stable circumstellar structure or if it is simply forming in the outflows.

In section 2.1, we describe our data and reduction procedures. In section 2.2, we discuss our observational results; section 2.3 describes our data analysis procedure and results of spectral model fitting. In section 2.4, we discuss the big picture implications of this work.

2.1 Data

For this work, a sample of 70 targets spanning the range from post-AGB star to Planetary Nebulae were chosen from three completed GTO programs on Spitzer (Fazio et al. 2006, 2007, 2008. Each program combined observations using the Infrared Array Camera (IRAC; Fazio et al. 2004) and the Infrared Spectrometer (IRS; Houck et al. 2004) onboard the Spitzer Space Telescope (Werner et al. 2004). The observations were taken in three observing programs: 30036 (post-AGB stars), 40115 (mixed chemistry PNe) , and 50116 (transition objects). These three programs were chosen for inclusion so that the sample spans the evolutionary transition from post-AGB star to Planetary Nebula.

2.1.1 Sample Selection

The post-AGB stars in this sample were first identified as post-AGB candidates on the basis of the IRAS colors (Parthasarathy & Pottasch 1986), and later confirmed w/ the addition of optical spectroscopy (Parthasarathy et al. 2000; Suárez et al. 2006). In order to target the late-stage post-AGB stars, a subset of post-AGB candidates w/ hot (Spectral Type F, A or B) central stars was chosen from among the lists of candidates. The effective temperature range for the central stars, based on spectroscopic types, range from 5,100–29,000 K.

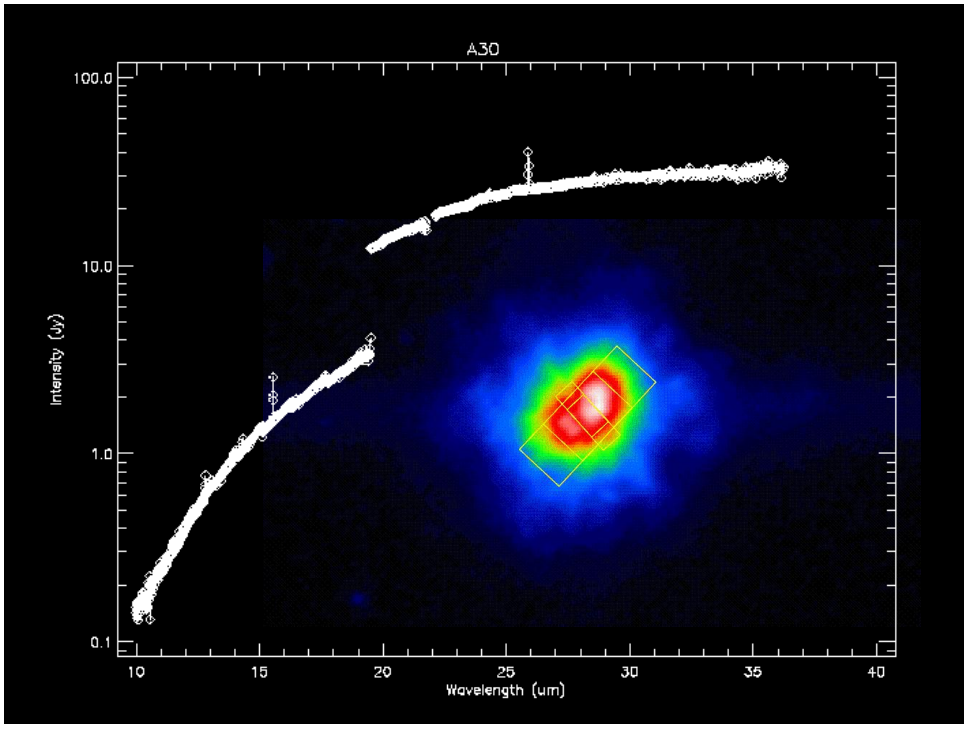

Figure 2.1 An IRAC image of young Planetary Nebula Abell 30, w/ the high resolution IRS slits overlaid to demonstrate the difference between the long (larger) and short (smaller) wavelength slit orientation and extent. The resulting spectrum is also overlaid as a typical example of the flux differences observed in these extended sources.

2.1.2 IRS Reduction

The brightest objects observed w/ IRS were taken in High Resolution Staring mode (10–37 μm; R $\approx$ 600) to avoid saturating the detector. The remainder were observed w/ Low Resolution Staring mode (5–38 μm; R $\approx$ 60–127). All Basic Calibrated Data (BCD) images were cleaned and masked w/ the campaign-specific rogue pixel masks using an IDL tool designed to remove image artifacts, including those due to cosmic rays and hot pixels, called IRSClean[1]. Once the images were cleaned, the method of reduction diverged for the two spectral modes : Low Resolution and High Resolution.

High Resolution Spectra

The High Resolution targets (most of the PNe, as well as some bright compact objects) were taken w/ dedicated backgrounds. Because we were targeting the emission around the central star, the backgrounds were taken w/in the boundaries of the extended nebula. Thus, we are subtracting out any contribution from the nebular foreground and our data will show only emission that originates in the core region.

w/in each nod position, the cleaned science and background images were combined (using the mean if there were only two images or the median if there were more). The background images were then subtracted from each science image w/ the same nod position. Spectra were extracted from these cleaned, background subtracted images using the SPICE software package (ver. 2.5.0) provided by the NASA/IPAC Infrared Science Archive for the extraction of IRS spectra. We extracted spectra from each nod position and compared the two for inter-nod discrepancies, the order edges were clipped and a nod mean was taken for each source. The resulting spectra are seen in Figures 2.2 through 2.5.

We encountered many problems in reducing the High Resolution mode data, including flux mismatches between the orders, each order having an overall arched shape, zig

[1] http://irsa.ipac.caltech.edu/data/SPITZER/docs/dataanalysistools/tools/irsclean/

zags imposed by the jagged order edges due to imperfect pointings, a spurious emission line at 19 microns, and very poorly constrained data at the longest wavelengths. Some of these problems are likely the result of our targets not being true point sources, perhaps especially at the longer wavelengths. This is consistent w/ the pattern we noticed in the data, that the targets that were most affected had a greater degree of nebulosity. To mitigate these effects, we extracted these spectra in every possible way using SPICE, as mentioned above, and also using the SMART IRS reduction software (version 1.6, Higdon et al. 2004; Lebouteiller et al. 2010). We found that for the High Resolution data, the SPICE Optimal Point Source extraction algorithm was the best. Optimal extraction involves first computing a wavelength-collapsed flux profile across the slits, and then the resulting profile is used to weight the extraction. This improved our jagged edge-order effects significantly and also improved the effects of some sources being slightly off center in the slits. Even so, there were some order mismatches; to address those, we first scaled the order containing the 25 μm wavelength range (convolved w/ the IRAS 25 μm bandpass) to agree w/ the IRAS photometric point at 25 μm (found in the IRAS Point Source Catalogue, v.2; Joint IRAS Science 1994), and then scaled the other orders to match. In most cases, this resulted in an overall flux adjustment of less than 15%. As an independent verification, we performed synthetic photometry on the scaled shorter wavelength orders and verified their agreement (w/in errors) w/ the published IRAS flux at 12 μm.

Low Resolution Spectra

The Low Resolution Spectrograph targets were taken w/out dedicated backgrounds, so in general the off-source nod position was used as a background. In some cases, one nod position caught emission from a nearby star; in these cases, an exposure taken while the star was aligned w/ a different order was used. We also sampled several extraction routines for these date, and found that the best result was derived from an Optimal Point Source extraction performed w/ SMART. Again this is probably because our sources were not perfect

point sources and/or were not perfectly centered, and as such the standard sum-across-the-slit routines created large mismatches between orders. The optimal routine minimizes these mismatches, and this is most easily done w/ the optimal two-nod extraction in SMART. Even w/ this optimized extraction, in some cases we found that there was still a flux mismatch between the Short-Low (SL) and Long-Low (LL); this is to be expected for objects w/ extended emission, since the aperture for LL is much larger than that of SL, and thus more light is collected from the surrounding nebula (in addition, the slits for the two wavelength segments differ in size and orientation, so that the long wavelength mode captured more of the nebulae; see Figure 2.1, which shows an IRAC image of one of the PNe w/ the spectral slits overlaid for demonstration). To account for these discrepancies, we multiplied the SL data by a scalar derived from the order mismatch and the scaled the entire spectrum (convolved w/ the IRAS 25 μm bandpass) to agree w/ the IRAS photometric point at 25 μm (found in the IRAS Point Source Catalogue, v.2; Joint IRAS Science 1994). This will not affect the relative strengths of lines in the spectra since this is only multiplication by a scalar, and should account for the difference in the size of the SL and LL slits.

2.1.3 Continuum subtraction method

In order to make the classifications discussed above, we had to distinguish the emission features from the thermal dust continuum. The broad, blended nature of the infrared emission features in these sources presents a challenge when attempting to define a region that contains only continuum emission. Thus, we chose to employ a fitting routine that fits the continuum, the gas-phase emission, and dust features simultaneously. We modified this routine, called PAHfit (the standard IDL routine MPFIT w/ the addition of AIB features built-in, downloadable from the author's website[2] and described by Smith & Draine 2012) to include several more features that are known to occur in post-AGB stars (silicates at 10 μm, SiC at 30 μm, and the unidentified 21 μm feature). This worked well for the feature-

[2]http://tir.astro.utoledo.edu/jdsmith/research/pahfit.php

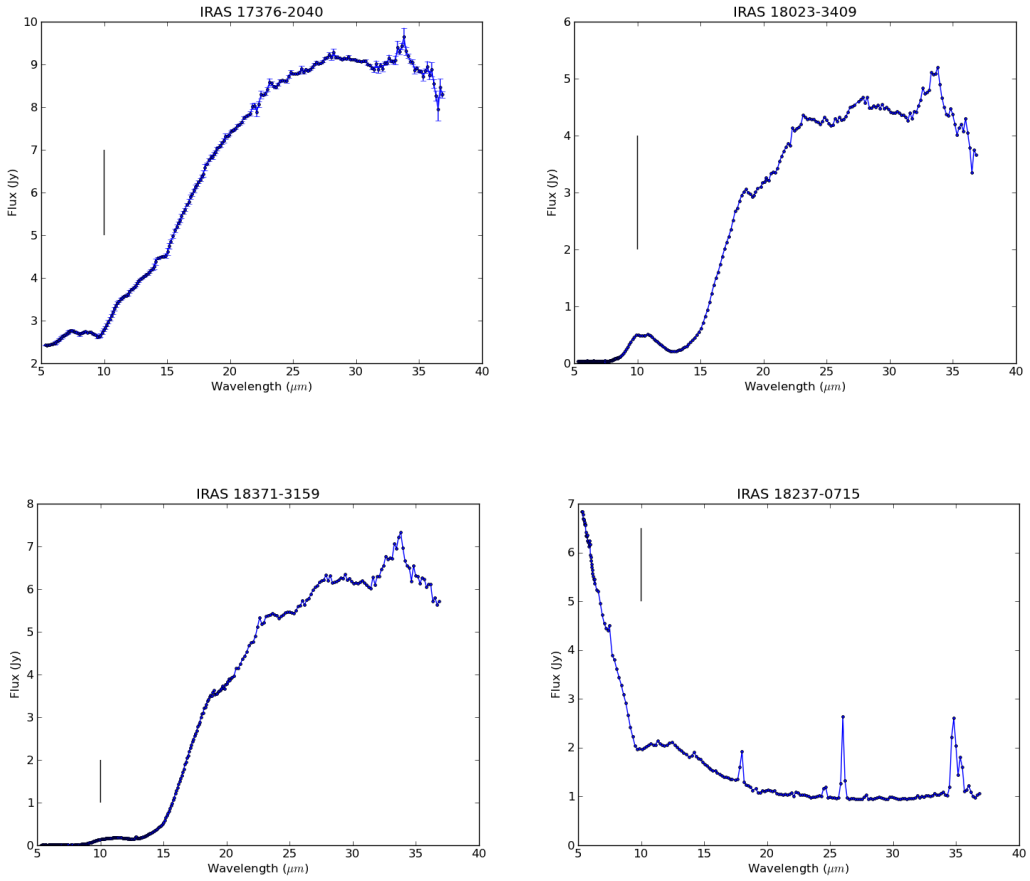

Figure 2.2 Post-AGB sources classified as oxygen-rich, based on the presence of a 10 μm silicate feature, marked w/ the vertical line. Typical error bars for this data set are shown on IRAS 17376-2040. Based on the IRAC image, IRAS 18237-0715 may be a Luminous Blue Variable or Young Stellar Object (see Ch. 2).

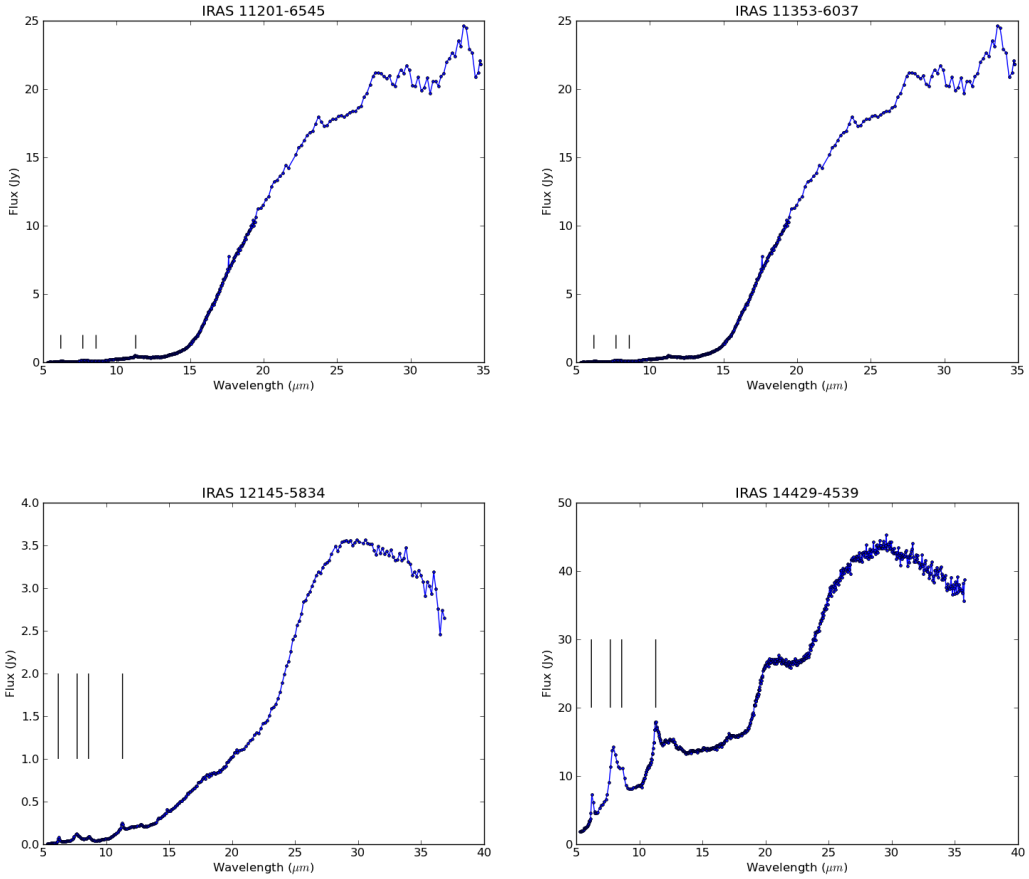

Figure 2.3 Post-AGB sources classified as carbon-rich, based on the presence of AIBs, marked w/ vertical lines.

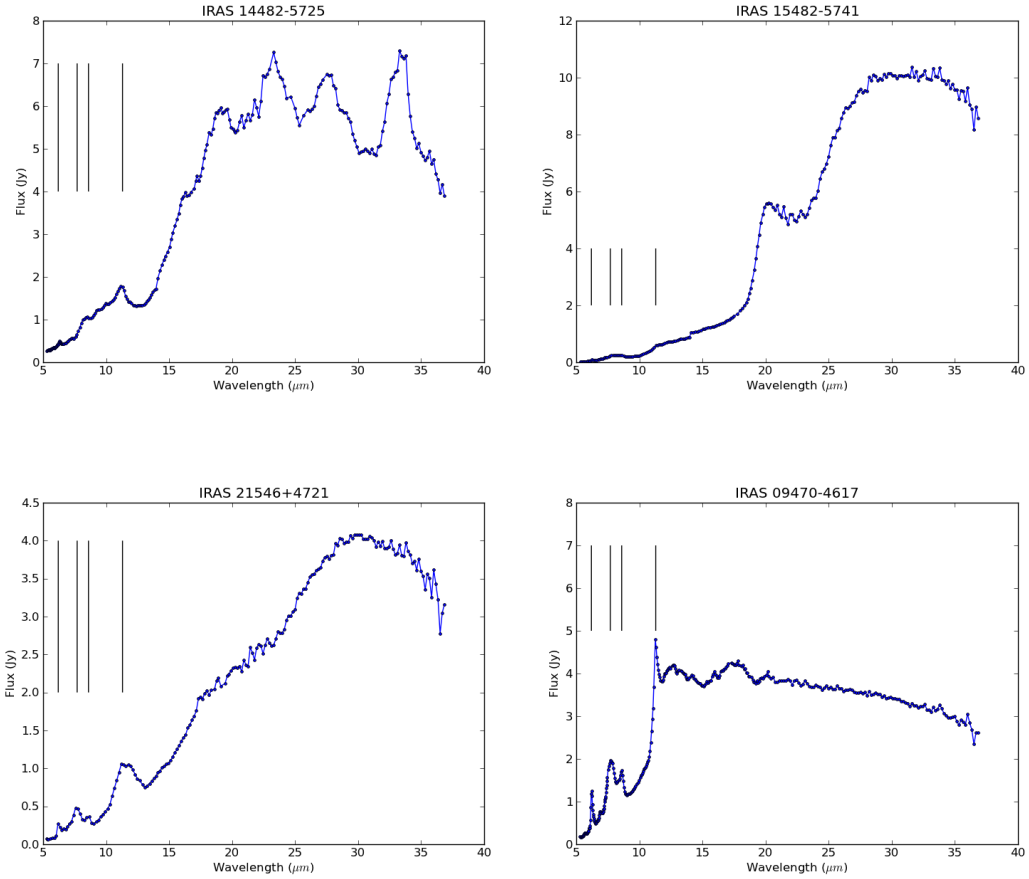

Figure 2.4 Post-AGB sources classified as carbon-rich, based on the presence of AIBs, marked w/ vertical lines.

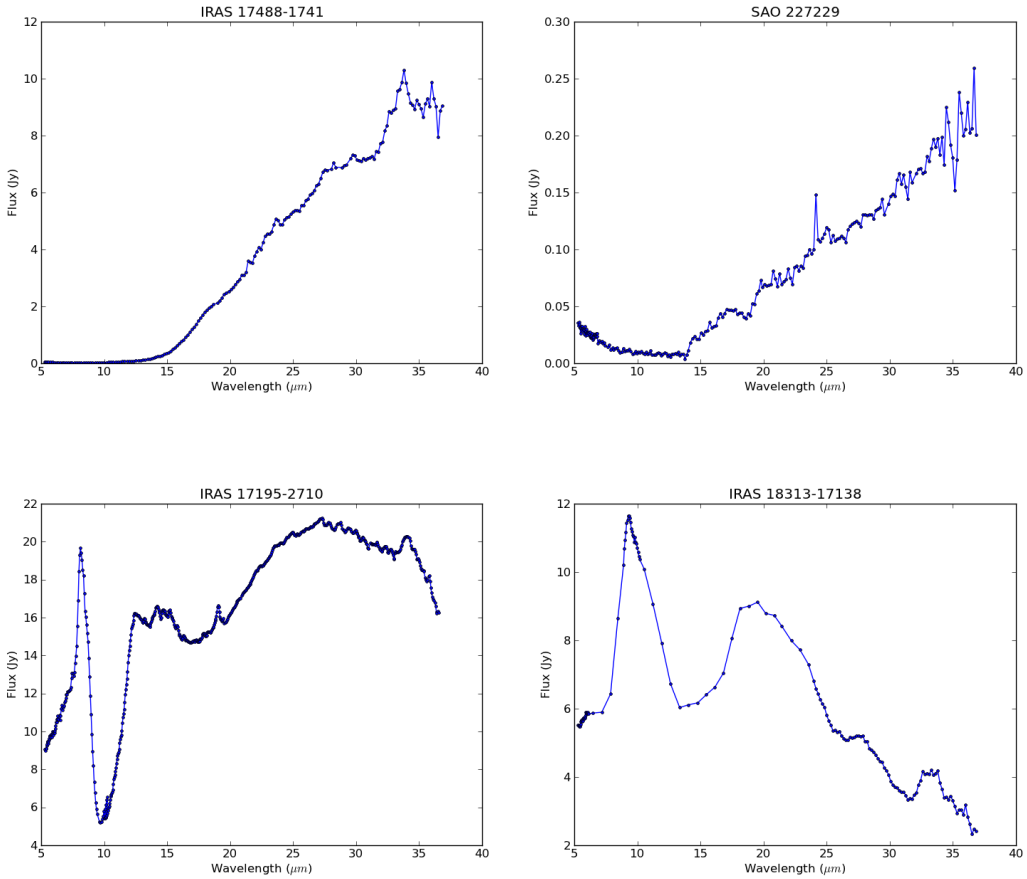

Figure 2.5 Atypical Post-AGB sources w/ less obvious classification. IRAS 17195-2710 is classified as oxygen-rich, while IRAS 18313-1730 is classified as mixed.

rich Carbon chemistry sources, but failed to find a good fit in the oxygen chemistry sources. Thus, to characterize the 10 μm feature, we subtracted a locally defined continuum and then fit the line w/ a gaussian.

2.1.4 Line and dust feature fitting method

To characterize the emission features in the spectra, we modified PAHfit (which is based on the IDL routine MPFIT, and has all of the AIB features built in) to include several specific dust features that are known to occur in post-AGB stars (silicates at 10 and 30 μm, and the unidentified 21 μm feature). This routine allows us to extract the characteristics of individual features and their relative strengths. Table 2.3 lists the feature strengths and Table 2.4 the scientifically relevant ratios for all of the carbon-rich sources.

2.2 Results

The final product of this processing can be seen in Figures 2.2 to 2.5. The 70 sources observed can be broken down into four categories: confirmed post-AGB stars (47), Young Planetary Nebulae (10), Mature Planetary Nebulae (5), and miscellaneous (8; mis-identified post-AGB stars and failed or incomplete observations). In order to call a source a post-AGB star, we required that it have thermal emission from dust, following the IRAS selected criteria of Szczerba et al. (2007). This criteria could in fact exclude some post-AGB stars that have optically thin dust or because the circumstellar material dissipated so rapidly that it will not be illuminated by the central star again (these are called "failed" Planetary Nebula, which are discussed in Moe & De Marco 2006). Additionally, because we selected sources w/ hot central stars, most of these fall w/in an SED class that can also include Young Stellar Objects (YSOs) that are still forming and Luminous Blue Variables (LBVs) that can harbor both hot and cool circumstellar dust. We have ruled out several sources as post-AGB based on their anomalous spectra, and also referred to our IRAC imaging at 8 μm to determine if

the star lies in what appears to be a star-forming or H_2 region. These sources, along w/ the rest of the sample, are listed in Table 2.2.

Table 2.2. Classifications based on IRS spectroscopy

Target	Program	Alt ID	Class	Silicate Type(s)[3]
NGC 40	Dual Dust PN	HD 826, IRAS 00102+7214	PN w/warm dust	···
NGC 1501	Dual Dust PN	CH Cam, IRAS 04026+6047	Mature PN	···
Minkowski 4-18	Dual Dust PN	IRAS 04215+6000	PN w/warm dust; AIB emission	···
PN PM 1-310	Dual Dust PN	IRAS 19367+2458	PN w/warm dust	···
Hen 2-459	Dual Dust PN	IRAS 20119+2924	PN w/warm dust; AIB emission	···
NGC 6905	Dual Dust PN	NT Del, IRAS 20201+1956	Mature PN	···
NGC 7026	Dual Dust PN	HD 201192, IRAS 21046+4739	Mature PN	···
Abell 30	Dual Dust PN	IRAS 08440+1803	PN w/warm dust	···
NGC 2867	Dual Dust PN	HD 81119, IRAS 09200-5805	Mature PN	···
PN PMR 1	Dual Dust PN	IRAS 09269-4923	Mature PN	···
PB 6	Dual Dust PN	ESO 213-7, IRAS 10113-5005	Mature PN	···
PB 8	Dual Dust PN	ESO 170-7,IRAS 11309-5649	PN w/warm dust	···
PN PMR 2	Dual Dust PN	IRAS 11322-5226	PN w/warm dust	···

Table 2.2 (cont'd)

Target	Program	Alt ID	Class	Silicate Type(s)[4]
Hen 2-99	Dual Dust PN	ESO 97-8,IRAS 13487-6608	PN w/warm dust	···
NGC 5315	Dual Dust PN	HD 120800, IRAS 13501-6616	···	···
NGC 6369	Dual Dust PN	V2310 Oph, IRAS 17262-2343	PN w/warm dust	···
Minkowski 2-20	Dual Dust PN	ESO 456-12, IRAS 17512-2935	···	···
Minkowski 2-31	Dual Dust PN	ESO 522-6, IRAS 18101-2530	PN w/warm dust	···
IRAS 17542-0603	Post-AGB	PN PM 2-32	Mixed	II
IRAS 01005+7910	Post-AGB	···	Carbon	···
IRAS 17074-1845	Post-AGB	BD-18 4436	Oxygen	I, III
IRAS 17203-1534	Post-AGB	···	Oxygen	I, III
IRAS 17364-1238	Post-AGB	PN PM 1-167	Oxygen	I
IRAS 17381-1616	Post-AGB	PN PM 2-28	Oxygen	I, III
IRAS 17423-1755	Post-AGB	Hen 3-1475	Carbon	···
IRAS 17460-3114	Post-AGB	HD 161853, SAO 209306	Oxygen	II

Table 2.2 (cont'd)

Target	Program	Alt ID	Class	Silicate Type(s)[5]
IRAS 18040-1457	Post-AGB	···	Not Post-AGB	I
IRAS 18062+2410	Post-AGB	HD 341617, V886 Her	Oxygen	I
IRAS 18070-2346	Post-AGB	···	Not Post-AGB	···
IRAS 18367-1233	Post-AGB	BD-12 5131	Not Post-AGB	II
IRAS 18371-3159	Post-AGB	PN PM 1-248	Mixed	I, III
IRAS 18379-1707	Post-AGB	PN PM 2-37	Mixed	I
IRAS 18435-0052	Post-AGB	···	Mixed	···
IRAS 18442-1144	Post-AGB	PN G022.0-04.3	Carbon	···
IRAS 19157-0247	Post-AGB	BD-02 4931	Mixed	II, III
IRAS 19200+3457	Post-AGB	PN PM 1-300	Mixed	II
IRAS 19306+1407	Post-AGB	···	Mixed	I
IRAS 19336-0400	Post-AGB	PN G034.5-11.7	Mixed	I, III
IRAS 19399+2312	Post-AGB	V450 Vul	Not Post-AGB	···

Table 2.2 (cont'd)

Target	Program	Alt ID	Class	Silicate Type(s)[6]
IRAS 19590-1249	Post-AGB	V5555 Sgr	Mixed	I, III
IRAS 20462+3416	Post-AGB	V1853 Cyg	Mixed	I
IRAS 20572+4919	Post-AGB	V1853 Cyg	Mixed	I
IRAS 21289+5815	Post-AGB	···	Mixed	II
IRAS 22023+5249	Post-AGB	PN G099.3-01.9	Mixed	I
IRAS 22495+5134	Post-AGB	HIP 112887	Mixed	I, III
IRAS 06556+1623	Post-AGB	OY Gem	Carbon	···
IRAS 09470-4617	Transition Object	···	Carbon	···
SAO 152360	Transition Object	FM CMa	Not Post-AGB	···
IRAS 10082-5647	Transition Object	GSC 08607-01509	Not Post-AGB	···
IRAS 11201-6545	Transition Object	PN PM 1-56	Oxygen	I
IRAS 11353-6037	Transition Object	PN PM 1-60	Mixed	III
IRAS 11387-6113	Transition Object	···	Mixed	I

Table 2.2 (cont'd)

Target	Program	Alt ID	Class	Silicate Type(s)[7]
IRAS 12145-5834	Transition Object	PN PM 1-64	Carbon	···
IRAS 12175-5338	Transition Object	V1024 Cen	Oxygen	I, III
IRAS 13245-5036	Transition Object	···	Carbon	···
IRAS 14325-6428	Transition Object	V1024 Cen	Carbon	···
IRAS 14429-4539	Transition Object	···	Carbon	···
IRAS 14482-5725	Transition Object	···	Carbon	···
IRAS 15482-5741	Transition Object	···	Mixed	···
SAO 243233	Transition Object	HD 143054; IRAS 15566-5043	Mixed	I
SAO 243756	Transition Object	IRAS 16206-5956	Oxygen	I, III
SAO 227229	Transition Object	HD 151212	Oxygen	III
IRAS 17119-5926	Transition Object	V839 Ara	Oxygen	···
IRAS 17195-2710	Transition Object	PN G358.7+05.1	Oxygen	II, III
IRAS 17317-2743	Transition Object	OH 359 +2.6	Oxygen	III

Table 2.2 (cont'd)

Target	Program	Alt ID	Class	Silicate Type(s)[8]
IRAS 17376-2040	Transition Object	···	Oxygen	III
IRAS 17488-1741	Transition Object	PN PM 1-184	Oxygen	III
IRAS 17576-2653	Transition Object	PN PM 1-198, OH 3.47 -1.85	Oxygen	I, III
IRAS 18023-3409	Transition Object	PN PM 1-208, CD-34 12448	Not Post-AGB	II, III
IRAS 18237-0715	Transition Object	V446 Sct	Not Post-AGB	···
IRAS 18313-1738	Transition Object	NSV 11033	Mixed	I, III
IRAS 21546+4721	Transition Object	PN G095.0-05.5	Mixed	···

We can further divide the confirmed post-AGB sources according to the chemical composition of the gas-phase molecules and solid state dust. We identified 14 sources that had a 10-micron silicate feature, which implies the presence of an oxygen-rich dust; we have labeled these at oxygen-rich post-AGB stars. Ten other confirmed post-AGB stars display Aromatic Infrared Bands (AIBs; due to gas-phase hydrocarbon rings often attributed to PAHs) which indicate that the circumstellar environment is carbon-rich; these we call carbon-rich post-AGB stars. An additional 20 sources were found to have emission in both the 10 micron silicate bump and in the AIBs; these we labeled as dual-chemistry post-AGB stars. Of the sources that did not meet our post-AGB criteria, ten were identified as Young Planetary Nebulae because they have both thermal dust emission as well as nebular (ionized) emission lines indicating that the central star has reached ionizing temperatures; the five most evolved (non-post-AGB) objects in our sample we have labeled Mature Planetary Nebula because they have nebular emission lines but no thermal dust emission. The remaining eight sources were thrown out because they are not true post-AGB stars, but instead Young Stellar Objects, Luminous Blue Variables, or perhaps dusty Giants.

A surprising result of these classifications is the unexpectedly high fraction of "dual-chemistry" post-AGB stars. This could be due to a selection bias, as we have chosen stars that are bright enough in the infrared to have shown up in surveys such as IRAS (the stars must show up in most or all of the IRAS bands to have been selected on the basis of IRAS colors as our sources were). The time window in which one might expect to observe the characteristic signature of both hot and cool dust in an individual post-AGB star is quite small, unless there is a mechanism (such as a dusty waist or disk) that is storing material close to the star for a more extended period of time, thus making the source bright in more of the mid- and far-infrared wavelengths. If such a structure does not exist, one would expect any dust formed around the star to cool and dissipate rapidly and thus not be bright at the shorter IR wavelengths for very long. By adopting a sample selected on the basis of IRAS colors, we might expect to have weighted our sample towards stars that

harbor stable dust reservoirs near the star in addition to having dust in outflows. Thus, the high incidence of these "dual-chemistry" objects in our sample favors the scenario in which the dual-chemistry phenomenon is related to the presence of a dusty waist or disk around the star. Further, if we divide the post-AGB stars according to the central star temperature into young post-AGB stars and mature post-AGB stars, we find that the incidence of "dual-chemistry" objects is 30% among the younger post-AGB stars (defined as having a $T_{EFF} < 10,000$ K), while among the mature post-AGB stars, that number is 54%. This may indicate that the molecules responsible for the AIB emission in these "dual-chemistry" stars forms at the onset of ionization rather than as a result of a truly carbon-rich circumstellar environment created by a Third Dredge Up in the AGB phase. This is consistent w/ the findings of Cerrigone et al. (2009), where my collaborators concluded that the molecules responsible for the AIBs (for convenience, we'll call them PAHs) are not located in the stellar atmospheres of a carbon-rich mass loss. In that study, the ionization fraction of the PAHs was very low, yet the central wavelengths of the features at 6.2, 7.7 and 11.2 μm are blue-shifted, indicating that the radiation from the central star is very hard. This scenario could indicate that the PAHs are located in the outflows, far from the central star, or might also be explained if the PAHs were shielded from the central star by a dust structure such as a dusty disk/waist. In this scenario, it seems most likely that PAHs are not the result of C-rich mass loss but rather photodissociation of CO in an O-rich environment.

There are many spectral features in these objects that can be used as chemical and evolutionary diagnostics. The most direct measure of the evolutionary status of these objects would the T_{EFF} of the central star, as it is contracting and heating up during this phase. Unfortunately, the post-AGB stars in this sample are dust enshrouded and we are unable to observe the starlight directly; the spectral types of these stars were determined from very faint reflected starlight, and are thus highly uncertain (corresponding to errors on the central star's T_{EFF} of as much as 10,000 K). We must therefore turn to other diagnostics to assess the maturity of individual sources. All types of post-AGB stars in my sample should

have emission due to H_2, and those lines will tell how it is being excited (UV or shock), which thus give us an indicator of hardness of the starlight's radiation (and thus a minimum T_{EFF} for the central star). The strength of forbidden lines such as [Ne II], [Fe II] and [S I] reveal the excitation mechanism (photodissociation or shock), and the ratios between them the ionization fraction (Fong et al. 2001), again measures of the minimum T_{EFF} of the central star. The ionization fraction measures the degree of maturity the object has reached, since the central star is not expected to be hot enough to emit ionizing UV photons until immediately before the PN phase. The same is true for the H_2 excitation; if it is only shock-induced, the object is most likely on the young end of the late post-AGB sequence, while if the culprit is photodissociation from UV photons, it must be nearing the PN phase. While our post-AGB data does not include any forbidden lines, we can look at the ionization fraction of molecular emission lines, a clue which we will use, along w/ hydrogen ionization information gleaned from near infrared imaging, to attempt to organize the sample in an evolutionary sequence (similar to what was done in Bachiller et al. 1997). Additional clues we will use in our attempt to place our sample in an evolutionary sequence are several dust chemistry-specific proxies for the evolutionary age of the source that have been proposed in the literature. These are detailed below.

For O-rich sources, the silicate feature at 10 μm is thought to shows in emission on the AGB, then absorption on the post-AGB, and back to emission in the Planetary Nebula phase, where the envelope is again optically thin (Kwok 1993). This is another clue to the evolutionary status of individual targets that we will use in our sequencing. The presence, shape and strength of these features can provide evidence of grain growth processing (Gielen et al. 2008). The ratios of these lines can yield temperatures for individual species, and even geometry of the dust shell (Molster et al. 2002a).

C-rich sources will have a spectrum characterized by emission in the AIBs at 3.3, 6.2, 7.7, 8.6 and 11.3 μm (Hrivnak et al. 2007). There are also features at 20.1 μm (colloquially called the 21 μm feature) and 30 μm that are specific to carbon rich PPNs, which are

likely due to aliphatic carbon compounds (Zhang et al. 2010). The SiC feature at 11.3 μm has been shown to transition from emission to absorption and back to emission as the star evolves, much like the silicate features in O-rich stars (Speck et al. 2009). In both cases, this feature could be modeled as a convolution of emission and absorption lines, and the resultant parameter tested as a potential age indicator.

Using each of these parameters as potential measures of the maturity of the object, we can then search for correlations between maturity of the central source and other characteristics of the dust, such as excitation and chemical composition.

2.2.1 C-rich sources

As mentioned above, we have classified as C-rich the post-AGB sources that possess emission in the Aromatic Infrared Bands commonly attributed to PAHs, though more likely an amorphous mix of aromatic and aliphatic compounds (Kwok & Zhang 2011). An example of this emission is shown in Figure 2.6 In addition, a few sources have an emission complex at 21 μm, the source of which is debated but seems to be associated w/ the presence of the AIBs (see Cerrigone et al. 2011 for a thorough discussion). We know that the formation of AIBs requires a carbon-rich environment (Allamandola et al. 1985), and at first it was assumed that these "carbon-rich" post-AGB stars must have undergone a third dredge up that provided sufficient carbon to the circumstellar environment to make it carbon-rich (Straniero et al. 1997). Zhang et al. (2010) suggest that the carbon molecules first form as aliphatic compounds and then transform to aromatic as the star evolves. However, some have suggested an alternative pathway: it could be that the photodissociation of CO near a shock front (likely caused by the interaction of a super-fast post-AGB wind w/ the slower AGB wind) or due to hardening radiation form the central star in an O-rich environment could free up enough carbon to allow for the formation of the aromatic molecules that we observe in emission w/out the entire environment actually being carbon rich (Guzman-Ramirez et al. 2011; Guzmán-Ramírez et al. 2012). This is a hypothesis that we can test

w/ our data, since these two formation scenarios would clearly happen at different stages of evolution: if the carbon compounds are evolving from aliphatic (arising in the 21 and 30 μm emission) to aromatic (arising in several AIBs near 10 μm) as the star evolves, we should see a correlation in our data between the maturity of the source and the ratio of the aliphatic feature strengths to the aromatic feature strengths. If, however, these AIBs were forming as a result of photodissociation, the incidence of dual chemistry will instead spike at the latest evolutionary stages when the radiation from the central source becomes hard enough to photodissociate the CO (assuming the dissociation is a result of high energy photons from the star and not a shock due to wind-wind interactions). If the latter were true, then the dual chemistry sources would just be O-rich sources in the last evolutionary stage before PN, after the onset of ionization, and the true C-rich sources would only display the 30 μm feature.

In addition, there are several other spectral features in post-AGB stars that we have characterized in order to search for evolutionary diagnostics: the integrated strength of the 15-20μm plateau (proposed by Peeters et al. 2002 to be a blend of emissions due to bending modes of the C rings), a 15.8μm feature possibly due to a larger solid state molecule and that may be connected w/ the presence of the 21 μm features (Hrivnak et al. 2009), a C_2H_2 molecular feature seen in emission or absorption at 13.7 μm, and Amorphous SiC at 11.3 μm which can be seen in emission, absorption or some combination thereof as mentioned in Section 2.3.

2.2.2 O-rich sources

We characterize the O-rich targets in our sample by the presence of silicate features, including amorphous silicates (amorphous olivine at 9.8 and 18 μm; amorphous pyroxene at 10μm), crystalline silicates (forsterite (Mg_2SiO_4) and enstatite ($MgSiO_3$) at 11.3, 16.2, 19.7, 23.7, 28, and 33.6 μm), and silica at 9 and 21 μm. The ratio between 11.3/9.8 μm features can be seen as a measure of crystallinity (those being the purest of the crystalline

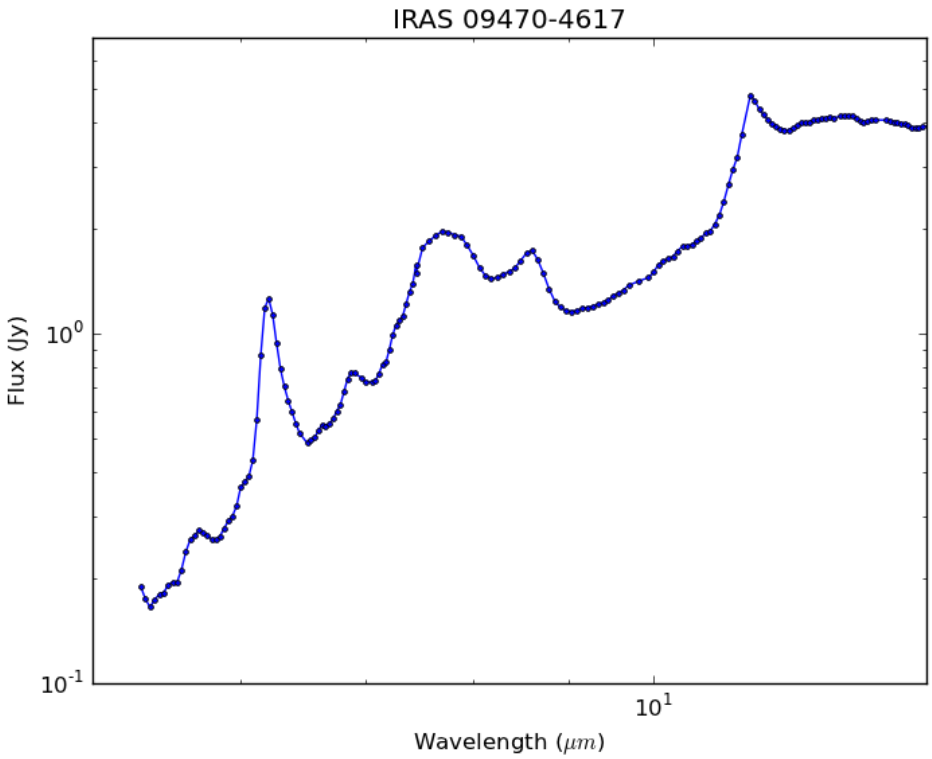

Figure 2.6 An example of AIB emission in a carbon-rich source, shown in log scale.

and amorphous silicate features, respectively; Gielen et al. 2008). Crystallinity is often considered a measure of dust grain processing under the assumption that the grains are formed as amorphous silicates and then crystallized by high temperature annealing as the central star heats up. Thus, we consider this ratio a potential indicator of evolutionary status to be included in our analysis.

2.3 Analysis

In order to get the necessary line strengths from the IRS spectra, we modified PAHfit (Smith & Draine 2012), which already includes the AIBs. To that, we added the silicate features described above, as well as the unidentified carbon features at 21 and 30 μm.

Defining a continuum in these sources is a challenge in the IRS wavelength window, where the dust features are broad and overlapping over the entire range. Thus, we chose to define the continuum as the best fitting sum of n blackbodies, where $0<n<10$. In this way we can avoid building in a systematic bias by our choice of continuum definition. A sample of the fit result is shown in Figure 2.7.

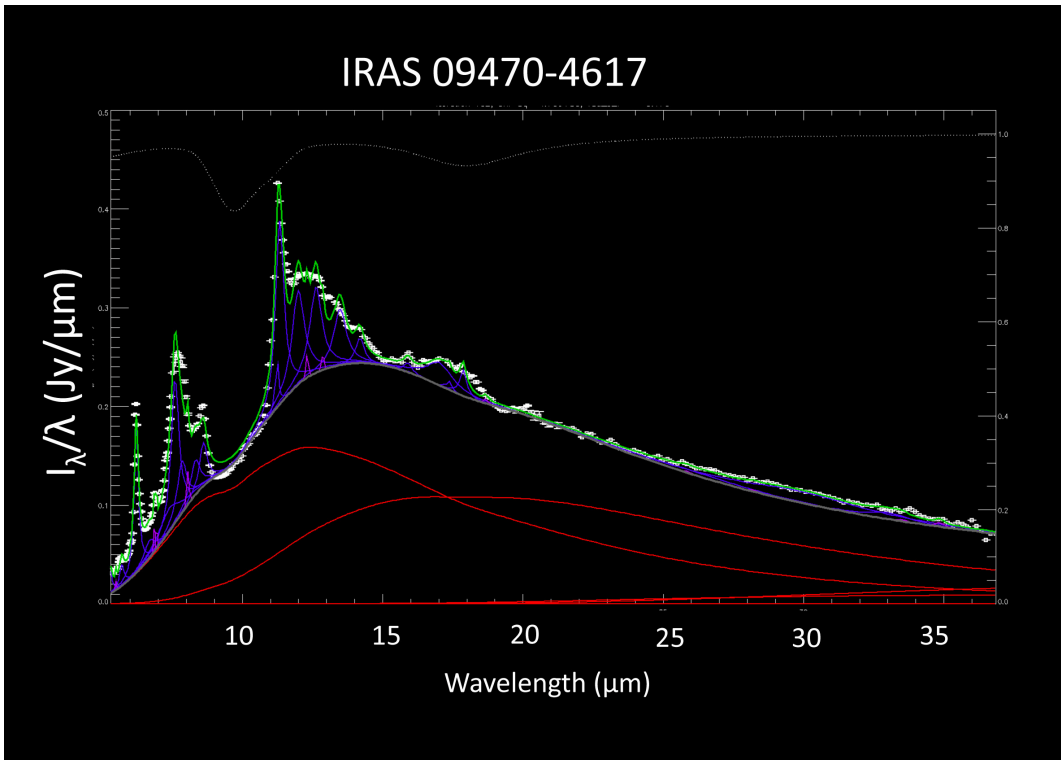

Figure 2.7 Example of a best fit found by our modified version of PAHfit. The white points are the Spitzer data. The components shown are dust continuum (red lines), AIBs (blue lines), and emission lines (purple lines). The green line shows the total model fit.

Table 2.3. Results of the modeling for Carbon rich sources with PAHfit. I. Integrated line fluxes

Identifier	$I_{12} + I_{12.6} + I_{13.5}$	$I_{11.3}$	$I_{11.2}$	$I_{7.6} + I_{7.8}$	$I_{6.2}$
IRAS 09470-4617	4.67E-08	3.36E-08	3.46E-09	4.69E-08	2.25E-08
IRAS 11353-6037	···	2.99E+11	3.36E+10	2.95E+11	1.69E+11
IRAS 11387-6113	4.54E+11	8.98E+11	···	1.62E+10	1.03E+11
IRAS 12145-5834	7.00E+10	1.06E+11	4.41E+10	3.02E+11	1.77E+11
IRAS 14482-5725	···	7.01E+11	2.52E+11	6.31E+11	3.30E+11
IRAS 15482-5741	3.45E+11	1.13E+12	3.68E+10	5.81E+10	···
IRAS 17376-2040	5.82E+11	6.02E+11	3.16E+10	4.73E+11	4.42E+11
IRAS 21546+4721	7.92E+11	7.35E+11	6.02E+10	8.16E+11	3.98E+11
IRAS 14429-4539	1.02E+14	2.00E+13	···	5.20E+13	5.96E+12
IRAS 01005+7910	4.02E+12	2.61E+12	5.66E+11	7.93E+12	5.41E+12
IRAS 17423-1755	3.09E+12	2.34E+11	···	3.20E+11	4.09E+11
IRAS 17542-0603	5.00E+10	9.46E+11	···	4.63E+11	6.78E+11
IRAS 18371-3159	···	2.63E+10	6.36E+10	6.98E+10	2.93E+10
IRAS 18379-1707	···	3.56E+11	3.23E+11	1.36E+12	7.85E+11
IRAS 20462+3416	···	5.92E+11	2.18E+11	2.06E+12	1.08E+12
IRAS 22023+5249	1.89E+11	1.75E+11	6.45E+10	8.13E+11	4.73E+11
IRAS 22495+5134	···	3.43E+12	···	1.82E+12	7.60E+11
IRAS 19306+1407	···	···	6.90E+10	3.69E+10	3.14E+10
IRAS 19336-0400	···	···	···	2.45E+11	1.30E+11
IRAS 19590-1249	1.78E+10	3.39E+11	3.92E+10	···	7.68E+10
IRAS 21289+5815	···	4.97E+11	1.01E+11	1.04E+12	4.67E+11
IRAS 19200+3457	···	1.41E+11	8.36E+10	7.71E+10	6.25E+10

Note. — Integrated line fluxes are in units of Jy/sec (W/m^2 $*10^{-26}$).

Table 2.4. Results of the modeling for Carbon rich sources with PAHfit.
II. Ratios of integrated line fluxes and estimated T_{EFF} of central stars.

Identifier	$\frac{I_{12}+I_{12.6}+I_{13.5}}{I_{11.3}}$	$\frac{I_{6.2}}{I_{11.3}}$	$\frac{I_{6.2}}{I_{11.2}}$	$\frac{I_{7.6}+I_{7.8}}{I_{11.2}}$	$\frac{I_{7.6}+I_{7.8}}{I_{11.3}}$	T_{EFF}
IRAS 09470-4617	1.39E+00	6.70E-01	6.50E+00	1.36E+01	1.40E+00	1.15E+04 ± 1.00E+03
IRAS 11353-6037	···	5.65E-01	5.03E+00	8.78E+00	9.87E-01	9.40E+03 ± 1.00E+03
IRAS 11387-6113	5.06E-01	1.15E-01	···	···	1.80E-02	8.70E+03 ± 3.00E+02
IRAS 12145-5834	6.60E-01	1.67E+00	4.01E+00	6.85E+00	2.85E+00	···
IRAS 14482-5725	···	4.71E-01	1.31E+00	2.50E+00	9.00E-01	8.90E+03 ± 3.00E+02
IRAS 15482-5741	3.05E-01	···	···	1.58E+00	5.14E-02	6.30E+03 ± 1.50E+02
IRAS 17376-2040	9.67E-01	7.34E-01	1.40E+01	1.50E+01	7.86E-01	6.60E+03 ± 3.00E+02
IRAS 21546+4721	1.08E+00	5.41E-01	6.61E+00	1.36E+01	1.11E+00	···
IRAS 14429-4539	5.10E+00	2.98E-01	···	···	2.60E+00	7.00E+03 ± 1.00E+02
IRAS 01005+7910	1.54E+00	2.07E+00	9.56E+00	1.40E+01	3.04E+00	6.80E+03 ± 1.00E+03
IRAS 17423-1755	1.32E+01	1.75E+00	···	···	1.37E+00	1.15E+04 ± 1.00E+03
IRAS 17542-0603	5.29E-02	7.17E-01	···	···	4.89E-01	5.10E+03 ± 8.00E+02
IRAS 18371-3159	···	1.11E+00	4.61E-01	1.10E+00	2.65E+00	1.60E+04 ± 3.50E+03
IRAS 18379-1707	···	2.21E+00	2.43E+00	4.22E+00	3.83E+00	1.60E+04 ± 3.50E+03
IRAS 20462+3416	···	1.82E+00	4.95E+00	9.45E+00	3.48E+00	1.60E+04 ± 3.50E+03
IRAS 22023+5249	1.08E+00	2.70E+00	7.33E+00	1.26E+01	4.65E+00	1.15E+04 ± 1.00E+04
IRAS 22495+5134	···	2.22E-01	···	···	5.29E-01	1.15E+04 ± 1.00E+04
IRAS 19306+1407	···	···	4.55E-01	5.35E-01	···	5.10E+03 ± 5.00E+03

To address the evolutionary status of these objects, the relevant values from these spectral fits are the strengths and ratios of certain gas-phase molecular AIB emission lines (Draine & Li 2007). One such ratio is that of the emission from AIBs attributed to ionized PAHs at 6.2 and 7.7 μm to the strength of the 11.2 and 11.3 μm features, which are due to neutral PAHs; these ratios are shown in Table 2.4. The C-H out-of-plane bending modes that produce emission features at 12, 12.6 and 13 μm are due to isolated aromatic rings, while the feature at 11.3 μm is produced by large groups of carbon atoms (on the order of 50). Thus, the ratio of these, shown in Table 2.4 as $\frac{I_{12}+I_{12.6}+I_{13.5}}{I_{11.3}}$, is a measure of the size of the emitting hydrocarbons. In principle, the ratio of features strengths due to aromatic compounds (all AIBs) versus those due to aliphatic ones (21 and 30 μm features) could also be an indicator of evolutionary status; unfortunately, this is not well quantified in our data because the 21 and 30 μm features are extremely broad and thus the measured strengths depend sensitively on our choice of continuum.

Though PAHfit worked well on the abundant AIB features in our carbon-rich stars, the silicates in our oxygen-rich stars were not faithfully reproduced w/ the model. This is probably due to the fact that the central wavelength and the fwhm of the silicate features is not consistent across all stars, and in our sources the feature is sometimes a superposition of emission and absorption, w/ the central wavelengths of the two slightly offset. Thus, we instead used a classification system to describe the appearance of the 10 μm silicate feature: Type I for sources w/ a simple gaussian-like emission line peaking at 9.8 μm (example shown in Fig. 2.8), similar to what is seen in the Inter Stellar Medium (ISM; Kemper et al. 2004; van Breemen et al. 2011), and Type II for those sources that appear to have a composite structure and peaking closer to 11 μm (such structure was associated in Molster et al. 2002a w/ the presence of a disk; see Figures 2.9 and 2.10); classifications of each source are shown in 2.2. The change in the profile of the silicate emission could be indicative of grain processing in a circumstellar disk (grain growth and thermal annealing of the amorphous silicates to crystalline forms), as Bouwman et al. (2001) have shown is the case for

Table 2.4 (cont'd)

Identifier	$\frac{I_{12}+I_{12.6}+I_{13.5}}{I_{11.3}}$	$\frac{I_{6.2}}{I_{11.3}}$	$\frac{I_{6.2}}{I_{11.2}}$	$\frac{I_{7.6}+I_{7.8}}{I_{11.2}}$	$\frac{I_{7.6}+I_{7.8}}{I_{11.3}}$	T_{EFF}
IRAS 19336-0400	···	···	···	···	···	1.60E+04 ± 3.50E+03
IRAS 19590-1249	5.25E-02	2.27E-01	1.96E+00	···	···	1.60E+04 ± 3.50E+03
IRAS 21289+5815	···	9.40E-01	4.62E+00	1.03E+01	2.10E+00	8.90E+03 ± 2.00E+02
IRAS 19200+3457	···	4.43E-01	7.48E-01	9.22E-01	5.47E-01	6.80E+03 ± 1.00E+03

Note. — Integrated line fluxes are in units of Jy/sec (W/m^2 $*10^{-26}$); the ratios are unit-less. T_{EFF} and estimated uncertainties are in degrees Kelvin.

the silicates in disks around Herbig Ae/Be stars. In addition, we detect crystalline silicate emission features at 23.7, 27.6, and 33.6 μm in many of our sources, which we label as having Type III silicates, as shown in 2.11 (also cataloged in 2.2). Molster et al. (2002a) found a prevalence of strong crystalline silicate bands in stars w/ expected disk-like geometries. Crystalline silicates can form in one of two ways around these sources: direct condensation in outflows or annealing. Crystalline silicates condense directly from the winds or quickly crystallize if the temperature at the dust condensation radius is above the glass transition temperature $T_g \approx 1000$ K (depending on gas pressure), which corresponds to a mass loss rate of $\gtrsim 2 \times 10^{-7}$ for conditions typical of oxygen-rich AGB circumstellar environments (Speck et al. 2008)). This mass loss rate is the very top of the range for for oxygen-rich AGB stars (van Loon et al. 2005), and thus in the vast majority of cases we expect silicates to condense in amorphous form (Speck et al. 2008). The best understood pathway for amorphous silicates to crystallize is high-temperature annealing, which would require dust to be held close to the star so that as the central star heats up along the post-AGB, these amorphous grains could be heated to the glass transition temperature. However, Molster et al. (1999) argue that there must be an alternate, low-temperature annealing mechanism that can take place in the presence of a long-lived circumstellar or circumbinary disk. In any case, crystalline slilicates can be considered highly processed dust grains in nearly all post-AGB sources, and their presence is further evidence that the dust responsible for the infrared emission is held in a stable reservoir near the star long enough for significant grain coagulation and annealing to take place (Molster et al. 1999). This is further supported by the strong correlation found by Molster et al. (2002a) between the presence of a highly flattened dust distribution ("disk-like sources") and a high degree of crystallinity among the emitting silicates.

We have eliminated from our post-AGB list two oxygen-rich sources that appear to be outliers, IRAS 18367-1233 and IRAS 18023-3409. IRAS 18367-1233 has a narrow silicate emission feature inside an absorption feature superposed on the 10 μm silicate emission

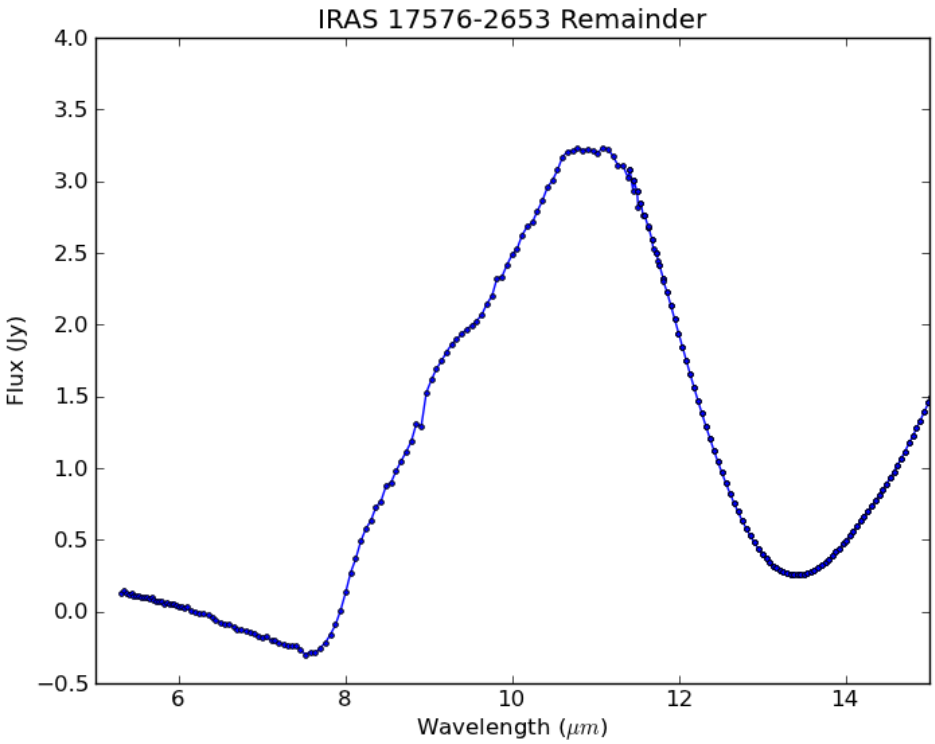

Figure 2.8 Example of a continuum subtracted 10 μm feature classified as Silicate Type I w/ a relatively smooth, gaussian-like emission profile.

(Figure 2.12); since this is unique among our sources we suspect this is not a post-AGB star. IRAS 18023-3409 has a P Cygni profile superposed on the 10 μm emission (Figure 2.13); we already suspected that this source was an LBV, and this seems to confirm that. As an aside, in many of the C-rich sources, we detect the 10 μm feature in absorption, but this is likely due to line of sight silicates in the ISM and not circumstellar dust. Please see Section 2.4 for further discussion.

2.4 Conclusions

To find correlations between our measured parameters and evolutionary status, it would be ideal to have at least one reliable baseline to measure against. In theory, the central star

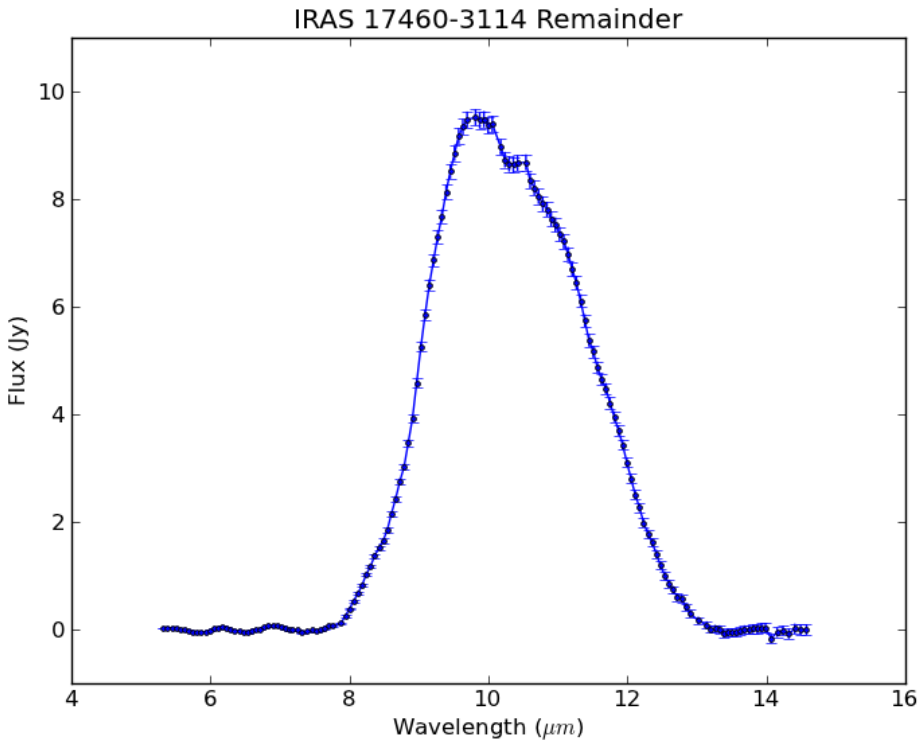

Figure 2.9 Example of a continuum subtracted 10 μm feature classified as Silicate Type II, w/ a composite structure of emission and absorption or a blended emission feature.

temperature would be excellent, since all stars increase in temperature as they evolve at this stage. Unfortunately, the central star temperatures are not well determined for these stars due to significant dust obscuration. Despite the fact that we chose a subset of sources for which there is a published spectral type, those are often derived from faint reflected starlight and have large uncertainties, corresponding to a temperature range spanning thousands of degrees Kelvin. Nonetheless, it is the best measure we currently have for a baseline, and as such we will compare our proposed evolutionary tracers w/ these values. Shown in Figures 2.14 to 2.16 are plots of observables that have been predicted as measures of evolutionary status. We do not find any correlations, which could be an artifact of the large error bars on the central star temperatures and does not necessarily disprove these theories.

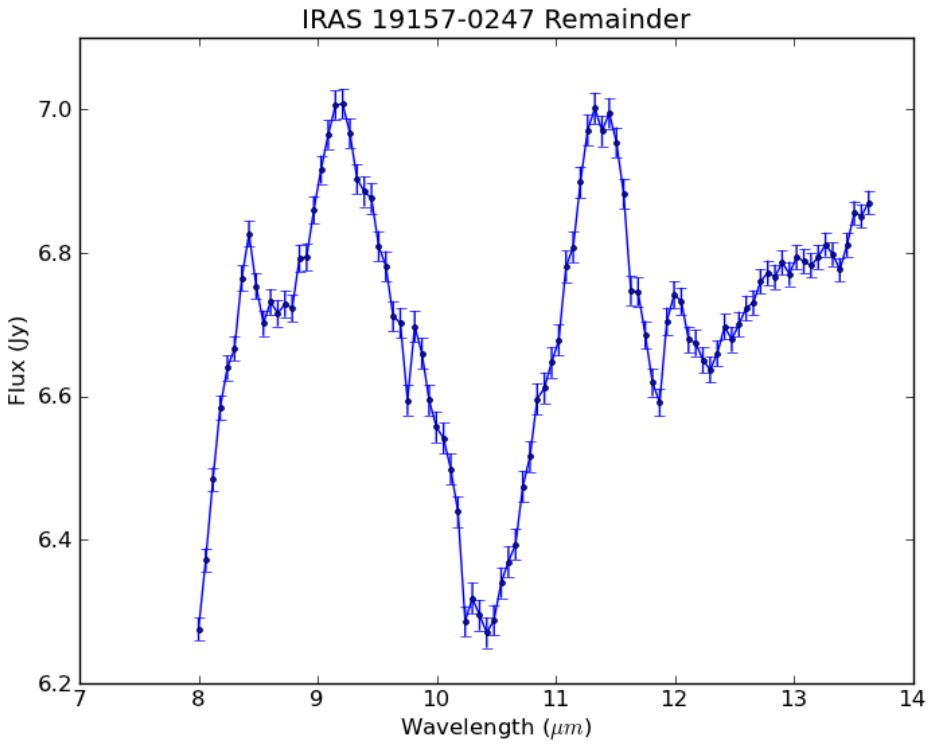

Figure 2.10 Example of the remainder after the continuum and a gaussian 10 μm bump has been subtracted. This source is classified as having Silicate Type II emission, w/ a composite structure of emission and absorption or a blended emission feature.

2.4.1 Ionization Fractions

Since we have chosen a sample of post-AGB stars that are just beginning to ionize their envelopes, the most direct measure of evolutionary status in our data is the ionization fraction. As the central star heats up, the ionization front travels outward through the circumstellar material, and thus in the simplest case of uniformly distributed material, the ionization fraction should increase linearly from the start of ionization to the edge of the envelope. Though this would be easy to track if we could watch a single object evolve over time, using this measure to place diverse sources on the same timeline is much more difficult. These sources vary in the extent of circumstellar material they harbor, the density and opacity of that material (and thus the radial velocity of the ionization front), and of

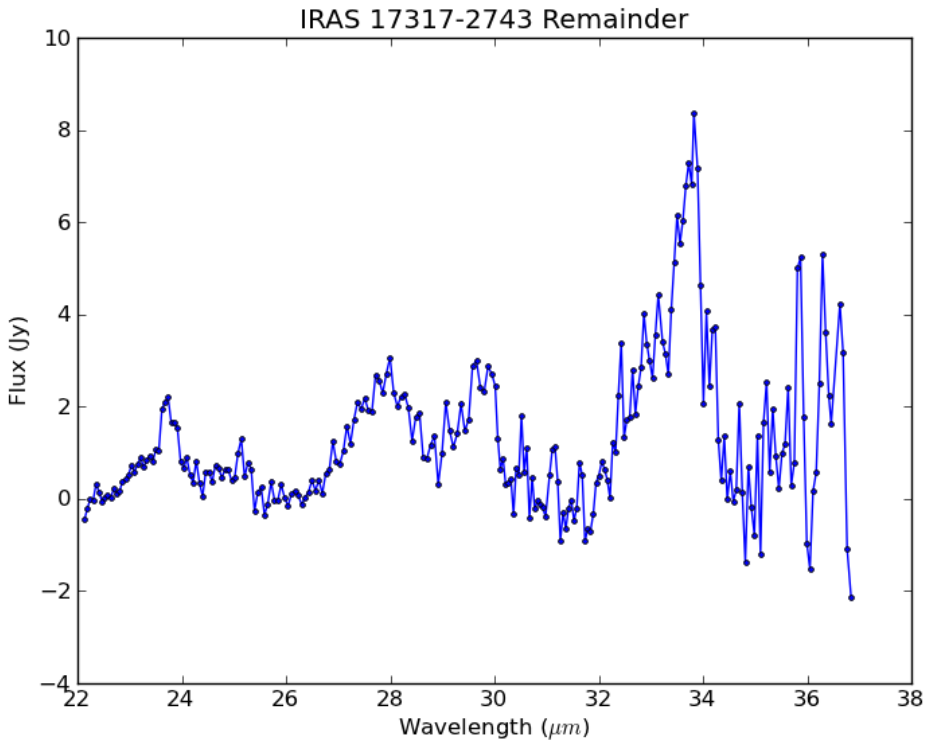

Figure 2.11 An example continuum-subtracted spectrum for an O-rich source, showing crystalline silicate emission lines at 23.7, 27.6, and 33.6 μm. This source is classified as having Silicate Type II emission.

course the mass of the central stellar remnant (which affects the rate at which the heating progresses, again affecting the speed of the ionization front). In our analysis, we measure the ionization of the grains responsible for the AIB emission by comparing the strengths of the features attributed to neutral PAHs versus those attributed to ionized PAHs. This is not necessarily a measure of the ionization fraction of the circumstellar envelope as a whole; the correlation between these two quantities depends on the spatial distribution and the formation pathway of the emitting PAHs. Nonetheless, we are able to confirm a correlation between our two measures of the ionization fraction of the PAHs in the carbon-rich sources, which is a good sanity check, and may indicate that the ionization fraction is a better measure of evolutionary status than the existing T_{EFF} estimates. The only other evolutionary

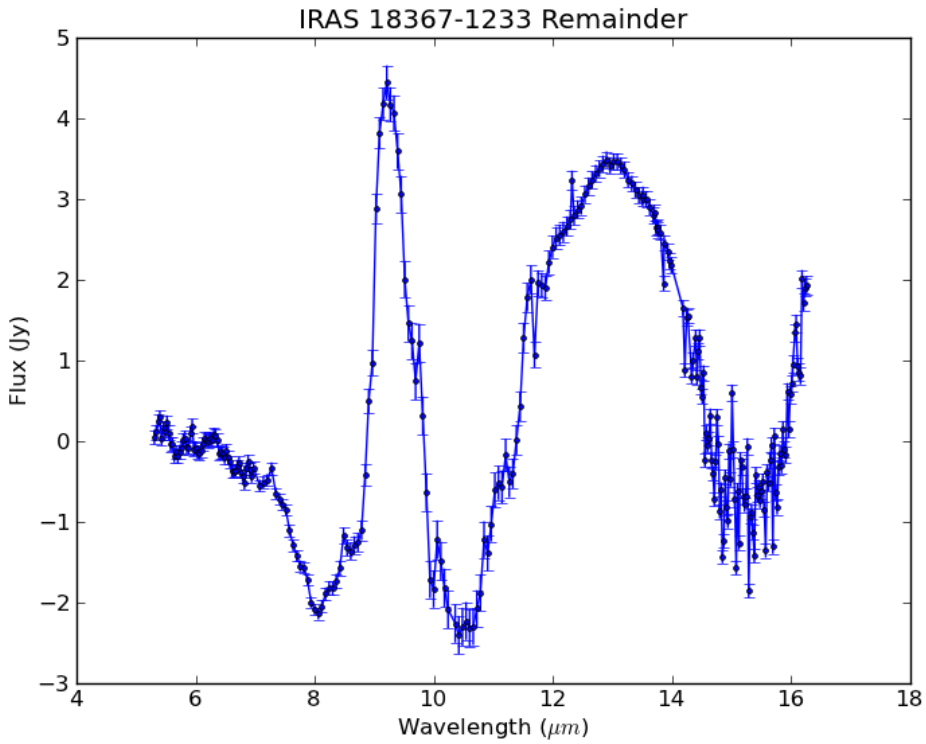

Figure 2.12 The remainder for IRAS 18367-1233 at 10 μm after subtraction of the continuum and the gaussian 10 μm bump.The unusual structure of this silicate emission has led us to conclude that this source is not a post-AGB star.

indicator we have for the C-rich sources is the ratio that is a measure of the growth of the AIB-emitting grains (commonly attributed to PAHs). We have plotted the ionization fraction versus this measure (see Figure 2.18). Though we do see a potential correlation, our sample is small enough that we cannot confirm this. It should be noted that the growth of AIB grains should be quenched once the star gets hot enough to photodissociate them, so we do not expect an indefinite linear increase in this measure. Additionally, the ionization fraction will not increase linearly even in the case of a single star, though we can say in general terms that it should increase as the central star heats up.

Overall, we do not detect convincing evidence for the correlation between any of our proposed evolutionary measures and the T_{EFF} of the central star. However, due to large

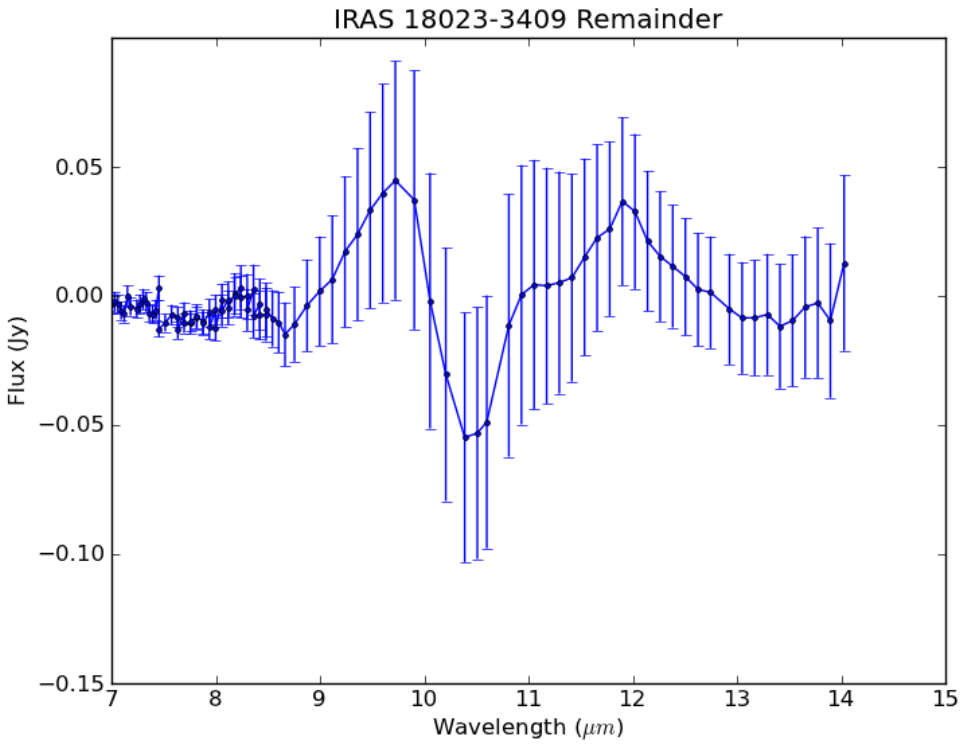

Figure 2.13 The remainder for IRAS 18023-3409 at 10 μm after subtraction of the continuum and the gaussian 10 μm bump. The unusual structure of this silicate emission has led us to conclude that this source is not a post-AGB star.

uncertainties is this temperature, any one of these measures or some combination of them might still be an observational diagnostic of evolutionary status. To find such a correlation, we need to do a systematic search for correlations among the evolutionary measures, discussed in detail in the Conclusion chapter.

2.4.2 Grain processing

We do, however, detect significant emission from highly processed dust grains; overall, 75% of our sources show emission from crystalline silicates or large groups of hydrocarbons. This is strong evidence for the presence of a stable dust structure near the central stars in the majority of our sources, particularly the hottest sources (over half of which have

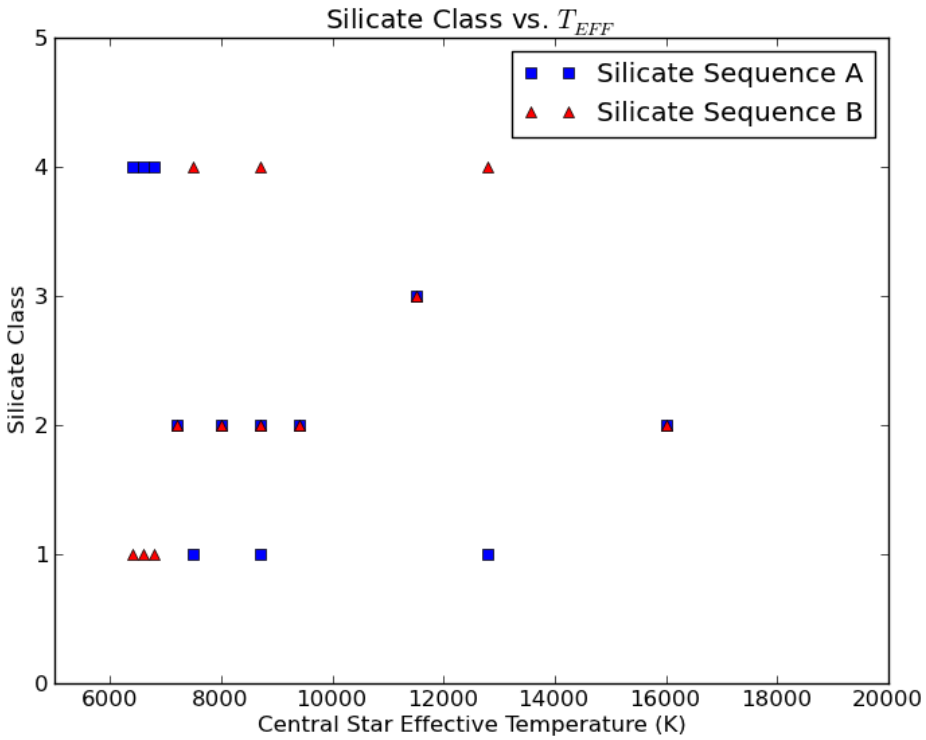

Figure 2.14 Silicate Classes versus T_{EFF} of the central star. The Silicates were placed into two sequences to check for correlation w/ evolution. Silicate Sequence A (I, I & III, II, III) would represent silicates forming as amorphous grains and becoming more crystalline as the central star heats up. This is the sequence that has the most observational evidence, but we do not see a correlation in our (admittedly small) sample. Silicate Sequence B (III, I & III, II, I) produces a more plausible correlation w/ central star temperatures, but there is no physical basis for this sequence.

mixed chemistry; Gielen et al. 2011). We cannot distinguish between a rotating disk and a dusty density-enhanced waist w/ our data, but either case strongly suggests the presence of a binary companion because models of the formation scenarios of such structures favor binarity (Nordhaus et al. 2010).

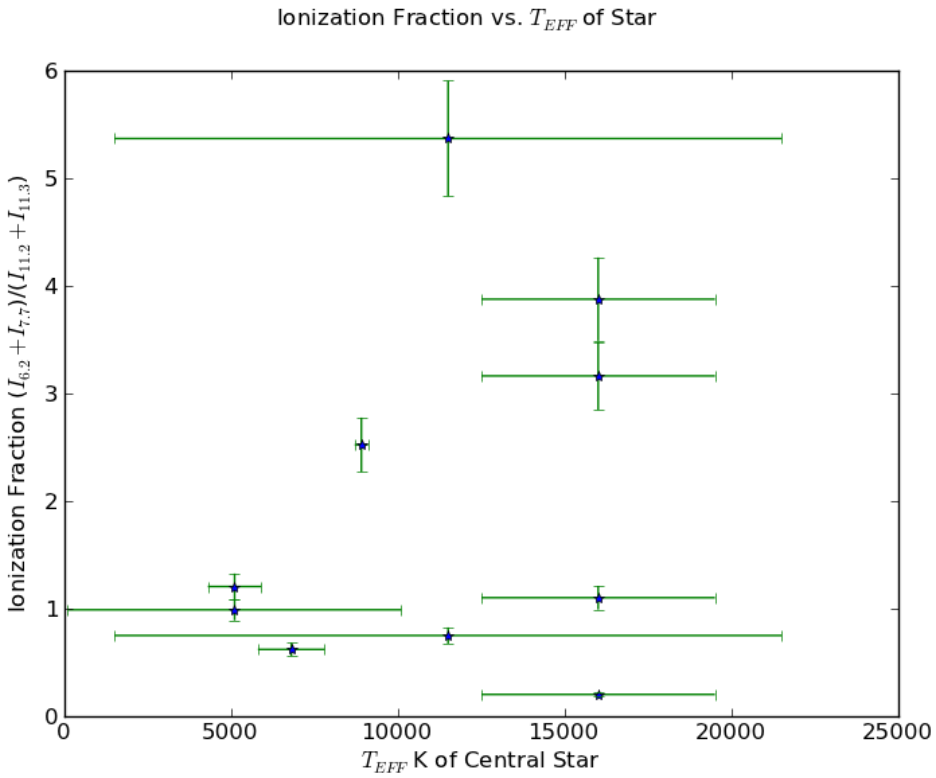

Figure 2.15 The ionization fraction of the aromatic hydrocarbons versus the T_{EFF} of the central star, based on published spectral types. Due to the severe dust obscuration of the central star, these spectral types are quite uncertain; as shown here, there is no correlation w/ the ionization fraction as one might expect if these temperatures were a reliable estimate of evolutionary status.

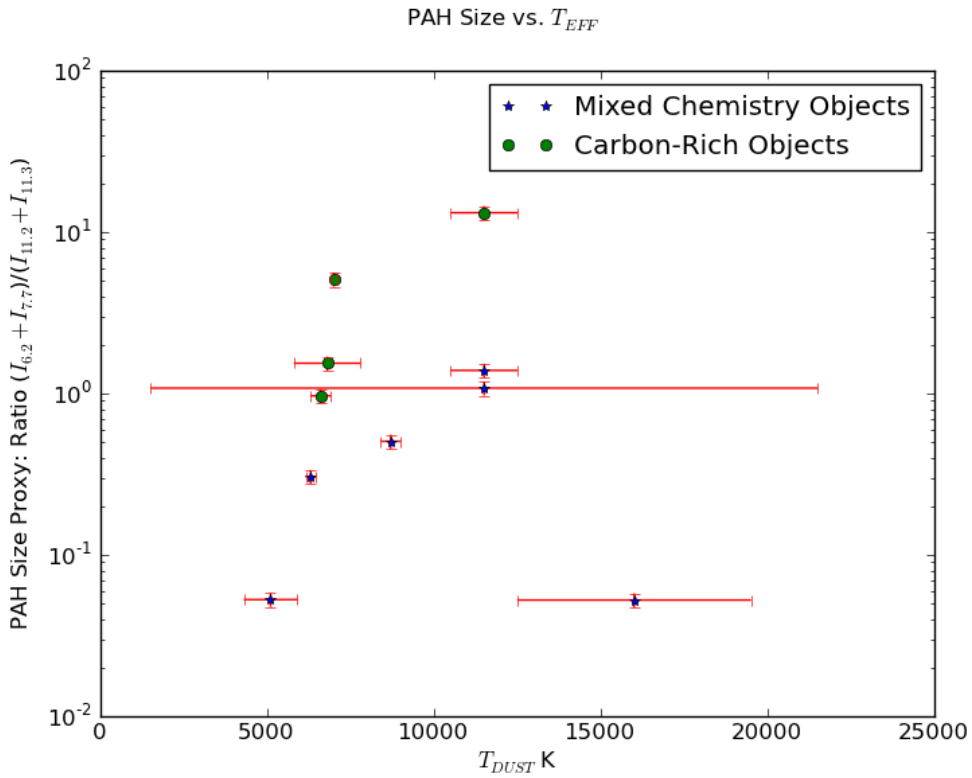

Figure 2.16 A proxy of the size of the emitting aromatic hydrocarbons versus the T_{EFF} of the central star, based on published spectral types. If the aromatic hydrocarbons are forming as a result of the photodissociation of CO, we would expect to see their size increase initially as the central star warms, but then as the radiation from the central star hardens they should be destroyed and taper off in size.

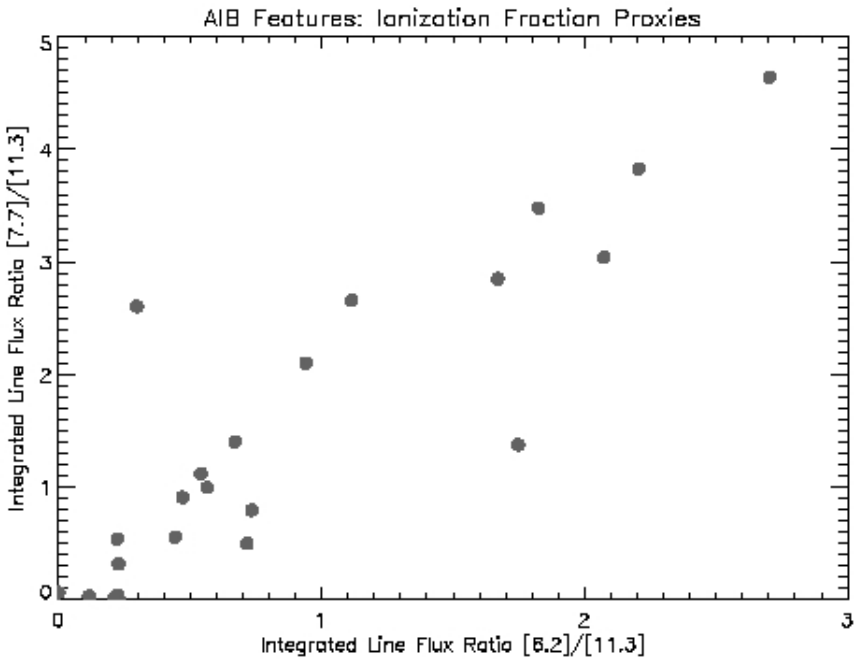

Figure 2.17 Two independent measures of the ionization fraction of the aromatic hydrocarbons.

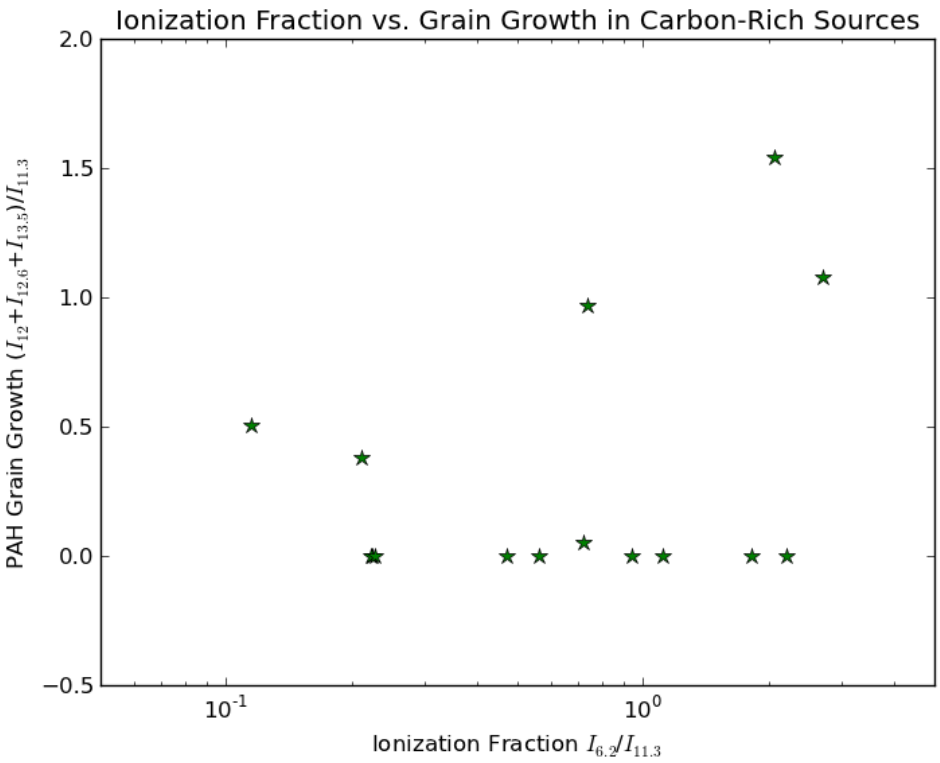

Figure 2.18 The ionization fraction of the aromatic hydrocarbons plotted against the grain size of the same grains.

Chapter 3

A Spitzer Imaging Survey of Post-AGB Stars

In addition to the spectra, an imaging survey of the same sources was performed using the Infrared Array Camera (IRAC; Fazio et al. 2004) onboard the Spitzer Space Telescope (Programs 30036, 40115, and 50116; Werner et al. 2004). We have, for the first time, resolved the extended emission around several of the post-AGB stars, as well as discovered new nebular structures around some Planetary Nebulae.

3.1 Data

The same sample of 70 targets spanning the range from post-AGB star to Planetary Nebulae were observed. These stars were chosen to span the evolutionary transition from post-AGB star to Planetary Nebula. The post-AGB stars in this sample were first identified as post-AGB candidates on the basis of the IRAS colors (Parthasarathy & Pottasch 1986), and later confirmed with the addition of optical spectroscopy (Parthasarathy et al. 2000; Suárez et al. 2006). In order to target the late-stage post-AGB stars, a subset of post-AGB candidates with hot (Spectral Type F, A or B) central stars was chosen from among the lists

of candidates. The effective temperature range for the central stars, based on spectroscopic types, is 5,100–29,000 K.

3.1.1 Observations & Data Reduction

To search for extended emission among these objects, they were imaged using the infrared array camera (IRAC) on Spitzer in four broadband channels centered at 3.6, 4.5, 5.8, and 8.0 μm. The images were taken in a high dynamic range (HDR) mode, so each object was imaged with a short and a long exposure. The majority of the compact sources (candidate post-AGBs; PID 30036, 50116) were taken using 12 and 0.6 sec exposures in a medium-sized dither pattern. A few of the brightest targets were taken using subarray mode, which uses only a subset of the array but more frequent sampling, to avoid saturation (with a larger dither pattern). The PNe (PID 40115) were taken in HDR mode with longer exposures in general. Table 3.1 details the exposure times and the corresponding sensitivities for each source. Only the PNe and non-standard post-AGB cases are listed, with the last line labelled "Remainder" describing the standard exposure times and sensitivities for all candidate post-AGB sources not listed.

Table 3.1. IRAC Image Sensitivities

Target	Observing Mode	T_{EXP} sec	N_{EXP}	3.6 μm MJy/sr	4.5 μm MJy/sr	5.8 μm MJy/sr	8.0 μm MJy/sr
NGC 1501	IRAC HDR Map	30/1.2	20	0.00376	0.00504	0.0204	0.0229
PN M 2-31	IRAC HDR Map	12/0.6	12	0.0114	0.013	0.0445	0.0476
PN M 2-20	IRAC HDR Map	30/1.2	12	0.00486	0.00651	0.0264	0.0295
NGC 40	IRAC HDR Map	30/1.2	12	0.00486	0.00651	0.0264	0.0295
PN PB 6	IRAC HDR Map	30/1.2	12	0.00486	0.00651	0.0264	0.0295
NGC 2867	IRAC HDR Map	12/0.6	12	0.0114	0.013	0.0445	0.0476
PMR 2	IRAC HDR Map	30/1.2	12	0.00486	0.00651	0.0264	0.0295
NGC 7026	IRAC HDR Map	12/0.6	12	0.0114	0.013	0.0445	0.0476
PN PB 8	IRAC HDR Map	30/1.2	12	0.00486	0.00651	0.0264	0.0295
Hen 2-99	IRAC HDR Map	30/1.2	12	0.00486	0.00651	0.0264	0.0295
PMR 1	IRAC HDR Map	30/1.2	40	0.00266	0.00356	0.0144	0.0162
Abell 30	IRAC HDR Map	30/1.2	60	0.00217	0.00291	0.0118	0.0132
PN M 4-18	SubArray	0.4	16	0.0316	0.0216	0.109	0.0399
NGC 5315	SubArray	0.4	16	0.0316	0.0216	0.109	0.0399
Hen 2-459	SubArray	0.4	16	0.0316	0.0216	0.109	0.0399
PN PM 1-310	SubArray	0.4	16	0.0316	0.0216	0.109	0.0399
iras 17460	SubArray	0.1	36	0.121	0.108	0.239	0.0817
iras 18435	SubArray	0.1	36	0.121	0.108	0.239	0.0817
iras 19157	SubArray	0.1	36	0.121	0.108	0.239	0.0817
Remainder	IRAC HDR Map	12/0.6	16	0.00992	0.0113	0.0385	0.0412

Note. — Sensitivities correspond to a 1-σ detection of extended emission. For the High Dynamic Range (HDR) observations, N_{EXP} corresponds to the number taken at each of the listed exposure times.

The IRACproc software (Schuster et al. 2006) ver. 4.3 was used to produce mosaics from the individual frames. Raw Basic Calibrated Data (BCD) files were first run through the fixup routine, then mkmopex_bcd, then visually inspected for cosmic rays and other image issues related to saturation. The most corrupted frames were either thrown out or corrected with the tools provided in the IRACproc suite. Finally, I ran the mkmosaic_bcd routine, which aligns the individual pointings to make one mosaic for each wavelength channel, all with the same pixel size of 0.6 arc seconds per pixel.

Many of the long exposure images were saturated by the central star, so the search for extended emission was complicated by image corruption. Nevertheless, in some cases it was possible to subtract the point spread function and recover the emission from circumstellar material. To perform the psf subtraction, we again made use of the IRACproc software

Schuster et al. (2006), which employs a PSF derived from observations of calibration stars and other IRAC programs Marengo et al. (2009) and was sampled to match the pixel scale of our mosaics. The sources for which we detected extended emission in at least one IRAC channel are IRAS 19590-1249, IRAS 11353-6037, IRAS 10082-5647, IRAS 18070-2346, IRAS 19399+2312, SAO 243233 and SAO 227229; these are shown in Figures 3.1 to 3.7.

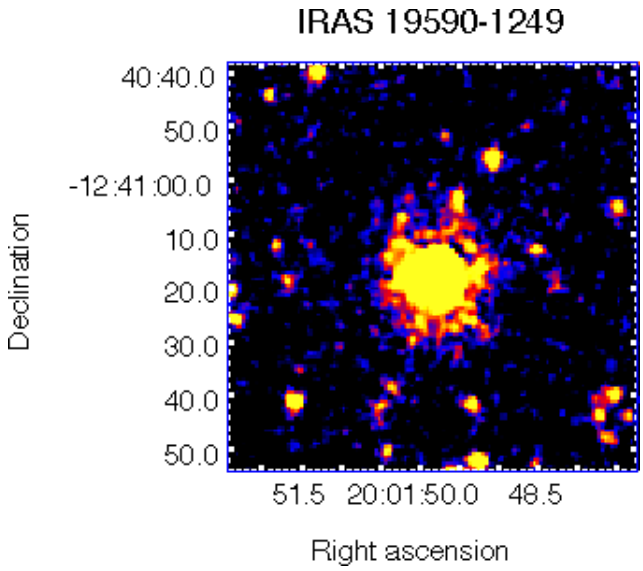

Figure 3.1 Extended emission around IRAS 19590-1249 in IRAC Ch.2, after PSF subtraction. Shown in log scale (centered at 3.6 μm).

IRAC Photometry

To extract the photometry from the mosaics, we used a routine that is part of the IRACproc suite of analysis tools called nsphot, which utilizes IRAF photometry and coordinate transformation tools. The routine applies aperture photometry to all sources in each mosaic, which are then matched up to our source list. The aperture used for this procedure has a 4-pixel radius, which corresponds to an angular size of 2.4 arc seconds in our mosaics. This routine works optimally for unsaturated, unresolved point sources, which is true of most of our targets (for most of the brightest targets we extracted photometry from the short exposure frames where the detector was unsaturated). A few of the targets were

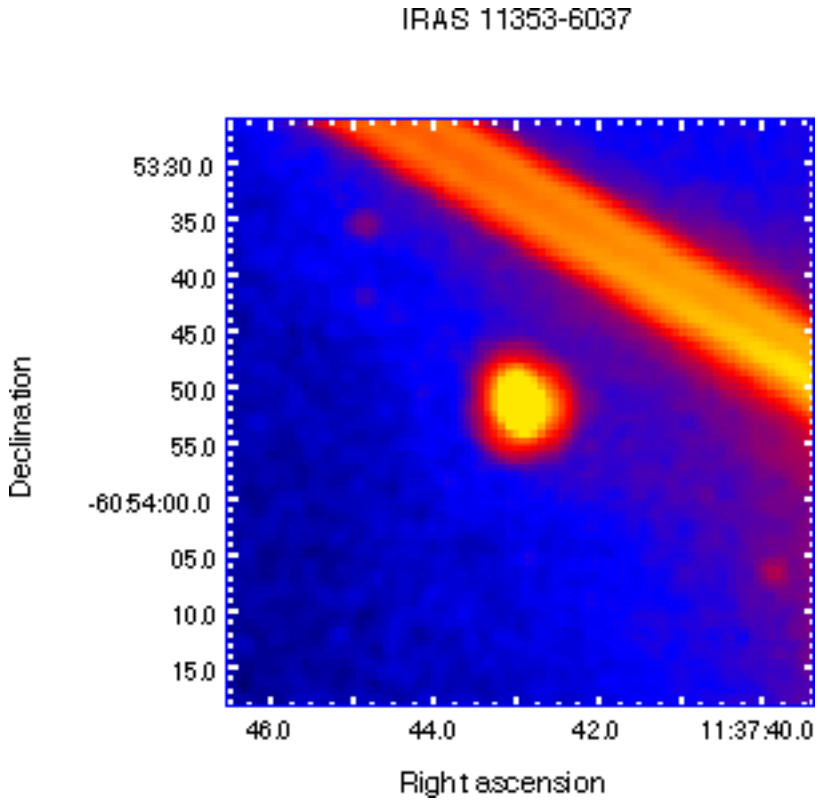

Figure 3.2 Resolved structure of IRAS 11353-6037 in IRAC Ch.4, shown in log scale (centered at 8 μm). The diagonal bar in the upper right corner is an image artifact from a nearby bright source.

too bright even for the short exposures; for these cases we instead performed a subtraction of the point spread function (psf) using a routine called psf_sub that is part of the IRACproc suite of tools. We used this routine to subtract an oversampled model psf from the image, adjusting the magnitude of the psf until the wings of the diffraction spikes a perfectly subtracted to the background noise level. The results of this procedure resulted in differences of 2% or less to those obtained with aperture photometry. The resulting fluxes are listed in Table 3.2 according to the standard IRAC magnitude convention described in Reach et al. (2005). The zero-magnitude flux densities are $280.9 \pm 4.1, 179.7 \pm 2.6, 115.0 \pm 1.7$, and 64.13 ± 0.94 Jy in the [3.6], [4.5], [5.8], and [8] μm channels, respectively.

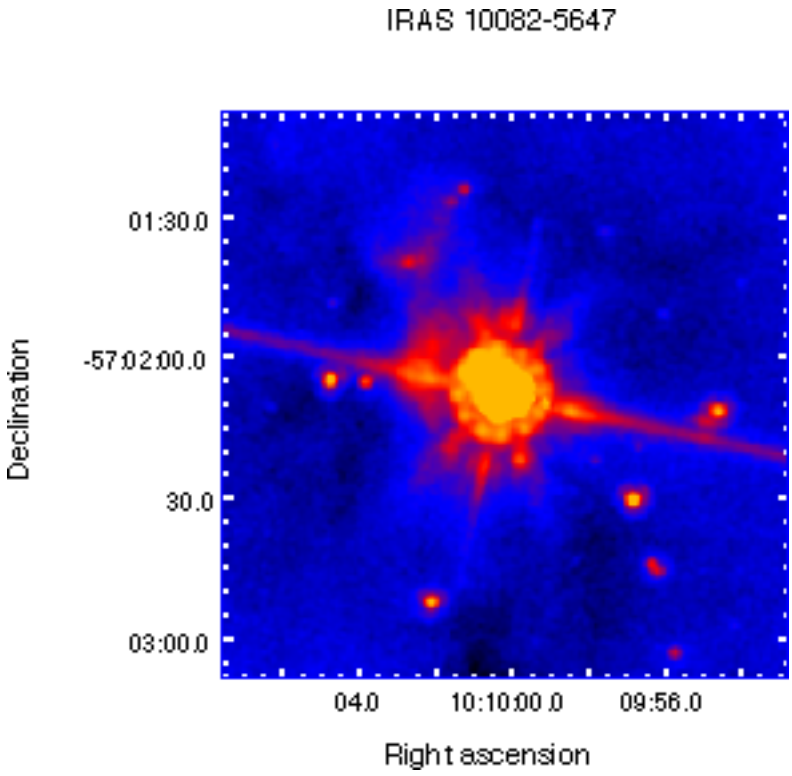

Figure 3.3 Extended emission around IRAS 10082-5647 in IRAC Ch.4, shown in log scale (centered at 8 μm). This target has been identified as a Herbig-Haro object in the most recent post-AGB catalog by Sczerba et al. 2007. The diagonal line seen here is a bright source artifact that occurs in this channel.

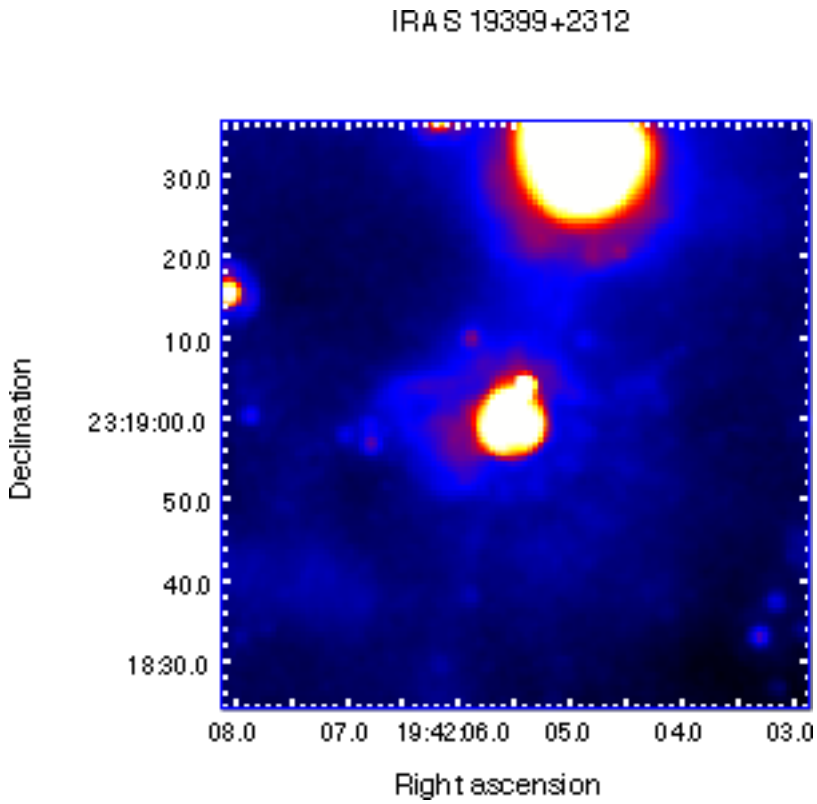

Figure 3.4 Extended emission around IRAS 19399+2312 in IRAC Ch.4, shown in log scale (centered at 8 μm). Based on the spectrum of this source, we have determined that it is not a post-AGB.

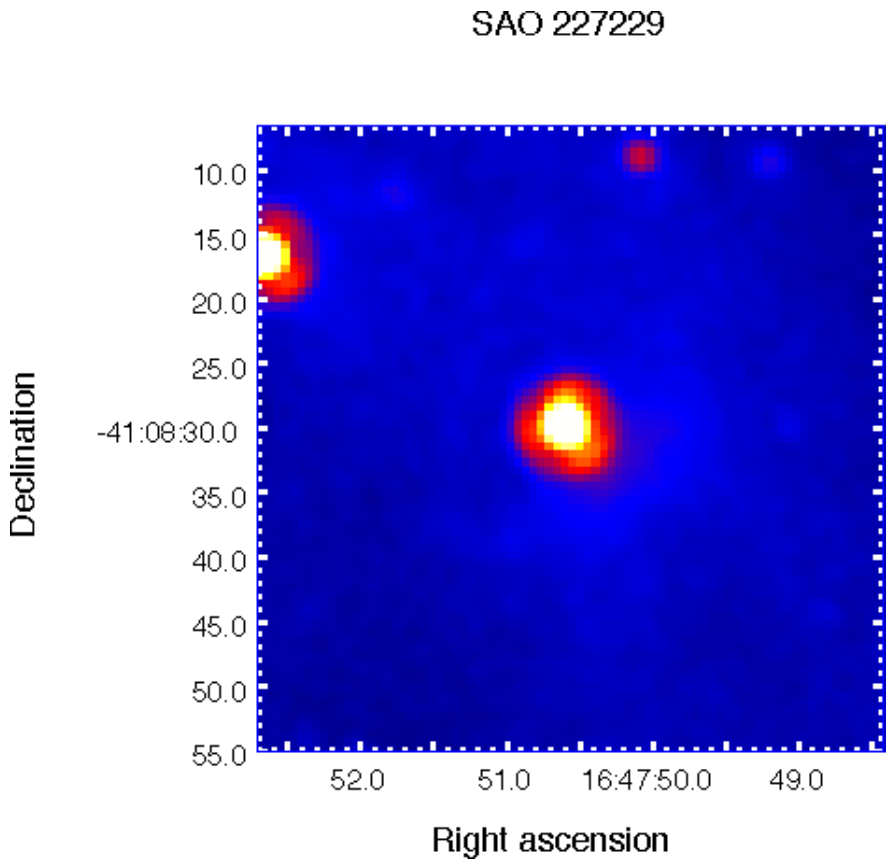

Figure 3.5 Extended emission around SAO 227229 in IRAC Ch.4, shown in log scale (centered at 8 μm). Due to the line of sight proximity to an H II region, this star may be a Young Stellar Object. This object is very faint, but the spectrum is very similar to other post-AGBs in our sample, so we have not removed it from our post-AGB list.

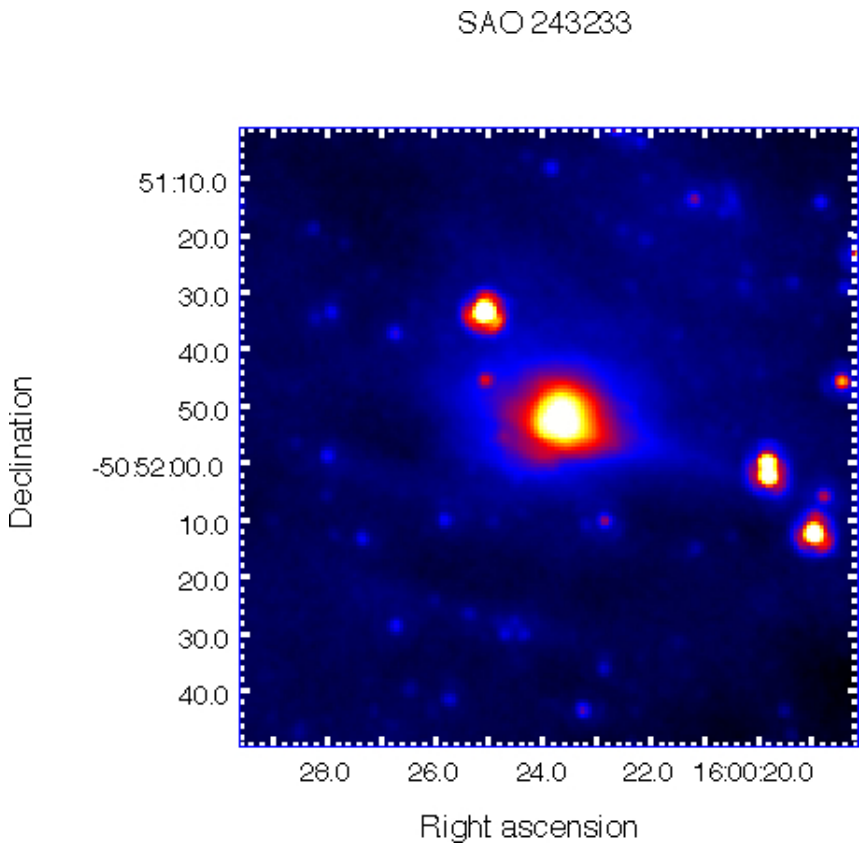

Figure 3.6 Extended emission around SAO 243233 in IRAC Ch.4, shown in log scale (centered at 8 μm). Due to the line of sight proximity to an H II region, this star may be a Young Stellar Object. The spectrum suffers from low signal to noise, but it is very similar to other post-AGB spectra in our sample so we have not eliminated it from the post-AGB candidates.

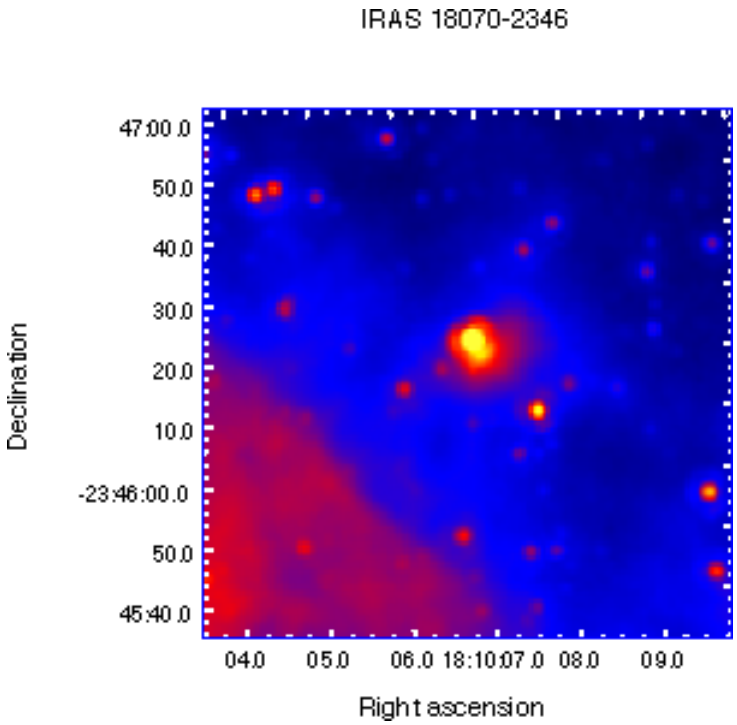

Figure 3.7 Extended emission around IRAS 18070-2346 in IRAC Ch.4, shown in log scale (centered at 8 μm). This object also appears to be a YSO based on the spectrum and its coincidence in the line of sight with an H II region.

Table 3.2. Photometric data derived from IRAC images.

Identifier	$m_{3.6}$ (mag)	$m_{4.5}$ (mag)	$m_{5.8}$ (mag)	$m_{8.0}$ (mag)	$SpectralType$ (Suarez et al. 2006)	$SpectralType$ (SIMBAD)
SAO 152360	7.829 ± 0.004	7.896 ± 0.005	8.074 ± 0.013	8.113 ± 0.011		B2/B3II
IRAS 10082-5647	5.495 ± 0.001	4.796 ± 0.001	4.078 ± 0.002	3.043 ± 0.001		Be
IRAS 11201-6545	9.472 ± 0.008	9.292 ± 0.009	9.302 ± 0.024	7.278 ± 0.008	A3Ie	
IRAS 11353-6037	10.015 ± 0.014	9.944 ± 0.015	8.922 ± 0.023	7.203 ± 0.008	B5Ie	
IRAS 11387-6113	8.396 ± 0.005	8.234 ± 0.006	8.120 ± 0.014	6.979 ± 0.007	A3Ie	
IRAS 12145-5834	11.465 ± 0.020	11.195 ± 0.024	9.479 ± 0.026	7.706 ± 0.009	em	
IRAS 12175-5338	7.906 ± 0.004	7.916 ± 0.005	8.012 ± 0.013	6.954 ± 0.007		F2
IRAS 13245-5036	11.289 ± 0.060				A7-9Ie	
IRAS 14325-6428	8.366 ± 0.005	8.254 ± 0.006	7.739 ± 0.011	5.645 ± 0.004	F5I	
IRAS 14429-4539	6.691 ± 0.002	5.549 ± 0.002	4.103 ± 0.002	2.659 ± 0.001	F4Ie	M
IRAS 14482-5725	7.563 ± 0.003	7.168 ± 0.003	6.498 ± 0.006	4.844 ± 0.002	A2I	
IRAS 15482-5741	9.562 ± 0.008	9.404 ± 0.010	8.635 ± 0.018	6.450 ± 0.005	F7I	
SAO 243233	8.476 ± 0.005	8.502 ± 0.006	8.536 ± 0.017	7.929 ± 0.011		B3II/III
SAO 243756	8.591 ± 0.005	8.469 ± 0.006	8.470 ± 0.016	8.029 ± 0.011	A3Ie	A3Iab:e
SAO 227229	8.934 ± 0.006	9.003 ± 0.008	9.156 ± 0.022	9.193 ± 0.019		B1/B2Ib
SAO 244567	11.153 ± 0.017	10.246 ± 0.015	10.381 ± 0.041	8.404 ± 0.013	PN	B3e
IRAS 17317-2743	8.238 ± 0.004	8.091 ± 0.005	8.163 ± 0.014	7.546 ± 0.009	F5I	
IRAS 17376-2040	5.762 ± 0.001	5.099 ± 0.001	4.435 ± 0.002	3.682 ± 0.001	F6I	

Table 3.2 (cont'd)

Identifier	$m_{3.6}$ (mag)	$m_{4.5}$ (mag)	$m_{5.8}$ (mag)	$m_{8.0}$ (mag)	$SpectralType$ (Suarez et al. 2006)	$SpectralType$ (SIMBAD)
IRAS 17488-1741	9.061 ± 0.006	8.887 ± 0.008	8.986 ± 0.021	8.956 ± 0.017	F7I	
IRAS 17576-2653	8.997 ± 0.006	8.774 ± 0.007	8.219 ± 0.014	5.263 ± 0.003	A7I	
IRAS 18023-3409	10.008 ± 0.010	9.464 ± 0.010	9.048 ± 0.021	7.358 ± 0.008		B2IIIe
IRAS 18237-0715	4.408 ± 0.001				B5-B9	B5-B9
IRAS 16206-5956	8.599 ± 0.005	8.469 ± 0.006	8.468 ± 0.016	8.033 ± 0.011	A3Ie	A3Iab:e
M4-18	9.131 ± 0.008	8.709 ± 0.009	6.664 ± 0.009	4.384 ± 0.002		
PM1-310	10.436 ± 0.015	9.615 ± 0.013	8.372 ± 0.019	6.287 ± 0.006		
He2-459	8.600 ± 0.006	8.023 ± 0.006	6.267 ± 0.007	4.180 ± 0.002		
NGC 5315	7.815 ± 0.004	7.190 ± 0.004	6.408 ± 0.008	4.104 ± 0.002		

3.2 Results

The imaging provides two key pieces of information on these systems: the extent and morphology of the shell (an upper limit of 5 arcsec on the angular size for unresolved objects), and the photometric flux in each of the channels. Though we did not resolve enough of the objects to include morphology or dust shell extent in our statistical analysis, we can test if our data is consistent with the hypotheses relating chemistry and morphology. In addition to our photometry and spectra, we collected photometric data published on these objects from the literature to increase the wavelength coverage for the formal modeling of the Spectral Energy Distribution. Sources for this photometry include the point source catalogs from IRAS (channels centered at 12, 25, 60 and 100 μm ; Neugebauer et al. 1984), 2MASS (channels centered at 1.25, 1.65 and 2.17 μm ; Skrutskie et al. 2006), SIMBAD UBVR magnitudes, and AKARI FIS (channels centered at 65, 90, 140, and 160 μm ; Yamamura et al. 2009, 2010).

3.2.1 Modeling the Spectral Energy Distribution

To solve the problem of radiative transfer in the dust shells around these stars, we recreated the observed Spectral Energy Distributions (SEDs) for each source using a the DUSTY code (Ivezic 1999). DUSTY takes as input the temperature of the central star as well as several properties of the dust shell; in our case, as a first run, we specified:

1. Central source: blackbody curve with temperature matching the spectral type of the target $T_\star$;
2. Chemistry of the envelope: either 100% silicates or 100% amorphous carbon, depending on IRS features (Chemistry);
3. Grain size distribution: power law $a^{-3.5}$, $a_{min} = 0.005$, $a_{max} = 0.25$, a being the grain radius in μm ($a_{min\&max}$ varied, but not the power law exponent);
4. Density distribution: power law proportional to R^{-2}, R being the shell radius;

5. Shell relative thickness: $R_{out} = 1000 R_{in}$;
6. Dust temperature at R_{in}: adapted to each SED (T_{dust});
7. Optical depth at 60 μm : calculated for each star from IRAS data (τ_{60}).

Each model was then iterated to find the best fit; in order to simulate multiple dust components, the model was run multiple times in succession, working outward with the output from the previous model entered as the central radiation source. (see the results for the subset of sources that have completed modeling in Table 3.3; Cerrigone et al. 2009).

Table 3.3. Results of SED modeling

Target	$T_\star$ (K)	Chemistry	Grain Size (μm)	T_{dust} (K)	R_{out}/R_{in}	τ_{60} (μm 10^{-4})
C-rich spectra						
01005+7910	20300	am-C	0.005-0.26	700	1000	0.16
			0.005-2.5	145	20	7
06556+1623	20000	Sil-Ow 15%, am-C 85%	0.005-0.26	900	1000	0.61
		Sil-DL	0.005-2	135	1000	3
09470-4617	20000	am-C	0.005-0.26	900	1000	0.2
				220	20	2
17423-1755	20000	am-C	0.005-100	1150	445	135
				132	2	80
				80	2	100
18442-1144	20000	am-C	0.005-0.26	280	2	0.4
		Sil-Oc		110	1000	20
19200+3457	7000	am-C	0.005-0.26	380	1000	0.27
		am-C 80%, Sil-Oc 20%		110	5	3.2
12145-5834	23000	am-C	0.005-0.26	125	10	15
		am-C		350	3	0.10
13245-5036	15000	am-C	0.005-0.26	250	100	100
		am-C		50	10	0.15

Table 3.3 (cont'd)

Target	$T_\star$ (K)	Chemistry	Grain Size (μm)	T_{dust} (K)	R_{out}/R_{in}	τ_{60} (μm 10^{-4})
14325-6428	7000	am-C	0.005-0.26	300	5	0.15
		am-C		150	10	0.15
		am-C		100	10	0.15
14429-4539	6000	am-C	0.005-0.26	1000	10	15
		am-C		300	5	15
		am-C		100	10	1.5
14482-5725	7000	am-C	0.005-0.26	275	3	15
		am-C		100	3	0.15
O-rich spectra						
17074-1845	17100	Sil-Ow	0.005-0.26	320	5	0.15
		Sil-Oc		120	5	4.3
17203-1534	20000	Sil-Oc	0.005-0.26	470	2	0.04
		Sil-Oc		110	4	2.75
17364-1238	7500	Sil-Ow 50%, am-C 50%	0.005-0.26	450	2	0.27
		Sil-Oc		100	2	20
17381-1616	24000	Sil-Ow	0.005-0.26	250	3	0.15
		Sil-Oc		120	3	4
17460-3114	34700	Sil-Ow	0.005-0.26	500	1000	0.02

Table 3.3 (cont'd)

Target	$T_\star$ (K)	Chemistry	Grain Size (μm)	T_{dust} (K)	R_{out}/R_{in}	τ_{60} (μm 10^{-4})
		Sil-Oc		140	2	0.017
18062+2410	24000	Sil-Ow	0.005-0.26	320	2	0.32
		Sil-Oc		160	2	4
18435-0052	3000	Sil-Ow 95%, am-C 5%	0.005-0.26	1300	1000	1400
19157-0247	24000	am-C	0.005-0.26	950	1000	0.32
		am-C 70%, Sil-Oc 30%		330		0.17
20572+4919	12000	70% Sil-DL, 30% am-C	0.005-0.26	1300	1000	4.5
				150	1000	3.75
11201-6545	12000	Sil-Ow	0.005-0.26	300	10	0.13
		Sil-Oc		100	5	20
		am-C		150	100	0.15
12175-5338	8000	Sil-Ow	0.005-0.26	300	1000	0.12
				200	1000	0.6
17119-5926	20000	Sil-Ow	0.005-0.26	300	1000	0.19
				150	1000	0.6
17317-2743	4000	Sil-Ow	0.005-0.26	300	1000	1.50
				150	10	0.20
				150	1000	1.4
		am-C		100	10	16

Table 3.3 (cont'd)

Target	$T_\star$ (K)	Chemistry	Grain Size (μm)	T_{dust} (K)	R_{out}/R_{in}	τ_{60} (μm 10^{-4})
17376-2040	6600	Sil-Ow	0.005-0.26	300	1000	1.3
				150	10	15
				100	10	150
17488-1741	6400	Sil-Ow	0.005-0.26	300	2	0.15
		am-C		150	100	0.7
17576-2653	15000	Sil-Ow	0.005-0.26	300	1000	0.10
		Sil-Ow		150	10	0.09
SAO 243756	8700	Sil-Ow	0.005-0.26	300	980	0.08
		am-C		150	1000	19
SAO 227229	7000	Sil-Ow	0.005-0.26	300	1050	1.50
		Sil-Oc		100	10	0.20
Mixed spectra						
17542-0603	21000	am-C	0.005-0.26	1050	100	1
		Sil-Ow		145	3	1.45
18371-3159	24000	Sil-Ow 85%, am-C 15%	0.005-0.26	350	2	0.05
		Sil-Oc		105	5	2.4
18379-1707	24000	Sil-Ow	0.005-0.26	590	3	0.1
		Sil-Oc		120	2	1.7

Table 3.3 (cont'd)

Target	$T_\star$ (K)	Chemistry	Grain Size (μm)	T_{dust} (K)	R_{out}/R_{in}	τ_{60} (μm 10^{-4})
19306+1407	16000	Sil-Ow 95%, am-C 5%	0.005-0.26	440	10	1.5
		Sil-Oc		120	2.5	30
19336-0400	24000	Sil-Ow 85%, am-C 15%	0.005-0.26	320	2	0.4
		Sil-Oc		105	2	4.3
19590-1249	24000	Sil-Ow 85%, am-C 15%	0.005-0.26	300	2	0.035
		Sil-Oc		100	2	1.5
20462+3416	24000	Sil-Ow 80%, am-C 20%	0.005-0.26	300	1000	0.034
		Sil-Oc		100	1000	1.5
21289+5815	15000	Sil-Ow	0.005-0.26	1300	100	4.8
		Sil-Oc		150	100	4.6
22023+5249	20000	90% Sil-Ow, 10% am-C	0.005-0.26	440	3	0.25
		Sil-Oc		105	2	6
22495+5134	20000	30% Sil-Ow, 70% am-C	0.005-0.26	360	5	0.05
		Sil-Oc		115	100	7
11353-6037	11500	80% Sil-Ow, 20% Sil-Oc	0.005-0.26	100	950	95
11387-6113	8700	80% Sil-Ow, 20% Sil-Oc	0.005-0.26	300	900	80
		100% am-C		150	100	0.2
15482-5741	6300	80% Sil-Ow, 20% Sil-Oc	0.005-0.26	100	1000	100
		100% am-C		150	7	0.2

Table 3.3 (cont'd)

Target	$T_\star$ (K)	Chemistry	Grain Size (μm)	T_{dust} (K)	R_{out}/R_{in}	τ_{60} (μm 10^{-4})
SAO 243233	12800	100% Sil-Ow	0.005-0.26	300	1000	0.1
		100% Sil-Oc		100	10	0.2

The limitations of the 1-D DUSTY models produce several unphysical artifacts; to find a good fit to the SEDs, most of the O-rich sources required the addition of amorphous carbon, despite the fact that we do not believe it to be present in the stars. In addition, the models required very large dust grains (up to 100 μm in size); while it is not totally implausible that these sources have large dust grains (our spectra do indicate a high degree of grain processing), 100 μm dust grains would indeed be extraordinary, particularly for sources with such hard (and thus destructive) radiation fields. Though dust grains can coagulate in an outflow, without some type of density enhancement (even an outflowing torus), the duration of time in which dust particles would remain in a sufficiently dense environment that collisions would be frequent is very short. The simplest explanation for the presence of such large dust grains, then, is that the dust remains in a region of enhanced density. It is possible that these dust grains are forming in the midplane of a waist or disk where they are shielded from radiation, but if that were the case they would likely be too cold to detect in the mid-infrared. In any case, our data does not constrain grain sizes very well; sub-millimeter observations would be ideal for that.

3.3 Conclusions

We have imaged a sample of post-AGB with Spitzer to characterize the circumstellar dust that is implied by the SEDs of these sources. We succeeded in resolving for the first time an elongated structure in the circumstellar material around IRAS 11353-6037, which we have classified as having mixed chemistry. We also resolved nebulosity around IRAS 19590-1249, and though it is not perfectly symmetric we do not see any evidence for a dusty waist or disk. We were able to detect extended emission around several other sources as well, but our data indicates that all of the rest were mis-identified as post-AGBs. With so few detections of nebulae, it is not possible to characterize the morphology of these sources with imaging. To investigate these sources further, we used the radiative transfer code DUSTY

to reproduce the Spectral Energy Distributions of our spectroscopic and photometric data combined with fluxes at other wavelengths from published surveys. All of these models required at least two dust components (hot and cool, ranging from 100-1,300 K), which may represent the fossil remains of previous episodes of mass loss or may be the result spatially distinct regions such as an outflow and a circumstellar (or circumbinary) disk or dusty waist. These models also required large dust grains, which is further evidence for the existence of a dusty waist or disk that retains the dust in a reservoir near the star that produces the warm, dense environment necessary for the formation of larger grains and thermal annealing.

Chapter 4

Interferometric Study of Wolf-Rayet stars

Wolf-Rayet (WR) stars are the chemically evolved progeny of massive ($M_{initial} \gtrsim 20M_{\odot}$) O-type stars characterized by heavy mass loss (Massey 1981). Most WR stars exhibit an infrared excess due to free-free emission or dust. Some dusty WR stars have periodic or episodic variability in the infrared, indicative of dust formation events (Williams et al. 1987b). These stars eject, or are stripped of, their outer envelopes at thousands of kilometers per second, with mass-loss rates of $10^{-5} - 10^{-4} M_{\odot}$ per year. The winds are often so dense that they obscure the stellar surface and can form nebulae around the central star that are $\sim 5 - 20$ pc in extent (Bransford et al. 1999).

The spectra of these stars are similar in appearance to massive O-type stars, but anomalous due to their lack of Hydrogen absorption lines; instead, emission lines are seen from the nuclear products of CNO burning. Roche lobe overflow to a binary companion is in some cases believed to be responsible for stripping away the outer (H-rich) envelope of a massive star to reveal its core fusion products . Thus, interpretation of spectral data hinges on the knowledge of such a companion. However, determination of binarity has proved difficult due to the intrinsic photometric variability and exceptionally high line-broadening

wind velocities in these stars. Thus, long baseline interferometers are uniquely suited to answer this question. The aim of this study was to determine binary status for the Wolf-Rayet stars that were observable with the Palomar Testbed Interferometer.

Bright, broad He, C, N and O emission lines dominate the spectra of WR stars with widths upwards of 3000 km/s. WRs are classified into subtypes, WN (nitrogen rich) and WC (carbon rich), defined by the appearance of optical emission lines from He, C, N and O ions. In WN spectra, He I-II and N III-V lines dominate, while in WC spectra C II-IV, He I-II and O III-IV lines dominate. For excellent reviews of the properties of Wolf- Rayet stars, see van der Hucht (1992) and Crowther (2007).

The spectral energy distribution of WRs exhibit a prominent excess in the infrared due to the absorption and re-emission of most of the stellar radiation by the circumstellar envelope. This energy is primarily re-radiated in continuum free-free emission (Hackwell et al. 1974). However, late WC stars also exhibit infrared emission due to thermal dust (Allen et al. 1972). This infrared excess and the bright, compact central sources make these objects ideal for investigations with near-infrared interferometers.

Recent studies of WRs using optical interferometry have successfully resolved some spectroscopic binaries, enabling astronomers to constrain orbital parameters and approximate distance measurements. Using the IOTA Interferometer, researchers were able to spatially resolve WR 140 (Monnier et al. 2004). Using an interferometric technique called aperture masking on the Keck I, structure was resolved in the pinwheel nebula surrounding WR 104 (Monnier et al. 1999), and a similar structure was mapped around WR 98a (Tuthill et al. 1999). Additionally, near-infrared speckle interferometry has been used to measure the extent of some dust shells around Wolf-Rayet stars (Allen et al. 1981).

In sections 4.2 and 4.3, we discuss our experiment to detect and potentially resolve a new group of WR systems with the Palomar Testbed Interferometer and related archival data from the Keck Interferometer. We discuss the data reduction process in section 4.3, present

our analysis of each system in section 4.4, and section 4.5 we summarize our conclusions based on these first look observations.

4.1 Instrumentation and Facilities

4.1.1 The Palomar Testbed Interferometer

The Palomar Testbed Interferometer (PTI) was a near-IR (J,H, and K bands), long baseline, two-element interferometric array located at the Palomar Observatory in North San Diego County, California. It was built by the Jet Propulsion Laboratory, California Institute of Technology, for NASA to develop interferometric techniques applicable to the Keck Interferometer (KI) (Colavita et al. 1999) and was operated from 1995 to 2008. PTI consisted of three 50 cm siderostats, each feeding light into a 40 cm fixed telescope. Any two telescopes could be combined in pairwise combination at one time. This provided a choice of three baselines of 86 m (NW), 87 m (SW), and 110 m (NS), that could resolve targets optimally in the 1 to 5 *mas* angular size range.

Before combination, beams from the two apertures were tilt corrected and pathlength matched. Interference occurred in the pupil plane at a beamsplitter, where the two combined outputs were focused onto an IR detector. Both outputs were band-limited by the astronomical filter K (2.0 to 2.4 μm) in the observations presented herein. One of the outputs was focused onto a single pixel (white light channel), and the other was dispersed via prism into five spectral channels with average channel widths of 97 nm. Before dispersion, the combiner output intended for the spectral channels was spatially filtered by a single-mode IR fiber. There was no spatial filtering of the white light channel other than what occurs naturally due to the finite pixel size (40 μm) and F/10 relay optics. The white light and spectral channels were positioned along a common row of pixels of a NICMOS-3 array.

The optical paths between the two telescopes were matched using a set of delay lines for each beam. Long delay lines tracked the sidereal motion of the target, while fast delay lines

were used to compensate for the higher frequency pathlength changes due to atmospheric fluctuations. For more detailed information on PTI and standard fringe tracking with the interferometer, see Colavita et al. (1999).

4.1.2 Keck Interferometer

The two 10 m Keck telescopes are combined to form the Keck Interferometer (KI), separated by 85 m, oriented along a line 38° east of north (Colavita & Wizinowich 2003). Each telescope is equipped with its own adaptive optics system (Wizinowich et al. 2003), and both are active for all interferometric observations. For each telescope, the beam is routed through the telescope Coudé train to the beam combination laboratory located beneath the telescope observation platforms. As in the case for PTI, the optical paths between the two telescopes are matched using a set of long and fast delay lines for each beam. In the case of the KI when these data were acquired, the long delay lines are fixed during an observation, and the fast delay lines are used not only to track the target over a small range of hour angles, but to compensate for the atmosphere as well (Vasisht et al. 2003).

Angle tracking to stabilize the telescope images is done at J band (1.2 μm), while science and fringe tracking measurements are accomplished in H and K bands. As was the case for the PTI, interference between the two beams occurs in the pupil plane using a beamsplitter. For the KI however, both beamsplitter outputs are spatially filtered using a single mode fiber. One of them is typically dispersed into four spectral channels for the lowest spectral resolution observations, and the other is used as the wide-band white light channel for fringe tracking.

4.2 Data and Reduction

The data were taken at PTI and KI between 16 May 2003 and 16 Oct 2003 in two different, initially unrelated programs. For the PTI data, calibrators were chosen to be

within 10° of the target star and to be unresolved (i.e. much less than 1.0 *mas*) to the interferometer (see Table 4.1) on the typical NS (110m) baseline. The KI data were archival as part of the KI initial shared-risk observing , and so the authors did not choose calibrators for this part of the project. Upon careful analysis for each calibrator prior to reducing the data, some of the calibrators in the KI archive appear to be unsuitable (as explained by suspect binarity, possible confusion with nearby bright source, or variability on short time scales). Hence only a small fraction of the KI data in the archive could be reliably reduced. This was ascertained by examining the predicted system visibilities using only the calibrators together, and from archival research on the potential calibrators using the SIMBAD and Vizier databases. See Table 4.1 for information on the data reduction and predicted angular sizes of the calibrators used for the project.

For the PTI data, a non-standard 50 ms integration frame rate was implemented due to the known inherent faintness of the targets. These data could only be taken on some of the very best observing nights at the interferometer, and therefore complete UV coverage was not the primary goal of the experiment. The interferometric signal from a binary pair will display quasi-sinusoidal variation as a function of Hour Angle, so the minimal coverage gained as the Earth rotates the projected baseline in the span of a few nights is sufficient to distinguish an unresolved point source from a binary or some more complicated structure. These data are not contained in the NexScI archive due to the non-standard observing mode. In order to make this data accessible for future observers, we have included the complete, reduced wideband data in Table 4.2.

These data were reduced in the standard fashion (c.f. Boden et al. 1999), using incoherent averaging for both the wide-band and narrow-band data, with standard jitter and ratio corrections applied. For the KI data, reduced with the same tools available at the NExScI software tools repository, a flux calibration technique implemented in 2007 was employed (c.f. flux bias memo) for data reduction, and this was found to markedly improve the calibration of the KI data. These data were reduced using incoherent averaging, no ratio

correction and a standard jitter correction of 0.04, along with the flux bias correction. All data for which the system visibilities dropped below 50% or for which the system jitter rose above 2.0 radians were deemed unreliable and discarded for both instruments.

PTI calibrators were initially vetted using the NExScI tool getCal and then performing further archival/literature research to eliminate suspected binaries and variable stars or stars expected to have significant emission lines in the infrared. Calibrator angular sizes were estimated, as part of the selection process, using the NExScI tool Fbol. The Fbol tool obtains archival data from the SIMBAD and Vizier databases, including photometry and, where possible parallax. A model spectrum derived from black body curves is matched to the spectral type and luminosity class of the calibrator and then fit to the archival photometry, corrected for reddening based on B-V colors, and scaled for absolute flux levels to arrive at an estimated angular diameter for the calibrator. Uncertainties on diameters were associated with a reduced chi-squared fit of the model to the archival photometry, and were generally set to be no less than 0.1 *mas*. If a fit suggested the spectral type had been misclassified by more than one Spectral Type or the archival photometry strongly suggested variability or infrared excesses, then a calibrator was deemed unsuitable (which was the case for some calibrators used for the KI archival data).

Table 4.1. Wolf-Rayet Observation Summary

Target	SpType	K_{mag}	Nights	Visibility Points	Baselines	Cal1	Est Angular Size (*mas*)	SpType	Cal2	Est Angular Size (*mas*)	SpType
WR 121	WC9	5.773 ± 0.023	2	20	PTI NS, NW	HD 161868	0.79 ± 0.12	A0V	HD 170137	0.74 ± 0.15	K3III
WR 134*	WN6	6.16	1	20	K1-K2	HD 333388[a]	0.65 ± 0.16	K8V	HD 191512	0.74 ± 0.22	K5V
WR 135*	WC...	6.663 ± 0.020	1	0	K1-K2	HD 333388[a]	0.65 ± 0.16	K8V	HD 191512	0.74 ± 0.22	K5V
WR 136	WN6(h)-s	5.561 ± 0.016	3	33	PTI NS, NW	HD 192640	0.46 ± 0.10	A2V	HD 192985	0.40 ± 0.10	F5V
WR 136*	WN6(h)-s	5.561 ± 0.016	1	17	K1-K2	HD 191720[b]	0.06 ± 0.12	B9V	HD 199099	0.10 ± 0.01	A1V
WR 137	WC7 + O9	6.185 ± 0.016	2	12	PIT NS, NW	HD 192640	0.46 ± 0.10	A2V	HD 192985	0.40 ± 0.10	F5V
WR 137*	WC7 + O9	6.185 ± 0.016	1	23	K1-K2	HD 333388[a]	0.65 ± 0.16	K8V	HD 191512	0.74 ± 0.22	K5V
WR 139	WN5 + O6 V-III	6.520 ± 0.038	1	2	PTI NW	HD 192640	0.46 ± 0.10	A2V	HD 192985	0.40 ± 0.10	F5V
WR 140	WC7 + O4 V	5.04	2	15	PTI NS, NW	HD 192640	0.46 ± 0.10	A2V	HD 192985	0.40 ± 0.10	F5V
WR 140*	WC7 + O4 V	5.04	3	136	K1-K2	HD 186427[c]	0.53 ± 0.06	G3V	HD 185657	0.76 ± 0.28	G6V
WR 148	WNv+...	8.318 ± 0.031	1	83	K1-K2	HD 192849	0.07 ± 0.01	A5V	HD 191373	0.13 ± 0.01	F3V

[a]Discarded: shows variation flagged by data reduction tools. Probable binarity.

[b]Discarded: shows variation flagged by data reduction tools. Perhaps a Be star or has a dusty disk.

[c]Discarded: possible confusion upon acquisition with companion (16 Cyg B), a known binary.

*Reduced using only one calibrator.

Table 4.2. Wolf-Rayet Observation Results

Target	Binarity	Resolved	Wideband Evolution	Narrowband Evolution
WR 121	unknown	y	n	n
WR 134*	unknown	n	n/a[a]	n/a[a]
WR 135*	unknown	n/a[b]	n/a[a]	n/a[a]
WR 136	unknown	n	n/a[a]	n/a[a]
WR 137	long-period binary	y	y	y
WR 139	binary	n	n/a[a]	n/a[a]
WR 140	long-period colliding wind binary	y	y	y
WR 148	spectroscopic binary, companion type unknown	y	y	n/a[c]

[a]Data are too sparse to track temporal evolution.

[b]No fringes were acquired on this source.

[c]Data are only resolved at some hour angles, so it is difficult to track temporal evolution for this source.

*Reduced using only one calibrator.

Table 4.3. Wideband Visibility Data

Target	Wideband (2.17 μm) Calibrated V^2	Date (UT) m/d/y/h:m:s	U m	V m	Baseline
WR 121	0.46906 ± 0.02699	5/21/2003/09:20:49	-83.104207	-22.45284	PTI NW
WR 121	0.47775 ± 0.02120	5/21/2003/10:28:16	-82.329409	-20.823947	PTI NW
WR 121	0.48337 ± 0.03190	5/21/2003/10:30:39	-82.170421	-20.767433	PTI NW
WR 121	0.46827 ± 0.01604	5/28/2003/09:25:22	-83.643025	-21.676408	PTI NW
WR 121	0.49154 ± 0.01733	5/28/2003/10:10:15	-81.639651	-20.597843	PTI NW
WR 134	1.04507 ± 0.17473	7/9/2003/10:39:23	-64.235902	-49.293042	PTI NW
WR 134	0.99925 ± 0.05000	8/9/2003/11:32:41	31.088729	79.096597	Keck
WR 136	1.00900 ± 0.06834	6/3/2003/10:09:33	-52.158109	-95.334441	PTI NS
WR 136	0.97805 ± 0.04101	6/3/2003/11:29:34	-32.894353	-104.669336	PTI NS
WR 136	0.95156 ± 0.06348	6/5/2003/09:45:22	-82.918544	-10.20814	PTI NW
WR 136	0.91667 ± 0.08104	6/5/2003/11:01:12	-82.034787	-27.347984	PTI NW
WR 136	0.94372 ± 0.05540	6/5/2003/11:55:09	-75.913296	-38.971192	PTI NW
WR 136	1.05531 ± 0.17524	7/9/2003/10:13:28	-70.264921	-45.329474	PTI NW
WR 136	1.34308 ± 0.20904	7/9/2003/11:14:11	-55.872892	-55.791259	PTI NW
WR 136	1.24569 ± 0.45175	7/9/2003/11:19:13	-54.490881	-56.543951	PTI NW
WR 137	0.85452 ± 0.09626	6/3/2003/10:17:17	-51.050957	-96.471125	PTI NS
WR 137	0.26138 ± 0.02375	6/3/2003/11:46:37	-28.862123	-105.916404	PTI NS
WR 137	0.32210 ± 0.00781	6/3/2003/11:49:00	-28.190114	-106.094961	PTI NS
WR 137	0.85402 ± 0.16326	7/9/2003/10:27:34	-67.852018	-46.766938	PTI NW
WR 137	0.53514 ± 0.05000	8/8/2003/10:40:27	42.429778	73.214755	Keck
WR 137	0.64115 ± 0.05000	8/8/2003/10:42:18	42.126426	73.418796	Keck
WR 139	1.44459 ± 0.30259	7/9/2003/10:57:06	-62.213288	-52.058885	PTI NW
WR140	0.83753 ± 0.03204	6/3/2003/10:17:17	-44.161015	-98.660063	PTI NS
WR140	0.29304 ± 0.00733	6/3/2003/11:46:37	-82.079548	-27.003904	PTI NW
WR140	0.32003 ± 0.01810	6/3/2003/11:49:00	-81.897955	-27.622642	PTI NW
WR140	0.63979 ± 0.01847	7/9/2003/10:27:34	-80.218947	-32.234542	PTI NW
WR140	0.29507 ± 0.05826	8/8/2003/11:29:14	34.714751	76.673837	Keck
WR140	0.45047 ± 0.08439	8/8/2003/12:12:12	25.763674	80.624579	Keck
WR140	0.88627 ± 0.04022	10/15/2003/05:20:35	50.49501	63.372301	Keck
WR140	0.86902 ± 0.04024	10/15/2003/05:40:18	48.116401	66.321223	Keck

Table 4.3 (cont'd)

Target	Wideband (2.17 μm) Calibrated V^2	Date (UT) m/d/y/h:m:s	U m	V m	Baseline
WR140	0.95519 ± 0.03463	10/16/2003/05:36:36	48.085093	66.356336	Keck
WR140	0.83750 ± 0.03353	10/16/2003/05:55:10	45.514992	68.99084	Keck
WR140	0.61931 ± 0.03016	10/16/2003/06:11:59	42.925199	71.247497	Keck
WR 148	0.98175 ± 0.10544	10/15/2003/06:07:54	47.214476	63.247849	Keck
WR 148	1.01420 ± 0.04791	10/15/2003/06:09:40	46.972968	63.536669	Keck
WR 148	0.83647 ± 0.14987	10/15/2003/06:24:43	44.799479	65.93923	Keck
WR 148	1.11021 ± 0.07185	10/15/2003/06:26:33	44.521351	66.223861	Keck
WR 148	0.72792 ± 0.09084	10/15/2003/06:40:36	42.295767	68.345009	Keck
WR 148	0.78680 ± 0.04873	10/15/2003/06:42:26	41.995598	68.611694	Keck
WR 148	0.87783 ± 0.07196	10/15/2003/06:56:10	39.646256	70.561204	Keck
WR 148	0.83581 ± 0.12481	10/15/2003/06:57:59	39.324866	70.810351	Keck

Table 4.4. Adopted Binary Parameters

Parameter	WR 137	WR 148
P	4766 ± 66 d[a]	4.3174 d[d]
e	0.178 ± 0.042[a]	0.079 ± 0.030[d]
a	16 AU	$38 R_{\odot}$[d]
i	67°[a]	66.7°
T_0 (JD)	2450198 ± 186[a]	2449639.961 ± 0.219[d]
ω	$326^{\circ} \pm 15^{\circ}$[a]	*unknown*
Ω	137°[b]	*unknown*
d	1.82 kpc[c]	8.28 kpc[e]

[a]Lefèvre et al. 2005, [b]This paper, [c]Nugis & Lamers 2000, [d]Marchenko et al. 2003, [e]van der Hucht 2001

4.3 Analysis of Individual Target Data

In total, eight different WR systems were attempted with PTI and KI during the summer and fall of 2003. In all but one of the systems, it was possible to acquire fringes. The calibrators used for each set of observations along with the summarized results for each source are presented in Tables 4.1 and 4.2. In Table 4.2 the calibrated PTI wideband data are presented along with the observation dates.

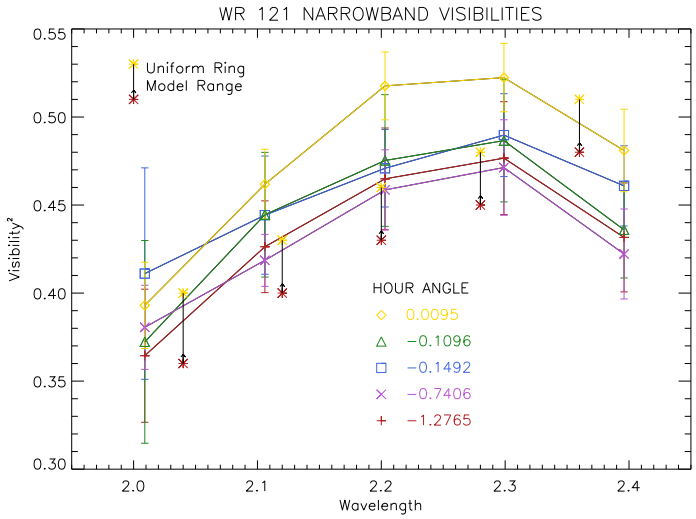

Figure 4.1 The "best fit" model for WR 121 plus the actual PTI narrow-band data. Hour angle (HA) is increasing in the models from -1.33 to 0.0 hours from red to yellow, as indicated by the arrows. This model was produced by a uniformly illuminated ring with major axis of 6.5 mas outer diameter, 1.0 masinner diameter, and minor axis of 2.5 mas outer diameter, 1.0 mas inner diameter aligned with the major axis coincident with the declination axis. We note that the models are relatively insensitive to changes along the declination direction (see the text for details). We stress that none of the models are able to reproduce the inflection seen in the V^2 at 2.4μm, indicating that the actual observations of WR 121 are more complex than anything that can be modeled parametrically or constrained easily with this small amount of HA coverage.

4.3.1 WR 121

Target star WR 121 (HIP 91911) was characterized as a Wolf-Rayet star by Merrill & Burwell (1950) and has since been spectroscopically classified as a WC9 (Roberts 1962).

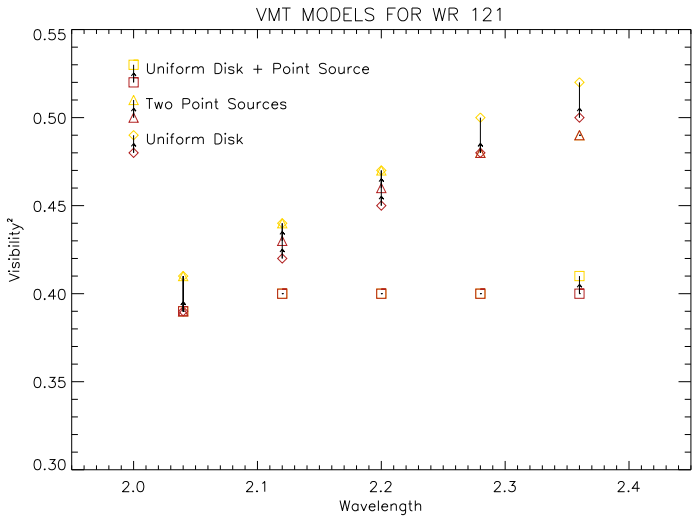

Figure 4.2 Other VMT parametric models attempted to fit the narrow band data for WR 121. Hour angle (HA) is increasing in the models from -1.33 to 0.0 hours from red to yellow, as indicated by the arrows. In most cases, the visibility increases toward positive HA. Error bars (not included) are 0.02 in V^2.

At a distance of 1830 pc (van der Hucht 2001), the star exhibits irregular obscuration events, and its binarity is unknown. Cohen & Kuhi (1977) first suggested that the star was a binary due to the dilution of emission lines, but later spectroscopic studies done by Torres & Conti (1984) found no evidence of a companion star. Veen et al. (1998) suggested that the occasional obscurations are due to intermittent dust production. The currently accepted value for the terminal wind velocity is 1100 km/s (van der Hucht 2001). A study to characterize the variability of this source as perhaps originating in a Corotating Interaction Region was carried out by St-Louis et al. (2009), but they were unable to rule out the possibility that the variability was originating in some type of colliding wind binary interaction. In the near-infrared PTI wavelength regime (2.0-2.4 μm), Figer et al. (1997) found prominent He I and He II emission features at 2.1636 μm, 2.185 μm, and 2.3464 μm and weak CII and CIV emission lines at 2.0824 μm, 2.1131 μm and 2.3243 μm.

We initially disregarded the observations of this target because the source was much brighter and more resolved than expected based on flux counts and raw visibility measured

by PTI. Pitault et al. (1983) published a K band magnitude for this source of $K_{mag} = 6.10$ and Williams et al. (1987a) measured $K_{mag} = 5.97$, possibly indicative of low level variability of the source. The PTI-derived K_{mag} was 2.3 ± 0.05, more than 3.5 magnitudes brighter than expected for WR 121. When we examined the nearby field using surveys like 2MASS, SDSS and POSS, we intially concluded that the target acquisition system might have locked on a bright star 1.5 arcminutes away, NSV 11276. However, NSV 11276 is classified by SIMBAD as an M6 dwarf, and based on the $V_{mag} = 14$ and a calculated distance modulus from Cox (2000), we calculate that this star would have an angular size of less than 0.1 *mas*. Such a star would not have been resolved by PTI and would produce fringes with a V^2 close to 1.0. Adding to the confusion, NSV 11276 has a $K_{mag} = 2.294 \pm 0.256$ from 2MASS (Cutri et al. 2003). If NSV 11276 were actually a giant star rather than a dwarf, with a physical diameter based on van Belle et al. (1999) of $\simeq 230 R_{\odot}$, it would be at a distance of 100-166 pc based on these measurements. Such a star has an absolute visual magnitude of -0.3 (Cox 2000) and thus would have an apparent visual magnitude between 4.7-5.8, much brighter than SIMBAD's listed magnitude for NSV 11276. We further verified the correct pointing of PTI by done examining the logs for the metrology measurements, which acquired the stellar fringes at the predicted pointing position without significant offsets. Therefore, we rule out that we acquired anything other than WR 121.

As presented above, PTI caught WR 121 in an apparent outburst. Because of the unexpectedly higher photon counts, it was possible to get good SNR on the five individual spectral channel data at K band (Figure 4.1). Examination of these data shows a unique feature, that the data rise in V^2 from 2.0-2.3 μm, and then drop again in the 2.4μm channel. This is true for all hour angles, and on both nights, and is significant given the typical V^2 error of 0.02-0.03. Unfortunately, because WR 121 is so far south for PTI, the NW baseline was the only one with which we could observe this target. This baseline, for very far south targets, is not very sensitive along the declination direction, which means true data fitting for so few UV points is mostly meaningless. We did, however, use the Visibility Modeling

Tool (VMT) at NExScI to try to reproduce the unique shape of the V2. We found no satisfactory one or two-component parametric models which can reproduce both the extent of the V^2 and the change in the 2.4μm channel (Figure 4.2). Further, there are no prominent emission lines near 2.4μm (Figer et al. 1997), which might explain this type of change in the spectral V^2 that might be attributed to a resolved emission line.

A few consistencies do appear when attempting to model the data. First, there is resolved emission which is likely more elongated in the dec direction than along RA, whether distributed as a disk, ring or gaussian, having a ratio of approximately 2:1 or higher, with the minor axis (oriented along the RA direction) in the size range of about 2-3 mas. Two component models, whether for an unresolved point source with a ring, disk, or secondary point source, all require flux ratios of 3:1 or higher in the central point source as compared with the outer parametric feature. None of these toy models can reproduce the detailed shape of the V^2 at 2.4μm. We conclude that whatever happened in the outburst of WR 121 had a complex shape, not easily constrained with a single-baseline interferometer.

Veen et al. (1998) constructed a dust condensation model to explain the occasional "obscuration events" observed in visible wavelengths for WR 121. They argue that the optical obscuration is caused by extinction due to a rash of dust formation in the circumstellar environment. The formation of dust clouds in such a hot environment is not understood, but if that is the mechanism behind these events, as the authors suggest, and this event is similar to the near infrared outburst that we have observed, then it might be that the emission region we have resolved is one of these dust clouds. Such clouds would almost certainly have a complex shape, and indeed, we have not been able to reproduce the resolved emission with any geometrically simple models. These condensation events occur interior to the permanent dust shell, which is estimated by Williams et al. (1987a) to have an inner edge at a radius of 180R_{WR}. Based on a Wolf-Rayet radius of 13$R_\odot$ (Howarth & Schmutz 1992), this puts the inner radius of the dust shell at 2340$R_\odot$. Veen et al. (1998) found that the condensation responsible for these transient obscuration events must take place at radii

ranging from 80–800$R_{\odot}$. Assuming the distance of 1830 pc from van der Hucht (2001), the inner radius of the permanent dust shell would have an angular size of 11.9 mas, which is much larger than anything reproduced in the toy models performed here. The angular size of the transient dust condensation event interior to this shell modeled by Veen et al, however, falls right in the "sweet spot" of the interferometer sensitivity in the 1-4 mas range. Thus, it seems that we have serendipitously observed this source during a dust formation episode with an instrument that happened to be capable of resolving features on the size scale of the dust cloud. In an attempt to confirm that the star underwent an "obscuration event" around the time of our observation, we searched the literature and online archive in the hope that someone was monitoring this source, but were unsuccessful. While there is not enough data to constrain these estimates further, these PTI data potentially indicate that WR 121 was captured during some type of dust obscuration or transient event in mid 2003.

4.3.2 WR 136

Target star WR 136 (HD 192163) has a much studied ring nebula around it, called NGC 6888. However, the nebula's large angular size (18' x 12', Chu et al. 1983) places it well outside of our near-infrared interferometer's field of view (Moore et al. 2000). For its spectral type, WR 136 contains an anomalous abundance of Hydrogen, $\simeq$10% by mass (Crowther & Smith 1996). Spectroscopically, this star is apparently single, though there is significant, periodic spectral variability on the order of 4.5 days (Antokhin & Cherepashchuk 1985). The distance to WR 136 of 1260 pc is well known because of its proposed membership in the Cygnus OB1 association, based on cluster fitting to the B main sequence stars (Garmany & Stencel 1992). The terminal velocity, based on Ca IV emission line width at 3.207 μm, is 1490 km/s (Ignace et al. 2001). Emission features in the near infrared are dominated by He II at 2.188 μm and 2.343 μm, and He II blended with He I and H I at 2.165 μm (Libonate et al. 1995). Mid-infrared observations by Smith & Houck (2001) show a broad flat absorption feature near 10μm, indicative of warm ($\simeq$1000K), possibly

optically thick dust, with a continuum-like stellar spectrum short of 9.6μm. This observational result is consistent with models of Zubko (1998), where physical models of dust and gas fitted to optical, NIR and IRAS data predict the inner dust shell radius for WR 136 at 700R$_*$ and the dust component spectrum peaking near 3μm.

Both the KI baseline and two PTI baselines (the NS 110 m and the NW 86 m) were unable to resolve any binarity in the WR 136 system in the wideband K observations. This allows us to put an upper limit on the size of a single star of 1.0 *mas*, or assuming the distance of 1260 pc, 0.79 AU, which is a radius of less than 85 $D_\odot$. A binary with a flux ratio of up to 0.8:1 would be resolved by these interferometers on these baselines at angular separations of larger than about 0.5 *mas* at the declination of WR 136, and so we can rule out a nearly equal brightness binaries with projected separations of about 0.4 AU or larger as well. At 1260 pc, a 13R$_\odot$ WR star with a 700R$_*$ dust radius would be resolved at approximately 67 mas diameter. This is far outside the range of PTI's sensitivity, but could contribute a modicum of incoherent flux, which would serve to lower the measured V^2. Again, because WR 136 was effectively unresolved to PTI, we do not believe we have even marginally resolved the inner radius of the presumed warm dust shell detected by Smith & Houck (2001). An imaging interferometer with a shorter baseline, or thermal infrared sensitivity, may be able to resolve such features in this system.

4.3.3 WR 137

Target star WR 137 (HD 192641) is a long period binary, consisting of a WC7 ($M_{WR} = 4.4 \pm 1.5 M_\odot$) and an O9 star ($M_O = 20 \pm 2 M_\odot$;Lefèvre et al. 2005; Gies 2003). The system has a period of 13.05 ± 0.18 years and observed aperiodic dust formation episodes with the last recorded dust formation maximum occurring in 1997 (Marchenko et al. 1999). These maxima are thought to be associated with the periastron passage of the O-star and the Wolf-Rayet, perhaps caused by colliding stellar winds (Lefèvre et al. 2005). A shorter periodicity has also been observed at 0.83 days by Lefèvre et al. (2005) and colleagues. Polarization

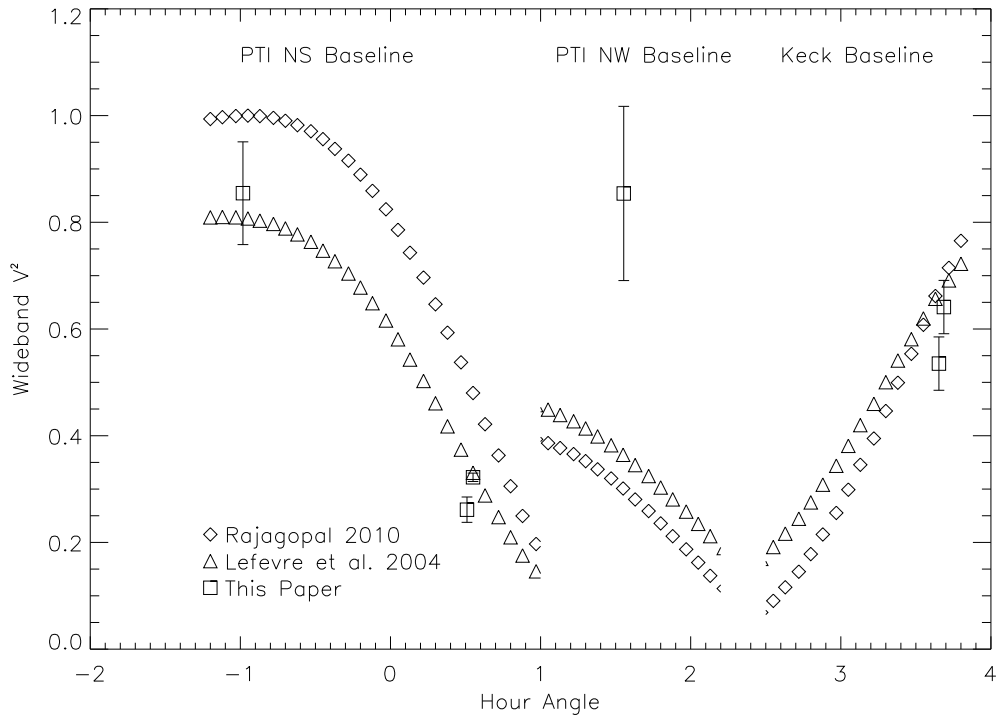

Figure 4.3 Binary orbit model fits to the wideband interferometer data for WR 137. Both binary models adopted the values of Lefèvre et al. 2005; the missing angular parameter (Ω , longitude of the Ascending Node) was varied to find the best fit to the Position Angle and separation derived from interferometric measurements at a particular phase in two cases. The resulting models are shown for Rajagopal 2010, yielding $\Omega = 112°$, and the value that best agrees with our data, $\Omega = 137°$. Both agree with the separations predicted by Lefèvre et al. 2005 to within their published error bars. The data point from PTI's NW baseline was taken in poor weather conditions, so we do not consider it to be very reliable.

measurements in visible and near-infrared wavelengths have confirmed an aspherical symmetry in the winds (Harries et al. 2000). The terminal velocity of the wind, derived from P Cygni profiles, is 1885 km/s (Prinja et al. 1990). The most prominent emission features in the K band are blended C IV at 2.0754 μm and a C III line at 2.1118 μm. Other minor emission features include C III, He I and He II (Figer et al. 1997). Williams et al. (1987a) predict the existence of a persistent dust shell at $R_{in} = 6130 R_{WR}$ and $R_{out} \approx 2R_{in}$, which

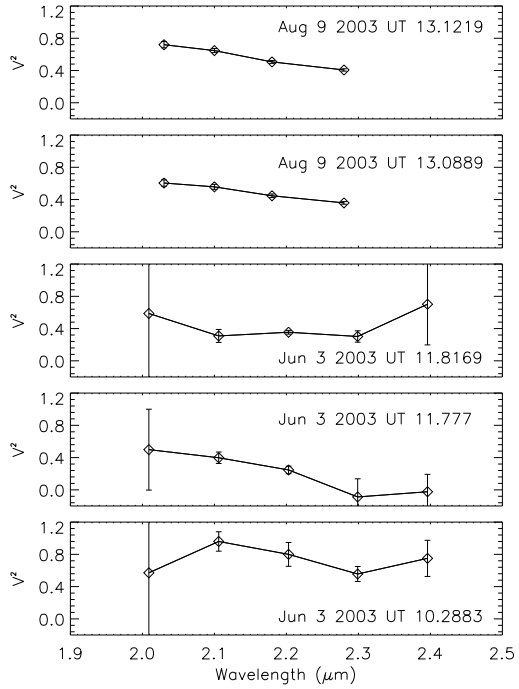

Figure 4.4 Narrowband Visibilities for WR 137 and their evolution over time. We see little clear evidence for the strong emission lines between 2.0 and 2.2 microns seen in WR 137 by Figer and McLean. The data, however, are particularly noisy in the shortest and longest channels owing to atmospheric noise (mostly from water vapor) and the inherent faintness of the source. We also note the PTI data from June 2003 are much noisier than the KI data from August of that year.

would correspond at 1.82 kpc (with $R_{WR} = 4R_{\odot}$) to an angular size of ≈126 *mas*, outside the interferometer's field of view but possibly capable of contributing to an incoherent flux.

WR 137 was observed on two separate nights at PTI using both the NW and NS baselines. Further, there are two data points in the KI archive, which unfortunately only have one reliable calibrator available for the data reduction. We have resolved the pair in the wideband observations and also recorded evolution in the visibility over time (Figure 4.3).

A spectroscopic orbit for this known binary was published by Lefèvre et al. (2005), the details of which are in Table 4.2. This is essentially a 2-D orbit, where only $M \sin^3 i$ is uniquely determined for each star; they adopted published stellar masses to derive the inclination of 67°. A seventh orbital element is required to uniquely determine a 3-D orbit, namely, the longitude of the ascending node, or Ω.

Our interferometric measurements are sensitive to three parameters: the separation, brightness ratio, and position angle (PA) between the two stars. As such, we are not capable of producing a full orbital solution. However, if we adopt the published binary parameters, we are able to use our data to constrain the final orbital element, Ω, that specifies the position angle between the two stars when they align in the plane of the sky. This parameter can only be obtained from spatially resolved observations, since it essentially specifies the orientation of the system as it is projected on the plane of the sky. We can only deduce the position angle if we assume a certain brightness ratio between the two stars. There is a great deal of degeneracy between these two parameters, and without more data the best we can do is rule out a region in binary parameter space. Rajagopal (2010) observed this system with the Center for High Angular Resolution Astronomy (CHARA) interferometer, where they obtained closure phase measurements which break this degeneracy. They published a snapshot of the system including the brightness ratio, PA and angular separation between the two stars at the time of their observation.

Adopting their value for the brightness ratio allows us to determine (within the errors of the adopted parameters) the PA between the two stars at the time of measurement by using the VMT to reproduce the PTI and KI wideband data. We started with the predicted separation based on Lefèvre et al. (2005) and then explored the local parameter space (PA, separation and flux ratios) to find the values of those parameters that most closely matched our observations. It is important to note that this is not a robust fitting procedure; there are many possible solutions that will reproduce our data. We have merely found those solutions

that comprise a local minima in the restricted parameter space defined by our assumptions based on previous studies of this source.

We produce a solution consistent with a separation of 9.32 *mas*, a PA of 303.7° and fluxes of 60% for the primary, 30% for the secondary and 10% incoherent flux which we attribute to the unresolvable dust shell. The incoherent flux is consistent with leftover hot dust from potential dust production events in the recent past. Nevertheless, we find it is impossible to match the singular PTI NW data point, though we note that the system visibility (58%) that night was very close to our cutoff for discarding the data. This result is not conclusive, as there is too little interferometric data to constrain well a complicated system which includes potential dust formation events. However, it may be possible with interferometric imaging to fully resolve what appears to be a dust enshrouded binary system.

If we adopt the values found above for the separation and PA of the system at the time of observation and use the phase given by the spectroscopic orbital solution, we can calculate the last orbital parameter, Ω. We have performed such a calculation and performed fits to our data, based on the orbit of Lefèvre et al. (2005) and the brightness ratio found by Rajagopal (2010). We find a PA (measured from the brighter star to the fainter) of 303.7° at the time of the PTI measurements, which corresponds to $\Omega = 137°$.

For comparison, we did the same calculation for the interferometric observations published by Rajagopal (2010), again assuming the parameters of Lefèvre et al. (2005), which leads to $\Omega = 112°$. The two orbital solutions are plotted with our data points in Figure 4.3; Table 4.2 contains the full list of binary fit parameters adopted.

4.3.4 WR 140

Target star WR 140 (HD 193793) is a prototypical colliding-wind binary, with a spectral type WC7 + O4-5 and an orbital period of 2899 ± 1.3 days (Marchenko et al. 2003). Previous periastron passages of this binary have been marked by dust formation episodes

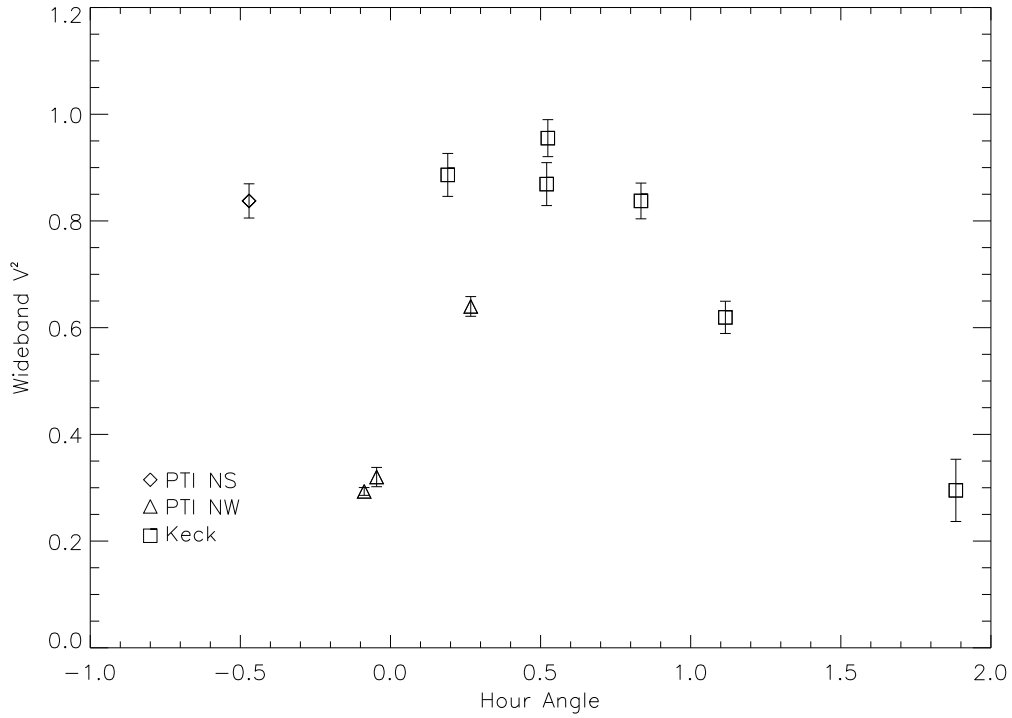

Figure 4.5 Wideband Visibilities for WR 140. We expect these values to vary in time as well as with respect to HA, but lack the necessary coverage for a fit.

lasting several months, the last episode occurring in 2001. Near-infrared observations taken with aperture-masked Keck I in 2001 resolved a complicated partial ring-shaped distribution attributed to a transient dust shell that formed after periastron passage (Monnier et al. 2002). Radio observations from the VLBA have similarly resolved a bow-shaped emission region in the wind collision zone between the two components (Dougherty et al. 2005). The only prominent spectral emission feature of WR 140 in the K-band is a broad, blended C IV and C III lines at 2.0746 μm and 2.1067 μm with a He I line on the long-wavelength shoulder of the blended C line at 2.12 μm, respectively (Figer et al. 1997).

This well-known dusty binary was observed on both the NW and NS baselines at PTI, and can also be found in the archives of the Keck Interferometer. In both data sets, the star is resolved and evolving in the wideband, with resolved, evolving spectral features

in the narrowband (see Figures 4.6 and 4.5). The interferometric visibility in the second spectral channel, centered at 2.12 μm, appears to be less resolved than in the two adjacent channels. This is suggestive of the spatial distribution of these lines being closer to the photometric center of the WR 140 system as compared with the stellar continuum and/or hot dust emission in this system. Many recent studies of spatial-spectral line distributions using interferometry have been able to demonstrate detailed distributions and physics for YSOs in particular (c.f. Eisner et al. 2010), and it would be reasonable to expect that a spectrally resolved imaging interferometer could contribute more information towards understanding a complex dusty system such as WR 140.

4.3.5 WR 148

Wolf-Rayet star WR 148 (HD 197406) is a single-line spectroscopic binary with an orbital period of 4.3 days (Smith et al. 1996; Bracher 1979). It is unusually far from the Galactic plane for a WR star, which along with its peculiar velocity relative to Galactic plane orbits led Drissen et al. (1986) to classify it as a runaway star possibly ejected from the Galactic plane by a supernova explosion. The companion is believed to be compact (either a neutron star or black hole), perhaps enclosed in the WR envelope (Moffat & Isserstedt 1980). Flare events, x-ray emission, long-term variation on the order of years, and random short-term variability have all been observed (Panov et al. 2000).

This star was observed with the Keck Interferometer (Figure 4.7). The wideband data appears to be marginally resolved over a small range of hour angles (0.63 to 1.47) over one night of data comprising a total of 83 visibility measurements. This is consistent with one of two interpretations, the first being that the source containts a slightly resolved uniform disk of 1.15 *mas*. However, the trend in the data toward lower visibilities at the largest hour angles suggests a second possible interpretation: that WR 148 is an equal brightness binary of unresolved point sources separated on the order of 0.8*mas*, preferentially in the direction of declination. Based on the binary parameters in Table 4.2, at the distance of 8.28 kpc (van

der Hucht 2001), the binary would not be resolved. Even at the 4.5 kpc kinematic distance derived by Dubner et al. (1990), which we consider to be a lower limit on the distance, the average separation would be 0.04 *mas*, well below the interferometer's resolution. So either the WR 148 system is much less distant than previously published, or some type of resolved dusty distribution is present in this system.

4.3.6 WR 134, WR 135 and WR 139

Due to the stringent seeing requirements needed to observe these sources at PTI, the resultant data were too sparse to be conclusive in these three cases. WR 134, an apparent single star, was fringe tracked with PTI and found to be unresolved, although only 3 visibility points with a great deal of scatter were acquired. It was also unresolved in the archival KI data, as reported by Rajagopal (2010); and we found this as well even after one bad calibrator was thrown out and we re-reduced the data. If there is no variation of the V^2 with time, this measurement may serve to place an upper limit on the uniform disk angular size of 1.0 *mas*, which at the distance of 1.74 kpc (van der Hucht 2001), corresponds to a physical diameter of 0.58 AU or $62 D_{\odot}$. This might be consistent with resolving a dust shell, though the data are too sparse to make a definitive conclusion. None of the KI data on WR 135 could be calibrated and it was too faint to attempt with PTI. The most likely reason for any failure to acquire fringes is an excessively faint and/or over-resolved source. WR 139 was observed on one night with PTI, however only two visibility points were acquired in marginal seeing (as traced by the high jitter and low system visibilities). As such we choose not to evaluate this target, except to indicate that it appears possible to fringe track it with a near-infrared interferometer.

4.4 Conclusions

We performed observations with PTI, to attempt to resolve the binarity and spectral features of a handful of Wolf-Rayet systems. This experiment was not intended to derive orbits as exceptional seeing conditions were necessary to operate on targets at this K-band magnitude (as faint as $K_{mag} = 6.3$). After the data were acquired it was learned that a similar program at nearly the same time of year had been undertaken at the KI during initial shared-risk observing in the summer and fall of 2003. With PTI we were able to fringe track on 4 of the 6 targets. Of these, only WR 121 cannot be confirmed to be a binary or have a resolved (presumed dusty) distribution in the system. WR 134 and 139 were both able to be fringe tracked with PTI, however the data were considered too sparse to warrant even rudimentary evaluation. Nevertheless, it is possible to acquire fringes on both these sources. KI archival data was available on most of these targets as well, and in a few cases we reduced and added the data to those reported here from PTI to be able to better describe and constrain the systems. WR 135 and 148 were attempted exclusively with the KI by another team during shared risk observations in 2003. For WR 148 the data are consistent with a marginally resolved system, likely a dusty circumbinary distribution as the single-lined binary is in a very short period orbit. It is clear, especially for imaging interferometers, that Wolf-Rayet systems are excellent targets as they present complex and evolving visibilities with resolved spectral features due to emission lines and dust. Given the stringent NIR magnitude requirements for modern interferometers, about a dozen are accessible for imaging (i.e., much better UV plane coverage) with VLTI and CHARA. Observations with these instruments, which offer better spatial resolution, sensitivity and coverage of the UV plane, have the potential to significantly increase our understanding of the dust formation and shaping induced by binary interactions, as well as the structure in and evolution of the winds of single Wolf-Rayet stars. Long-term monitoring of these stars with an interferometer could improve our understanding of these dust formation events and why

they occur, and could help us quantify the physics of the wind interactions in binary systems that shape the circumstellar dust. Next generation instruments, such as the Magdalena Ridge Observatory Interferometer, will dramatically increase the pool of observable Wolf-Rayet systems, allowing for statistical characterizations of these fascinating stars.

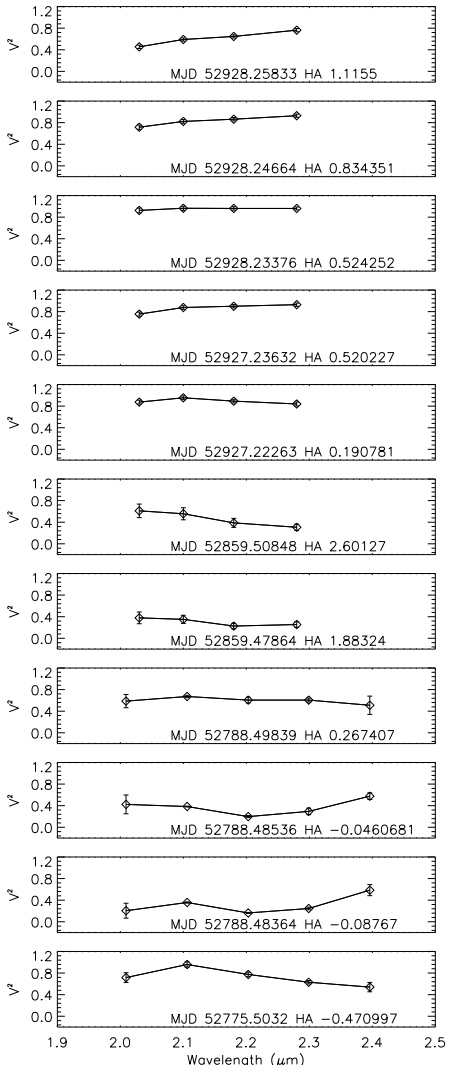

Figure 4.6 Narrowband Visibilities for WR 140 and their evolution over time. The 2.1 μm channel contains a blended C IV, C III and He I emission feature, which appears to be less resolved, and therefore closer to the photometric center of the star than the hot dust component, represented by the other continuum-dominated channels.

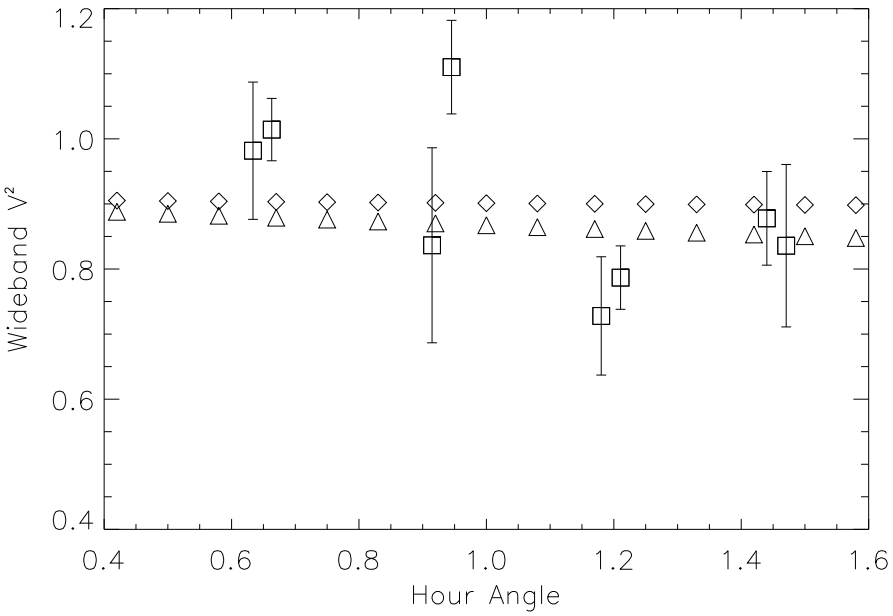

Figure 4.7 Wideband visibilities for WR 148. Shown are the models for a 1.15 *mas* uniform disk (diamonds) and an equal brightness binary separated by 0.8 *mas* in the direction of declination (triangles). With the limited UV coverage available, we find a slight preference for the second interpretation. This likely requires a re-evaluation of the distance for the system.

Chapter 5

Conclusion

In each of Chapters 2-4, we have addressed one aspect of the process that returns stars to the dust from which they were born. We have discovered that a majority of late-stage post-AGBs appear to harbor a reservoir of dust near the star, likely in the form of a dusty waist or disk, where the dust grains coagulate and are processed by radiation from the central star. These objects also seem to have at least two distinct dust components which are either spatially segregated from one another (such as in an outflow and a disk) or that are merely distinguished by their exposure to radiation from the central source (e.g., if a dusty waist shields radiation from part of the outflow). Models of various formation scenarios for potential dust reservoirs favor the presence of a binary companion to provide gravitational focussing in the outflows or direct formation of a circumstellar disk via Roche Lobe Overflow. Though few binary companions have been observationally detected in post-AGBs, De Marco (2009) have suggested that all PNe are the result of such interactions. This is a hotly debated question that remains unanswered. Our data do not detect binarity directly, but do seem to favor this formation scenario for our sources.

The more massive Wolf-Rayet stars pose an equally vexing question: are they all the result of binary interactions via Roche Lobe Overflow, or is there a single-star process that can strip away the outer layers of the star with equal efficiency? To test this hypothesis, we

took interferometric observations of the few WR systems that are close enough to barely meet the minimum flux requirements for such observations. Though the data were plagued by small statistics and large error bars, owing to the fact that they could only be observed in the absolute best seeing conditions, we were able to conclude that some stars are indeed binary as well as put upper limits on the separation of any binary companion for others.

All of these studies address the broader question of the role that binarity plays in stellar evolution. We have discovered that companions, even planet-scale ones, can profoundly effect the evolutionary path of a star and ultimately the manner of its demise. In addition, binary companions may provide the physical conditions that make the circumstellar envelopes of evolved stars rich environments for the formation of a menagerie of complex molecules, including those that are the basis of life on our planet and potentially others.

5.1 Future Work

5.1.1 Principal Component Analysis: A search for correlations between spectral features, evolutionary status

Several properties of Young PNe (YPN) have been proposed as tracers of the evolution along the track from post-AGB to PN. The diversity of YPNs, particularly in mass, dust chemistry, and binarity (still unknown for almost all of the objects in this sample) has stymied past attempts to find a solid indicator of evolutionary status among these objects. Thus, as a next step, one could pursue use a Principal Component Analysis (PCA) to tease out any correlations between the many candidate age indicators. Ideally analysis would synthesize the results from a spectral fitting procedure, described below. In this way one may be able to find an observational parameter (or linear combination of a few parameters) that provide a good diagnostic of the evolutionary status of these objects. If this analysis is successful, the resulting observational tool would contribute immensely to our understanding of how the C-rich, O-rich, and Mixed chemistry post-AGB stars evolve.

Each of the columns one could potentially use in a PCA are described below:

1. **Transition from Aliphatic to Aromatic:** As discussed above, for the carbon-rich sources, Zhang et al. 2010 suggest that the structure of the carbon dust may transform over time, from aliphatic to aromatic compounds. As a measure of this, one could use the ratio of feature strengths at 21, 30, and 10 μ m:
$\frac{[21]\mu m + [30]\mu m}{[10]\mu m}$
which is the ratio of features attributed to aliphatic compounds to those attributed to aromatic compounds. This parameter should increase with time if there is a correlation.

2. **Ionization Fraction:** The most direct method we have to measure the evolutionary status of an object is the ionization fraction. As the central star heats up, the ionization front travels outward through the circumstellar material, and thus in the simplest case of uniformly distributed material, the ionization fraction should increase linearly from the start of ionization to the edge of the envelope. Though this would be easy to track if we could watch a single object evolve over time, using this measure to place diverse sources on the same timeline is much more difficult. These sources vary in the extent of circumstellar material they harbor, the density and opacity of that material (and thus the radial velocity of the ionization front), and of course the mass of the central stellar remnant (which affects the rate at which the heating progresses, again affecting the speed of the ionization front). There are two measures of the ionization fraction that one can test for correlation: the AIB and H_2 ionization fractions. These ratios are a measure of the degree of ionization in the carbon dust and H_2 molecules, respectively.

3. **Grain Growth:** Another observational quantity that evolves over time in these sources is the size of the dust grains, as we have previously mentioned. The AIBs detected in the IRS wavelengths of our Carbon-rich sources are attributed to specific grain sizes,

as discussed in Ch. 2. Thus, one could test this parameter as a potential measure of evolutionary state.

4. Amorphous SiC: The 11.3 μm feature detected in many of our Carbon-rich sources has been attributed to amorphous SiC, and is thought to change from emission to absorption in the post-AGB to PN phase. Thus, one can test this as a potential diagnostic of evoluti

5. Central Star Temperature: As discussed in Ch. 2, we have derived central star temperatures from published Spectral Types for our sources. Though the uncertainties in these values are large, one could nontheless use it as a potential age indicator for these sources.

6. Amorphous Silicates: The features detected in our Oxygen rich sources at 9.9, 10, and 19 μm have been attributed to amorphous silicates, and both the strength of these features and their central wavelengths are proposed to evolve over time. Thus, one can use these measures in a test for correlations as well.

7. Crystalline silicates: The infrared emission detected in many of our Oxgen-rich sources at 11.3, 16.2, 19,7, 23.7, 28, and 33.6 μm are due to crystalline silicates. These grains are thought to form via thermal annealing, and are thus excellent indicators of the stability of the dusty reservoir near the star, as well as the characteristics of the radiation coming from the central star. In addition, the percentage of silicates in crystalline form indicates the degree of dust processing within the reservoir. Both of these can also be used to trace evolutionary status.

This analysis, though ambitious, may provide the pivotal clue astronomers have failed to find so far: the key to unlocking the evolutionary relationship between the astonishingly diverse range of dying intermediate-mass stars.

Bibliography

Allen, D. A., Barton, J. R., & Wallace, P. T. 1981, MNRAS, 196, 797

Allen, D. A., Swings, J. P., & Harvey, P. M. 1972, A&A, 20, 333

Antokhin, I. I., & Cherepashchuk, A. M. 1985, Soviet Astronomy Letters, 11, 355

Bachiller, R., Forveille, T., Huggins, P. J., & Cox, P. 1997, A&A, 324, 1123

Balick, B., & Frank, A. 2002, ARA&A, 40, 439

Bartzakos, P., Moffat, A. F. J., & Niemela, V. S. 2001, MNRAS, 324, 18

Blackman, E. G., Frank, A., Markiel, J. A., Thomas, J. H., & Van Horn, H. M. 2001, Nature, 409, 485

Blöcker, T. 1995, A&A, 299, 755

Boden, A. F., et al. 1999, ApJ, 515, 356

Bouwman, J., Meeus, G., de Koter, A., Hony, S., Dominik, C., & Waters, L. B. F. M. 2001, A&A, 375, 950

Bracher, K. 1979, PASP, 91, 827

Bransford, M. A., Thilker, D. A., Walterbos, R. A. M., & King, N. L. 1999, AJ, 118, 1635

Cami, J., Bernard-Salas, J., Peeters, E., & Malek, S. E. 2010, Science, 329, 1180

Cerrigone, L., Hora, J. L., Umana, G., & Trigilio, C. 2009, ApJ, 703, 585

Cerrigone, L., Hora, J. L., Umana, G., Trigilio, C., Hart, A., & Fazio, G. 2011, ApJ, 738, 121

Cerrigone, L., Umana, G., Trigilio, C., Leto, P., Buemi, C. S., & Hora, J. L. 2008, MNRAS, 390, 363

Chu, Y.-H., Treffers, R. R., & Kwitter, K. B. 1983, ApJS, 53, 937

Cohen, M., Barlow, M. J., Liu, X.-W., & Jones, A. F. 2002, MNRAS, 332, 879

Cohen, M., & Kuhi, L. V. 1977, MNRAS, 180, 37

Colavita, M. M., & Wizinowich, P. L. 2003, in Society of Photo-Optical Instrumentation Engineers (SPIE) Conference Series, Vol. 4838, Society of Photo-Optical Instrumentation Engineers (SPIE) Conference Series, ed. W. A. Traub, 79–88

Colavita, M. M., et al. 1999, ApJ, 510, 505

Cox, A. N. 2000, Allen's astrophysical quantities (AIP Press; Springer)

Crowther, P. A. 2007, ARA&A, 45, 177

Crowther, P. A., & Smith, L. J. 1996, A&A, 305, 541

Cutri, R. M., et al. 2003, 2MASS All Sky Catalog of point sources. (NASA/IPAC Infrared Science Archive)

De Marco, O. 2009, PASP, 121, 316

Dijkstra, C., Dominik, C., Bouwman, J., & de Koter, A. 2006, A&A, 449, 1101

Dougherty, S. M., Beasley, A. J., Claussen, M. J., Zauderer, B. A., & Bolingbroke, N. J. 2005, ApJ, 623, 447

Draine, B. T., & Li, A. 2007, ApJ, 657, 810

Drissen, L., Lamontagne, R., Moffat, A. F. J., Bastien, P., & Seguin, M. 1986, ApJ, 304, 188

Dubner, G. M., Niemela, V. S., & Purton, C. R. 1990, AJ, 99, 857

Eisner, J. A., et al. 2010, ApJ, 718, 774

Fazio, G., Barlow, M., Cohen, M., Crowther, P., Hora, J., & Parker, Q. 2007, Spitzer Proposal, 40115

Fazio, G., Cerrigone, L., Hora, J., Marengo, M., Trigilio, C., & Umana, G. 2006, Spitzer Proposal, 30036

—. 2008, Spitzer Proposal, 50116

Fazio, G. G., et al. 2004, ApJS, 154, 10

Figer, D. F., McLean, I. S., & Najarro, F. 1997, ApJ, 486, 420

Fong, D., Meixner, M., Castro-Carrizo, A., Bujarrabal, V., Latter, W. B., Tielens, A. G. G. M., Kelly, D. M., & Sutton, E. C. 2001, A&A, 367, 652

García-Lario, P. 2006, in IAU Symposium, Vol. 234, Planetary Nebulae in our Galaxy and Beyond, ed. M. J. Barlow & R. H. Méndez, 63–70

Garmany, C. D., & Stencel, R. E. 1992, A&AS, 94, 211

Gielen, C., Cami, J., Bouwman, J., Peeters, E., & Min, M. 2011, A&A, 536, A54

Gielen, C., van Winckel, H., Min, M., Waters, L. B. F. M., & Lloyd Evans, T. 2008, A&A, 490, 725

Gies, D. R. 2003, in IAU Symposium, Vol. 212, A Massive Star Odyssey: From Main Sequence to Supernova, ed. K. van der Hucht, A. Herrero, & C. Esteban, 91

Guzmán-Ramírez, L., Zijlstra, A., Níchuimín, R., Gesicki, K., Lagadec, E., Millar, T. J., & Woods, P. M. 2012, in IAU Symposium, Vol. 283, IAU Symposium, 259–262

Guzman-Ramirez, L., Zijlstra, A. A., Níchuimín, R., Gesicki, K., Lagadec, E., Millar, T. J., & Woods, P. M. 2011, MNRAS, 414, 1667

Hackwell, J. A., Gehrz, R. D., & Smith, J. R. 1974, ApJ, 192, 383

Harries, T. J., Babler, B. L., & Fox, G. K. 2000, A&A, 361, 273

Higdon, S. J. U., et al. 2004, PASP, 116, 975

Houck, J. R., et al. 2004, in Society of Photo-Optical Instrumentation Engineers (SPIE) Conference Series, Vol. 5487, Society of Photo-Optical Instrumentation Engineers (SPIE) Conference Series, ed. J. C. Mather, 62–76

Howarth, I. D., & Schmutz, W. 1992, A&A, 261, 503

Hrivnak, B. J., Geballe, T. R., & Kwok, S. 2007, ApJ, 662, 1059

Hrivnak, B. J., Volk, K., & Kwok, S. 2000, ApJ, 535, 275

Iben, Jr., I., & Tutukov, A. V. 1997, S&T, 94, 36

Ignace, R., Cassinelli, J. P., Quigley, M., & Babler, B. 2001, ApJ, 558, 771

Joint IRAS Science, W. G. 1994, VizieR Online Data Catalog, 2125, 0

Karakas, A., & Lattanzio, J. C. 2007, PASA, 24, 103

Karakas, A. I. 2010, MNRAS, 403, 1413

Karakas, A. I., Lattanzio, J. C., & Pols, O. R. 2002, PASA, 19, 515

Kemper, F., Vriend, W. J., & Tielens, A. G. G. M. 2004, ApJ, 609, 826

Kwok, S. 1993, ARA&A, 31, 63

Kwok, S., & Zhang, Y. 2011, Nature, 479, 80

Lagadec, E., et al. 2011, MNRAS, 417, 32

Lebouteiller, V., Bernard-Salas, J., Sloan, G. C., & Barry, D. J. 2010, PASP, 122, 231

Lefèvre, L., et al. 2005, MNRAS, 360, 141

Libonate, S., Pipher, J. L., Forrest, W. J., & Ashby, M. L. N. 1995, ApJ, 439, 202

Marchenko, S. V., Moffat, A. F. J., & Grosdidier, Y. 1999, ApJ, 522, 433

Marchenko, S. V., et al. 2003, ApJ, 596, 1295

Marengo, M., Stapelfeldt, K., Werner, M. W., Hora, J. L., Fazio, G. G., Schuster, M. T., Carson, J. C., & Megeath, S. T. 2009, ApJ, 700, 1647

Massey, P. 1981, ApJ, 246, 153

Meixner, M., Skinner, C. J., Graham, J. R., Keto, E., Jernigan, J. G., & Arens, J. F. 1997, ApJ, 482, 897

Meixner, M., Ueta, T., Bobrowsky, M., & Speck, A. 2002, ApJ, 571, 936

Meixner, M., et al. 1999, ApJS, 122, 221

Merrill, P. W., & Burwell, C. G. 1950, ApJ, 112, 72

Moe, M., & De Marco, O. 2006, ApJ, 650, 916

Moffat, A. F. J., & Isserstedt, J. 1980, A&A, 91, 147

Molster, F. J., Waters, L. B. F. M., & Tielens, A. G. G. M. 2002a, A&A, 382, 222

Molster, F. J., Waters, L. B. F. M., Tielens, A. G. G. M., & Barlow, M. J. 2002b, A&A, 382, 184

Molster, F. J., et al. 1999, Nature, 401, 563

Monnier, J. D., Tuthill, P. G., & Danchi, W. C. 1999, ApJ, 525, L97

—. 2002, ApJ, 567, L137

Monnier, J. D., et al. 2004, ApJ, 602, L57

Moore, B. D., Hester, J. J., & Scowen, P. A. 2000, AJ, 119, 2991

Murakawa, K., Ueta, T., & Meixner, M. 2010, A&A, 510, A30

Neugebauer, G., et al. 1984, ApJ, 278, L1

Nordhaus, J., Spiegel, D. S., Ibgui, L., Goodman, J., & Burrows, A. 2010, MNRAS, 408, 631

Nugis, T., & Lamers, H. J. G. L. M. 2000, A&A, 360, 227

Olofsson, H. 2008, Physica Scripta Volume T, 133, 014028

Owocki, S. P., Cranmer, S. R., & Gayley, K. G. 1996, ApJ, 472, L115

Panov, K. P., Altmann, M., & Seggewiss, W. 2000, A&A, 355, 607

Parthasarathy, M., & Pottasch, S. R. 1986, A&A, 154, L16

Parthasarathy, M., Vijapurkar, J., & Drilling, J. S. 2000, A&AS, 145, 269

Perea-Calderón, J. V., García-Hernández, D. A., García-Lario, P., Szczerba, R., & Bobrowsky, M. 2009, A&A, 495, L5

Pitault, A., Epchtein, N., Gomez, A. E., & Lortet, M. C. 1983, A&A, 120, 53

Prinja, R. K., Barlow, M. J., & Howarth, I. D. 1990, ApJ, 361, 607

Rajagopal, J. 2010, in Revista Mexicana de Astronomia y Astrofisica Conference Series, Vol. 38, Revista Mexicana de Astronomia y Astrofisica Conference Series, 54–58

Ramos-Larios, G., Guerrero, M. A., Suárez, O., Miranda, L. F., & Gómez, J. F. 2009, A&A, 501, 1207

Reach, W. T., et al. 2005, PASP, 117, 978

Roberts, M. S. 1962, AJ, 67, 79

Sabin, L., Zijlstra, A. A., & Greaves, J. S. 2007, MNRAS, 376, 378

Schuster, M. T., Marengo, M., & Patten, B. M. 2006, in Society of Photo-Optical Instrumentation Engineers (SPIE) Conference Series, Vol. 6270, Society of Photo-Optical Instrumentation Engineers (SPIE) Conference Series

Siódmiak, N., Meixner, M., Ueta, T., Sugerman, B. E. K., Van de Steene, G. C., & Szczerba, R. 2008, ApJ, 677, 382

Skrutskie, M. F., et al. 2006, AJ, 131, 1163

Smith, J. D., & Draine, B. 2012, PAHFIT: Properties of PAH Emission, astrophysics Source Code Library

Smith, J. D. T., & Houck, J. R. 2001, AJ, 121, 2115

Smith, L. F., Shara, M. M., & Moffat, A. F. J. 1996, MNRAS, 281, 163

Speck, A. K., Corman, A. B., Wakeman, K., Wheeler, C. H., & Thompson, G. 2009, ApJ, 691, 1202

Speck, A. K., Whittington, A. G., & Tartar, J. B. 2008, ApJ, 687, L91

St-Louis, N., Chené, A.-N., Schnurr, O., & Nicol, M.-H. 2009, ApJ, 698, 1951

Stanghellini, L., & Renzini, A. 2000, ApJ, 542, 308

Suárez, O., García-Lario, P., Manchado, A., Manteiga, M., Ulla, A., & Pottasch, S. R. 2006, A&A, 458, 173

Szczerba, R., Siódmiak, N., Stasińska, G., & Borkowski, J. 2007, A&A, 469, 799

Tielens, A. G. G. M. 2008, ARA&A, 46, 289

Torres, A. V., & Conti, P. S. 1984, ApJ, 280, 181

Tuthill, P. G., Monnier, J. D., & Danchi, W. C. 1999, Nature, 398, 487

Ueta, T., Meixner, M., & Bobrowsky, M. 2000, ApJ, 528, 861

Ueta, T., Murakawa, K., & Meixner, M. 2005, AJ, 129, 1625

Umana, G., Cerrigone, L., Trigilio, C., & Zappalà, R. A. 2004, A&A, 428, 121

van Aarle, E., van Winckel, H., Lloyd Evans, T., Ueta, T., Wood, P. R., & Ginsburg, A. G. 2011, A&A, 530, A90

van Belle, G. T., et al. 1999, AJ, 117, 521

van Breemen, J. M., et al. 2011, A&A, 526, A152

van der Hucht, K. A. 1992, A&A Rev., 4, 123

—. 2001, New A Rev., 45, 135

van der Veen, W. E. C. J., & Habing, H. J. 1988, A&A, 194, 125

van der Veen, W. E. C. J., Habing, H. J., & Geballe, T. R. 1989, A&A, 226, 108

van Loon, J. T., Cioni, M.-R. L., Zijlstra, A. A., & Loup, C. 2005, A&A, 438, 273

van Winckel, H. 2003, ARA&A, 41, 391

Vasisht, G., Booth, A. J., Colavita, M. M., Johnson, Jr., R. L., Ligon, III, E. R., Moore, J. D., & Palmer, D. L. 2003, in Society of Photo-Optical Instrumentation Engineers (SPIE) Conference Series, Vol. 4838, Society of Photo-Optical Instrumentation Engineers (SPIE) Conference Series, ed. W. A. Traub, 824–834

Veen, P. M., van Genderen, A. M., van der Hucht, K. A., Li, A., Sterken, C., & Dominik, C. 1998, A&A, 329, 199

Waters, L. B. F. M., et al. 1998, Nature, 391, 868

Werner, M. W., et al. 2004, ApJS, 154, 1

Williams, P. M., van der Hucht, K. A., & The, P. S. 1987a, QJRAS, 28, 248

Williams, P. M., van der Hucht, K. A., van der Woerd, H., Wamsteker, W. M., & Geballe, T. R. 1987b, in Astrophysics and Space Science Library, Vol. 136, Instabilities in Luminous Early Type Stars, ed. H. J. G. L. M. Lamers & C. W. H. De Loore, 221–226

Wizinowich, P. L., Le Mignant, D., Stomski, Jr., P. J., Acton, D. S., Contos, A. R., & Neyman, C. R. 2003, in Society of Photo-Optical Instrumentation Engineers (SPIE) Conference Series, Vol. 4839, Society of Photo-Optical Instrumentation Engineers (SPIE) Conference Series, ed. P. L. Wizinowich & D. Bonaccini, 9–20

Yamamura, I., Makiuti, S., Ikeda, N., Fukuda, Y., Oyabu, S., Koga, T., & White, G. J. 2010, VizieR Online Data Catalog, 2298, 0

Yamamura, I., et al. 2009, in American Institute of Physics Conference Series, Vol. 1158, American Institute of Physics Conference Series, ed. T. Usuda, M. Tamura, & M. Ishii, 169–170

Zhang, Y., Kwok, S., & Hrivnak, B. J. 2010, ApJ, 725, 990

Zijlstra, A. A., Gaylard, M. J., te Lintel Hekkert, P., Menzies, J., Nyman, L.-A., & Schwarz, H. E. 1991, A&A, 243, L9

Zubko, V. G. 1998, MNRAS, 295, 109